INTRINSIC PHOTOCATALYTIC ACTIVITY OF TiO_2 IN GAS PHASE CO_2 REDUCTION: LIGHT COUPLING, MASS TRANSFER, AND MICROKINETICS MODELS.

A Thesis

Presented to the Faculty of the Graduate School

of Cornell University

In Partial Fulfillment of the Requirements for the Degree of

Master of Science| Chemical Engineering

by

Hugo Alejandro Vignolo Gonzalez

August, 2017

ABSTRACT

Applications of photocatalytic CO_2 reduction are limited by poor overall efficiency and slow reaction rates. In addition to such intrinsic material's limitations, external influences decrease observed reaction rates still further. This work aims to quantify those external factors in a batch photocatalytic gas-phase reactor for CO_2 reduction on P25 (TiO_2), approaching to the intrinsic activity of the material under standard conditions. The proposed methodology addressed optical aspects of the reactor design to decouple the influence of light in observed reaction rates; as a thin film with an optical effectiveness of 67%, P25 showed a yield of 14.5 [μmoles-C-products g^{-1} h^{-1}], which is at least 20 times higher compared to previous references. A transport model demonstrated the small influence of diffusion based on a dimensional analysis and perturbation expansion. As a final remark, reaction mechanisms were analyzed using Microkinetics Analysis (MKA), whose qualitative predictions explained reaction trends not captured by coarse-grain models.

BIOGRAPHICAL SKETCH

Hugo Vignolo is currently in his 2nd year of study in the Robert Frederick School of Chemical and Biomolecular Engineering at Cornell University. In August 2017, He will receive his official degree of Master of Science in Chemical Engineering, with a minor focus on Sustainable Energy Systems. Mr. Vignolo is a Fulbright fellow coming from Chile, country where he has received several awards for both his professional and academic achievements in the area of Chemical Process Engineering, including the Fulbright Chile Foreign Master Program Award (Fulbright Chile, 2015), and the Federico Santa Maria Award (UTFSM Chile, 2013).

During the last semesters, Hugo was part of the Hanrath Energy Lab research group, where he applied different concepts of advanced transport phenomena and computational methods applied to heterogeneous catalysis, aiming to understand more in depth the fundamental physical phenomena triggering CO_2 reduction using photocatalysis. These experimental and computational research experiences gave him valuable insight to start discovering new materials suitable for artificial photosynthesis under the concepts of intrinsic photocatalytic activity, and surface reaction models. Hugo successfully passed his Master of Science Thesis defense examination in May 2017, and since August 2017 he will be part of Prof. Lotsch research group in nanochemistry at the Max Planck Institute for Solid State Physics in Germany. As a Ph.D. candidate in this group, Hugo will be investigating new materials different than TiO_2 to reduce CO_2, using similar concepts in advanced photo-reactor design and intrinsic kinetics.

Outside of academics, Hugo was also the treasurer of the Chilean Association at Cornell University (CHAS), and project assistant and volunteer at the Cornell Lab of Ornithology, in the Citizen Science Program. In the past, Hugo was also involved in several Musical Programs in the city of Viña del Mar, Chile. In such programs, Hugo enjoyed enormously performing different classical piano pieces to the community of famous composers like W.A. Mozart and L.V. Beethoven sonatas, and J.S. Bach Inventions among others. Other Hugo's hobbies include athletics, hiking, and reading philosophy.

Dedicado con todo mi cariño a mi esposa, Daruska, por su apoyo incondicional hacia mí durante esta etapa, y también a mis amigos, padres, abuelos, hermanos, y familia en general, por ayudarme a ser quién soy y motivarme siempre a alcanzar mis sueños.

ACKNOWLEDGMENTS

I wish to express my appreciation and gratitude to all my Committee members, Prof. Hanrath, Prof. Brad and Prof. Escobedo, for their help, guidance, and support during my MS adventure. This was a journey that involved meaningful research and advanced technical skills that required very different expertise, and I found them both in my committee and research group. I am grateful for everyone's patience and willingness to help inside the group, and I also specially recognize the experimental help and patience of Kevin and Jessica.

I would like to thank all my Cornell/Ithacan folks that made this experience a fun trip through their friendship: Kevin, Ben, Victor, Javier, Mari, Daniel, Carolina, Rodri, Camila, Ignacio, JuanJo, Jose Lenin, Elijah, Shaun, Sean, Max, Steve, Eric, Winston, Christine, and to all my friends out of Cornell: Marta, Kelsey, Jeremy, Erika, Matt, Vane, Marilu, nana, Alejandra, Karen, and many others whose names do not come to my mind right now.

My sincerest gratitude to the Fulbright Chile Scholarship that allowed me to pursue this dream, and the Cornell Grad School and College of Engineering for their financial support.

TABLE OF CONTENTS

LIST OF FIGURES

LIST OF TABLES

LIST OF ABBREVIATIONS

CB	: Conduction band
DFT	: Density Functional Theory
FFT	: Fourier Finite Transform
GC	: Gas Chromatograph
HER	: Hydrogen Evolution Reaction
KMC	: Kinetic Monte Carlo
L-B	: Langmuir-Blodgett
L-H	: Langmuir-Hinshelwood
LVRPA	: Local Volumetric Rates of Photon Absorption
MKA	: Microkinetics Analysis
ML	: Monolayer
NHE	: Normal Hydrogen Electrode
NP	: Nanoparticles
ODE	: Ordinary Differential Equation
PDE	: Partial Differential Equation
PEG	: Polyethylene Glycol
QY	: Quantum Yield
VB	: Valence band

LIST OF SYMBOLS

a : Specific area per gram of catalyst

$k_{L\text{-}H}$: Langmuir-Hinshelwood constant at incident light intensity

α_A : Effective Absorption extinction coefficient

α_E : Total extinction coefficient

α_S : Rayleigh Scattering extinction coefficient

β : Light dependency power number

δ_F : Active film thickness

ε : Small parameter Damkohler-like for L-H reaction

λ : Mean free path

Φ : Photon flux

Φ_L : Optical effectiveness

CHAPTER 1

INTRODUCTION

Photocatalysis using titanium oxide (TiO_2) based materials has been proposed as one of the greener and sustainable technologies to address key environmental issues that our society is facing nowadays, such as pollution and global warming [1]. Particularly global warming has motivated several actions to reduce CO_2 emissions worldwide, including incentives for carbon sequestration technologies, promotion of renewable energy generation, and energy storage, among others. A particular niche has arisen last decades combining said technologies, and is known as solar fuels, which is the denomination given to the transformation of solar energy into chemical-carriers. It results particularly attractive to use CO_2 as a chemical-carrier, and one of the simplest approaches to do so is using photocatalysis to reduce CO_2 [2]. However, direct conversion of CO_2 to higher value compounds using sunlight in presence of water has been particularly hard. Typical yields for CO_2 photocatalysis are in the order of 1 to 1,000 [$\mu moles\ g^{-1}\ h^{-1}$] for the most efficient materials, which makes any industrial application to stationary carbon sources still unfeasible [3].

In this search for better photocatalysts for CO_2 reduction, TiO_2 based materials, specifically P25 has been consistently used in literature as baseline to compare the activity of new composites that incorporate co-catalysts, dopants and noble metals [4]. However, the experimental procedures to date have not addressed external influences

that underestimates photocatalysts activity. Particularly gas-phase CO_2 reduction, no other work to date has decoupled the influence of light and mass transfer from observed CO_2 reduction rates.

Consequently, the aim of this work is to provide a methodology to unravel the intrinsic activity of P25. In principle, the methodology can be applied to any other photo-active materials, though we found P25 the best candidate as it re-defines the baseline activity for future works. We started addressing the influence of light experimentally, using an engineered film catalyst load and few simple models to characterize the influence of light, previous to the measurement of photocatalytic activities. The measured activities of the films were further analyzed theoretically using mathematical models based on regular perturbation expansions, to decouple the influence of mass transfer limitations, not only in this setup but presenting a general analytical solution that applies to any case.

The reactor chosen was a water-vapor batch cell that would allow to make reaction kinetics analysis simpler. The model for surface reaction is tangential to the intrinsic activity of the material, but it provides useful insight for reaction limitations for later optimization works. Taking this into account, a final piece of the work was a proof of concept of mechanistic models explaining observed trends in the formation of products. The formation of products can be particularly hard to explain for coarse-grain approximations, like the widespread pseudo-Langmuir-Hinshelwood (L-H). Although L-H mechanisms provide enough complexity to locally fit experimental reaction curves, it was shown that only mechanistic models like Microkinetics Analysis (MKA) can

explain drastic changes in product selectivity under different illumination, and formation of key intermediates.

The structure of the document of the document is as it follows:

- Chapter 2 presents a literature review like summary of the state of the art of CO_2 photocatalysis and the specific case of TiO_2 materials. General ideas about solar fuels and related technologies will be addressed to contextualize the work. The Chapter goes through the choice of batch reactors with water vapors as a candidate to measure intrinsic activity of P25, and the different deposition techniques available to simplify the catalyst load from the perspective of optics. The Chapter ends showing the concept of intrinsic kinetics and surface reaction modeling, together with its motivations and limitations.
- Chapter 3 is dedicated exclusively to the influence of light in observed reaction rates. The topic starts with the definition of light dependent rates and optical properties of photo-reactors. The production and optical characterization of the catalyst in form of a film is the center piece of the Chapter, and finalizes with a mathematical description of the reactor scale-up considering light aspects; the concept of catalyst optical effectiveness is also introduced.
- Chapter 4 starts with a summary of all the experimental procedures to obtain reliable reaction rates using a Gas Chromatograph (GC) equipment. The data is presented, analyzed in terms of optical utilization concepts presented in Chapter 3, and finally fitted to typical coarse-grain models used in literature.
- Chapter 5 is a mathematical modeling section describing the influence of mass transfer limitations in observed rates. It is the continuation of the reactor scaling-

up concepts presented in Chapter 3 but considering diffusion gradients. The key aspects of this section are non-dimensional analysis of reaction-diffusion equations with L-H kinetics in a boundary condition. The problem will be treated using a regular perturbation analysis coupled to an FFT solution to Partial Differential Equations (PDE).

- Chapter 6 is a proof of concept of MKA models explaining more complex behavior not captured by coarse-grain models. The section will link solid-state physics, redox phenomena, gas-solid adsorption, and Density Functional Theory (DFT) simulations of CO_2 reduction pathways to extrapolate the experimental results to cases with high higher illumination.
- Chapter 7 is conclusions and future steps considering the limitations of this method and the concepts that were not fully explained in this work.

CHAPTER 2

LITERATURE REVIEW

2.1 Photocatalysis Background

Environmental issues are nowadays one of the biggest problems of modern societies. Both environmental pollution and the lack of sustainable and renewable energetic sources are enormous challenges for the development of an always expanding global community. This constant increase of world's population and unrestrained industrial expansion have speeded up energy demand, intensifying year by year the release of untreated toxic agents, pollutants and industrial wastes. Part of the consequences of said managements includes pollutions-related diseases, global warming, and abnormal climatic changes [1].

In this way, photocatalysis presents an alternative for solar harvesting that is abundant, sustainable, and sometimes economically viable. Additionally, titanium oxide (TiO_2), which is one of the most widespread materials for photocatalysis applications, it is cheap, highly reactive, and non-toxic. Some of the applications of TiO_2 include purification of polluted water and air, self-cleaning glasses, among others [1, 5]. Particularly in this work, we will focus our attention on photocatalysis using TiO_2 to reduce CO_2 and split water.

2.1.1 Photocatalysis Basic Features

In most applications, the main goal of photocatalysis is the conversion of light to chemical energy. Most likely, this conversion is the breakage or creation of chemical bonds. The conversion process occurs when a photocatalytically active material absorbs photons of a certain range of wavelengths, which triggers chemical reaction when reactive species are adsorbed or in solution near the surface of the material. In semiconductors, when a photon of energy higher than the bandgap of the material is absorbed produces the promotion of an electron from the valence band to the conduction band of the material. This process is known as excitation and generates an electron-hole pair. The electron-hole pairs generated are in close proximity and localized in the coordinate bonds of the material, i.e., Ti^{+4} in TiO_2. Once it is separated, the pairs are very short-lived and can recombine releasing radiation or heat to the crystal [1, 4, 6].

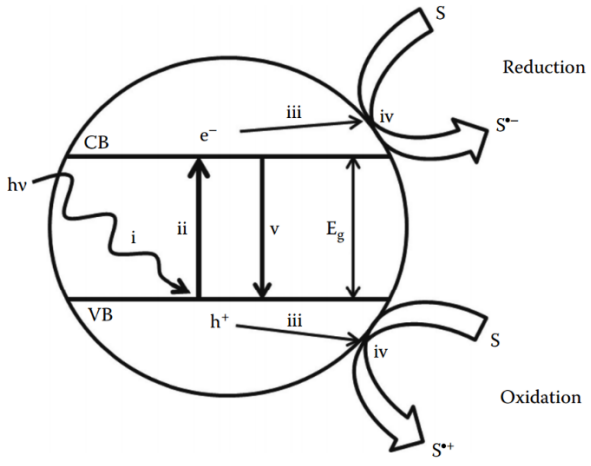

Figure 2-1 Elementary steps of photocatalysis. Reproduced [Primo, Neaţu and Garcia, 2015].

Although recombination of pairs is the most dominant phenomena in photocatalysis, because occurs in the sub-microsecond scale, trapping charges is still possible if some fraction of the free charges migrate to the surface of the material and

triggers electron-transfer reactions with adsorbates. The different fates of the free charges are presented in the Figure 2-1, where: (i)light absorption, (ii)charge generation, (iii)electron-hole diffusion separation, (iv)reduction of adsorbate S, (iv)oxidation of adsorbate S, (v)recombination of electron-hole pairs. As electron holes are generated in pairs, in steady-state the reduction rate must equal oxidation rates [1, 7].

2.1.2 Photocatalysis Applications

When no species are adsorbed to serve as electron or holes scavengers, the stored energy is dissipated as heat or radiation when electron-holes recombine [8]. If reactive species are available to trap electrons or holes, recombination is avoided and following redox reaction are possible [9]. In TiO_2 based materials, the valence band has a strong oxidizing potential (Rutile is +3.5 V compared to NHE). In some cases, the conduction band is also a suitable reductant (Rutile is +0.4 V compared to NHE) [10]. In liquid media or ambient air, typical electron acceptor and hole-scavengers are oxygen and water respectively. The interaction of such activated molecules usually form Reactive Oxygen Species (ROS). Typical ROS includes hydrogen peroxide (H_2O_2), hydroxyl radicals (OH), and superoxide (O_2). The high oxidation potential of ROS (i.e, Eox=+2.80 V for •OH radical) makes them very reactive in presence of electron-rich organic compounds; OH and H_2O_2 can theoretically degrade a wide variety of pollutants. Illuminated semiconductors has been successfully used for the remediation of pollutants including alkanes, alcohols, aliphatic carboxylic acids, phenols, aromatics, dyes, among others [1, 4].

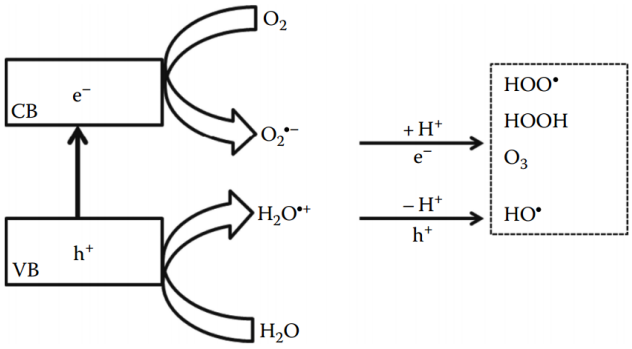

Figure 2-2 Photocatalysis application to organic degradation. Reproduced from [Primo, Neaţu and Garcia, 2015].

Besides its application to degradation of organic compounds, photocatalysis received a major thrust after the novel work of Fujishima and Honda [11]. In this work, the field of photocatalysis was also expanded to hydrogen production from water (water splitting) and CO_2 reduction on later works [1, 12]. Both, CO_2 and water splitting, will be discussed more thoroughly in the context of solar fuels.

2.2 Solar Fuels

2.2.1 Motivations

The increase in the CO_2 atmospheric concentration to roughly 46% above that of pre-industrial levels (260-380 ppm in volume) has motivated several worldwide efforts to reduce anthropogenic CO_2 emissions [13]. Moreover, the reduction of CO_2 emissions has become a major concern that not only includes the scientific community but policymakers and other stakeholders; the Paris agreement (COP21, 2015) is a proof of the importance of promoting green energies and mitigation of the impacts of fossil fuels in GHG atmospheric levels. Together with transportation, the electricity

generation from fossil fuels power plants appears as one of the major contributors to the rate of CO_2 emissions in the U.S. (16% of the total global emissions) that should be promptly treated [13].

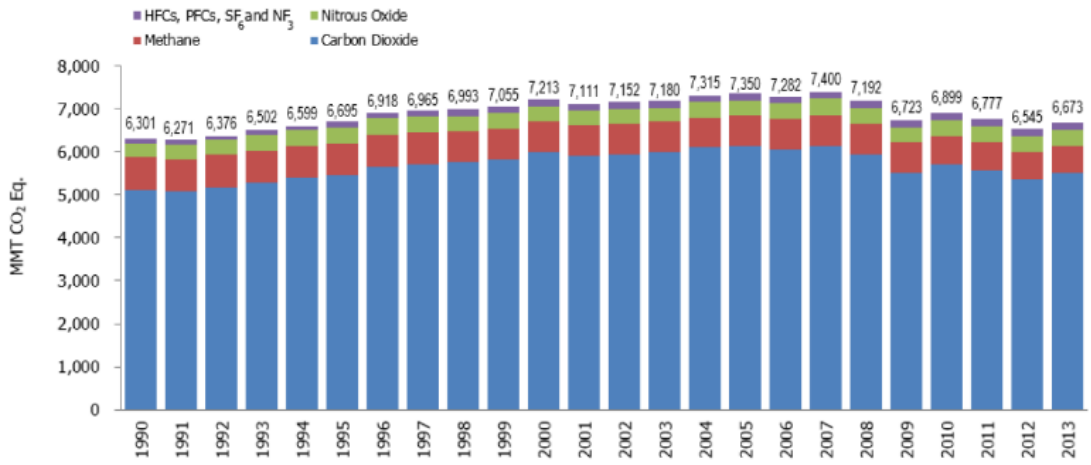

Figure 2-3 GHG increase in time (1990-2013) in the US per type of gas. Reproduced from [EPA, 2015].

On the other hand, since the experiment of Honda and Fujushima was done, the alternative of transforming solar energy into chemical compounds appeared as an alternative to directly convert sunlight into chemical carriers. More generally, chemical storage of solar energy in any of its forms is indeed a potential solution to several constraints of other renewable energy sources, mainly dispatchable generation and day night-cycles [10, 12, 14]. For this reason, together with global warming concerns, numerous efforts have been made last decades to feasibly use CO_2 as chemical energy carrier to both mitigate CO_2 emissions from stationary sources, and store solar energy; instead of using large battery or capacitor banks, what is known as solar fuels technologies could directly convert a solar energy input into energy dense products [3].

Typical electrochemical conversions of CO_2 to solar fuels and their electrochemical potential are presented in Table 2-1.

Table 2-1 Electrochemical potential for CO_2 reduction to different solar fuels. Reproduced from [White et al, 2015].

Reaction	E^0 vs SHE (V)
$CO_2 + e^- \rightarrow CO_2^{\cdot -}$	-1.85
$CO_{2(g)} + H_2O_{(l)} + 2e^- \rightarrow HCOO^-_{(aq)} + OH^-_{(aq)}$	-0.665
$CO_{2(g)} + H_2O_{(l)} + 2e^- \rightarrow CO_{(g)} + 2OH^-_{(aq)}$	-0.521
$CO_{2(g)} + 3H_2O_{(l)} + 4e^- \rightarrow HCOH_{(l)} + 4OH^-_{(aq)}$	-0.485
$CO_{2(g)} + 5H_2O_{(l)} + 6e^- \rightarrow CH_3OH_{(l)} + 6OH^-_{(aq)}$	-0.399
$CO_{2(g)} + 6H_2O_{(l)} + 8e^- \rightarrow CH_{4(g)} + 8OH^-_{(aq)}$	-0.246
$2H_2O_{(l)} + 2e^- \rightarrow H_{2(g)} + 2OH^-_{(aq)}$	-0.414

2.2.2 Carbon based Solar Fuel technologies

In this scenario, not only photocatalysis but any technology able store solar energy using CO_2 as energy carrier present noticeable advantages compared to other CO_2 abetment or Energy Storage technologies alones. For example, promoting amine treatments appears as a robust technology to capture and sequestrate CO_2 from stationary sources; these are known as Carbon Capture and Sequestration technologies (CCS). However, since CCS technologies do not add any value to the captured CO_2, they are facing serious economic challenges, besides its technical limitation associated

to the regeneration of the capturing amine and the compression of CO_2 concentrated gas [15].

Among energy storage technologies, fuel cells are also interesting alternatives to convert renewables into super-efficient fuels like Hydrogen and Ammonia; in fact, the overall energy efficiency cycle in heat engines is far less efficient compared to hydrogen and ammonia fuel cells . Nevertheless, solar fuels become particularly more attractive when its consumption can rely on the same infrastructure as the actual fossil fuels economy does. Additionally, important limitations exists for a classical hydrogen economy since its storage and transportation has an important economic burden (more than the competitive price of 2-4 USD per delivered H_2 kg). CO_2 derived solar fuels on the other hand have a wide variety of options to be further commercialized in the regular fuel market [16, 17]. As an example of this concept, a solar fuel economy scheme is presented in Figure 2-4.

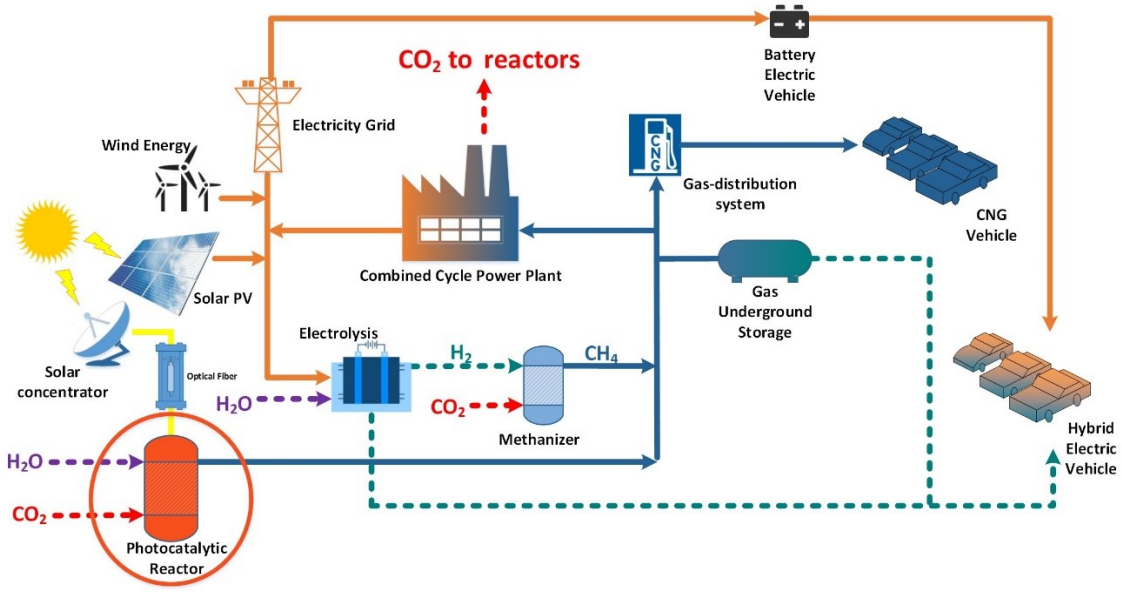

Figure 2-4 Solar fuel economy scheme. Adapted from [Rybtchinski et al, 2010].

Having figured out that solar fuels have its own niche when it comes to CO_2 mitigation technologies, the way to classify the CO_2 reduction technologies by the nature of the energy input and transformation process are the following.

Photocatalytic: As previously mentioned, photocatalysis is a form of inorganic photosynthesis. TIO_2 is the most common material used to conveniently promote redox reactions (Band gap of 3.05 eV). Even though it has not been demonstrated rigorously, it is believed that feasible reaction mechanisms TiO_2 involve multi electron transfer. In semiconductors, typical limitations are fast recombination and poor visible light response. One way to enhance the poor light absorption in the solar range (5% approximately) and therefore the overall performance is to combine this material by adding Cu/Ag/Au/Pd materials as cocatalysts. They way that this reaction can be performed is either in a disperse matrix or in heterogeneous bulk suspension, or in liquid media or gas-phase [6, 10, 12, 18].

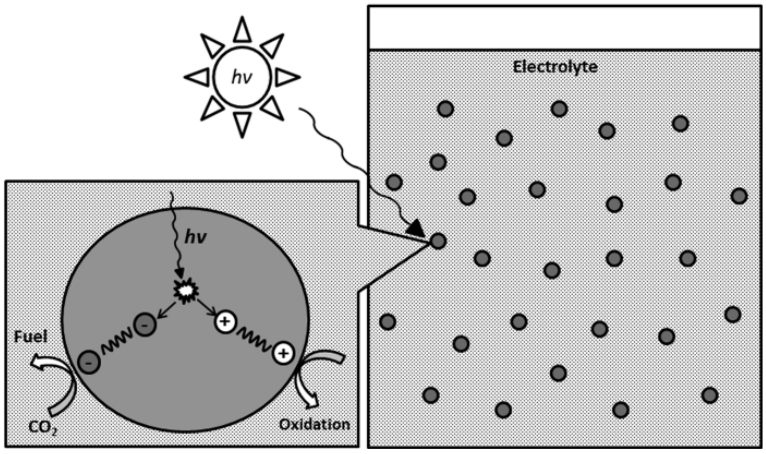

Figure 2-5 Photocatalytic CO_2 reduction. Reproduced from [White et al, 2015].

Electrochemical: It is just a subtype of regular electrochemistry applied to energy conversion. Not only solar PV may be applied to produce the electricity needed; wind or other renewables can be used to produce a potential. When a potential is applied several reactions may occur in the electrodes under electrochemistry principles. The result when applied for example to CO_2 containing electrolyte, different forms of carbon reductions reactions will spontaneously occur, i.e. Oxalic and Formic Acid formation. Although this process itself it is highly efficient compared to photocatalytic processes, most electro catalytic active surfaces like copper are self-degrading and has other technical and economical limitations to be considered as a robust solar fuel technology, such as poisoning of scarce materials and selectivity issues [19, 20].

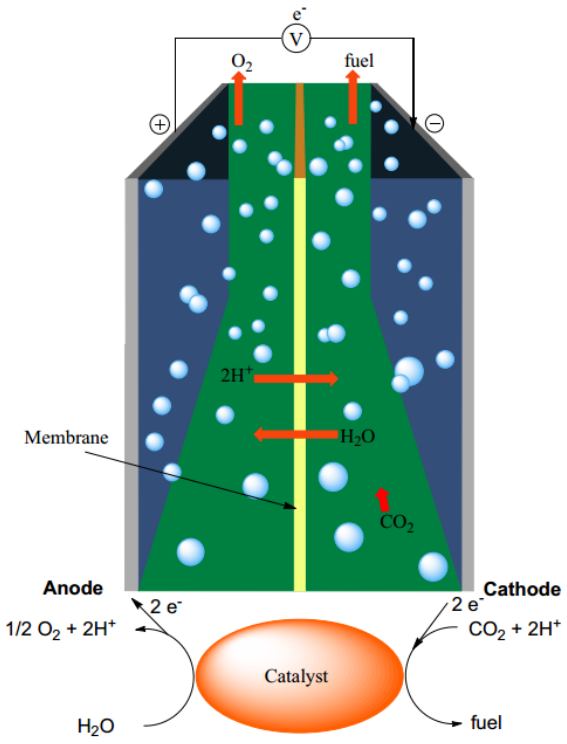

Figure 2-6 Electrocatalytic CO_2 reduction. Reproduced from [Fenwick et al, 2015].

Photo electrochemical: It is in principle the combination of both electrocatalytic and photocatalytic CO_2 reduction. It consists of a photo electrode that provides charge excitation, charge/hole separation and catalytic surface under illumination to produce a half reduction reaction in the semiconductor photocathode, whereas oxidation occurs in the anode with an additional external biased electric potential [10].

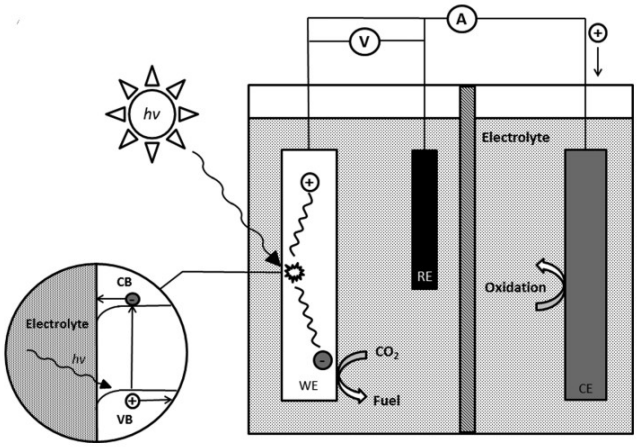

Figure 2-7 Photocelectrochemical CO_2 reduction. Reproduced from [White et al, 2015].

2.3 Water splitting and CO_2 photocatalytic reduction on TiO_2

2.3.1 Semiconductor materials

A semiconductor is a material with an intermediate electrical conductivity; it lies between a conductor and an insulator. However, it also differentiates from a conductor basically because the conductivity of a semiconductor increases with temperature, whereas a metal has exactly the opposite trend. This and other distinctive electronic properties are given by its valence band (VB) and the conduction band (CB). This definition comes from quantum mechanical properties, which sets the highest occupied

molecular orbital (HOMO), and the lowest unoccupied molecular orbital (LUMO). In practice, the HOMO/LUMO interaction within the material is equivalent to the VB and CB definition, since an electron is not allowed to jump to an Energy level between those two states [5, 10]. This energy jump from the VB to the CB is also known as the bandgap of the material, or E_g. Both the bandgap and the relative positions of the CB and VB are one of the fingerprints of the material in photocatalysis, since it defines light absorption properties and red/ox potentials [10]

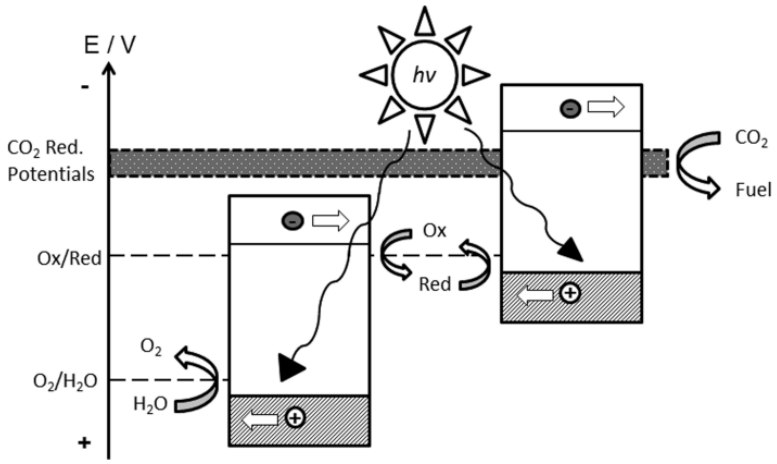

Figure 2-8 Semiconductor junction for CO_2 photocatalytic reduction. Reproduced from [White et al, 2015].

Figure 2-8 summarizes the key steps in photocatalytic CO_2 reduction using a typical junction of two semiconductors, which is a common way to improve redox reaction rates based on band-alignment and bandgap concepts. As it was presented previously, the process starts with the light absorption and subsequent generation of electron-holes pairs. Photons with energy exceeding the bandgap of the material triggers

the jump of electron from the VB to the CB, and an additional flux of charges can be generated at the heterojunctions.

In despite of the fraction of electron-hole pairs that undergo recombination, only the free photogenerated charges that reaches the surface produces reaction; defective crystals and surfaces are usually recombination centers that decreases photocatalytic activity. Thus, efficient separation of charges appears is one key aspect to improve the overall efficiency of desired reactions. Separation of charges and surface area are the main reason why photocatalysis is almost always conducted in nanoparticles [21].

The reaction on surface is a complex system whose actives species are initially generated after charges have been separated and reached the surface. Reactivity of the CB and VB with precursor adsorbates in surface is given by the relative position of those energy levels compared to electrochemical red/ox potential. For example, water splitting only occurs when the position of the CB of a semiconductor is more negative than the redox potential $H+/H_2$ (0 V vs NHE, pH = 7), and when the energy level of the VB is more positive than the redox potential of O_2/H_2O (1.23 V vs NHE, pH = 7) [4, 10, 12]. Although in some particular cases one semiconductor material can provide generation and separation of charges, and surface active centers at the same time, most efficient and faster photocatalytic reactions only occurs when noble metal and metal oxides are loaded to the surface; this is known as the Z-Scheme, or dual Z-scheme (Figure 2-8).

2.3.2 Phase Structures of TiO_2

More generally, polycrystalline materials properties depend also on the phase structures that they can present. In TiO_2, this is also a key feature in photocatalytic activity. The classical four TiO_2 polymorph are anatase, rutile, brookite, and TiO_2 (B). The geometries of such polymorphs are presented in Table 2-2. All those type are coordinated bonded unit cells forming in TiO_6 octahedra, but they have a different distortions, edges and corners.

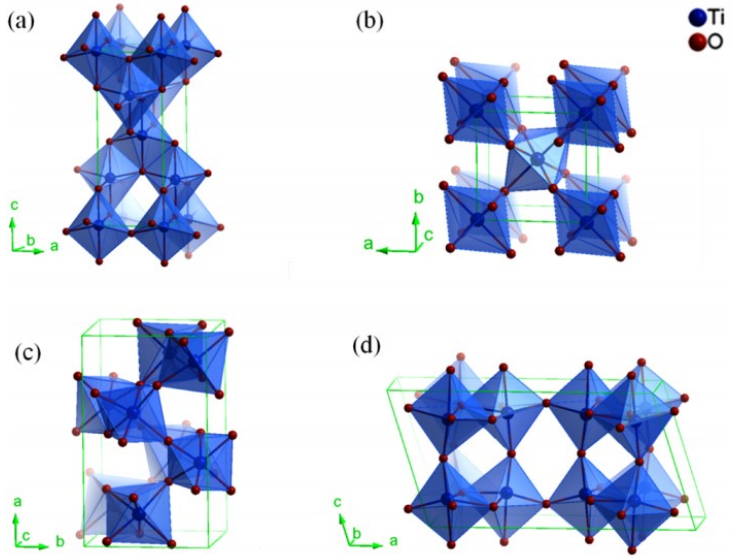

Figure 2-9 Phase structures of TiO_2. Reproduced from [Ma et al, 2015]. (a) anatase, (b) rutile, (c) brookite, (d) TiO2 (B)

Table 2-2 Four main Polymorphs of TiO_2 and their structural parameters. Reproduced from [Ma et al, 2015]

Crystal form	**Crystal system**	**Unit cell parameters**			
		a/nm	b/nm	c/nm	β/deg
anatase	tetragonal	0.379		0.951	

rutile	tetragonal	0.459		0.296	
brookite	orthorhombic	0.918	0.545	0.515	
TiO_2(B)	monoclinic	1.216	0.374	0.651	107.3

Several works have tested TiO_2 as a baseline photocatalyst to split water, biomass reforming, and for solar fuel production in general. As TiO_2 band gap is approximately 3.2 [eV], its light absorption property is limited to roughly 5% of the total solar spectrum (UV range). Even so TiO_2 is still a good reference to understand both charge-separation and reaction mechanisms. The activity of TiO_2 is also dependent on the phase structure, for example: rutile and anatase have a slightly different band gap (3.2 [eV] and 3.02 [eV] respectively). This makes anatase a material with a higher redox potential, but more limited by light absorption. Additionally, anatase has more surface area, better charge separation, and therefore is more abundant in both active sites and adsorption sites. On the other hand, due to its higher crystallinity, rutile can present better charge mobility [22].

2.3.3 Photocatalytic activity of P25 for CO_2 reduction

As presented in previous sections, TiO_2 is a typical benchmark material. However, due to its variety of phase structure, it has been necessary to standardize its photocatalytic activity with respect to one specific polycrystalline structure. Due to its high photocatalytic activity for water splitting, commercial availability and standardization, Degussa P25 is maybe the most widespread reference both for baseline performance testing and theoretical works in CO_2 reduction [3, 23, 24, 25]. The

combination of rutile and anatase bulk structures confers P25 a small visible light response, a better charge separation, and heterojunctions that are believed to act as pseudo-Z-schemes [26].

2.3.4 Time-scales

The different processes involved in CO_2 photocatalysis on semiconductors have a very dissimilar time-scale, which makes any further analysis of reaction kinetics an inherently multi-scale problem. Some key steps of reaction mechanisms of interest lay on the interfacial charge transfer time-scale. In Figure 2-10 a summary of the characteristic time-scales for the different steps is presented. Since in typical CO_2 reduction experiments the characteristic time for depletion of CO_2 is in the range of thousands of hours, it can be deducted that the convolution of all the processes does not show the time-scale of the limiting-step alone, i.e. Hydroxyl activation (10-100 [μs]). This suggests that a steady state is reached in an ultrafast time-scale for charge carriers movements, and other adsorption (100[ns]) and slow activation processes. In a second stage, further slow reaction involving classical mechanisms for CO_2 activation and hydrogenation may take place. This time-scale dissociation will have an enormous impact on the approach used to analyze reaction mechanisms. For instance, it should be kept in mind that key steps in photocatalysis occurs in a range of time-scales from femto-seconds to couple of seconds [27].

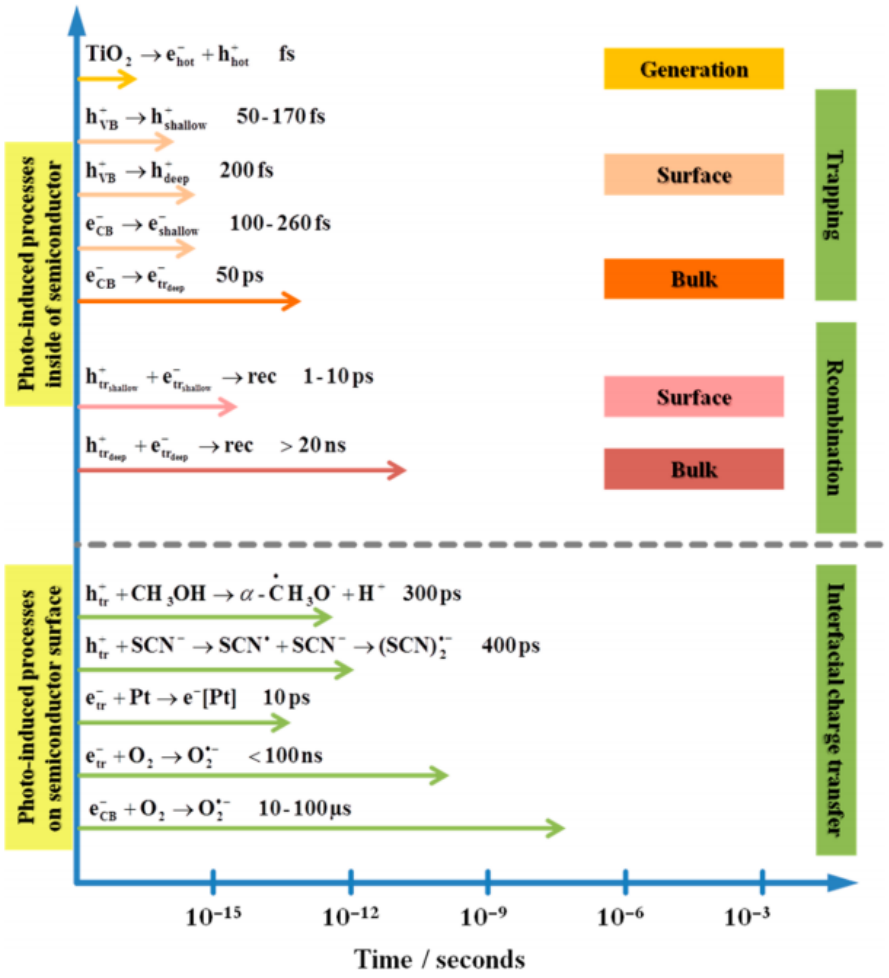

Figure 2-10 Time-scales in photocatalysis in semiconductors. Reproduced from [Schneider et al, 2014].

2.3.5 Key indicators of photocatalytic performance

So far, we have presented most of the key aspects of the photocatalytic CO_2 reduction in TiO_2. However, in order to have a standardize comparison along different materials, it is sometimes useful to define key indicators of the overall performance, which are simplified quantifications of photocatalytic activity. Below a description of the most widespread indicators used in literature [6].

$$Turnover\ Number\ (TON) = \frac{moles\ products}{moles\ of\ catalysts}$$

$$Turnover\ Number\ (TOF) = catalytic\ turnovers/time$$

$$Catalyst\ selectivity\ (CS) = \frac{moles\ intended\ products}{moles\ other\ products}$$

$$Product\ Yield\ = \frac{moles\ products}{catalyst\ mass\ \times\ time}$$

$$Quantum\ Yield\ (\Phi) = \frac{\#products}{\#absorbed\ photons}$$

$$Apparent\ Quantum\ Yield\ \left(\Phi_{App}\right) = \frac{\#products}{\#Irradiated\ photons}$$

2.4 Laboratory scale water vapor photo-reactor

2.4.1 Typical setup

In this work we will focus our attention on CO_2 photocatalytic reduction in presence of water vapors. Although a rich experimental literature about CO_2 reduction in liquid media is available for a wide variety of materials, the primary aim of this work is to gain some insight on reaction kinetics and light influences. The advantages of using water vapors for these purposes includes: (1) Liquid water reactors usually have suspended particles that makes light propagation characterization very difficult, (2) The elementary steps in the solid-gas interface are closer to ideal gas assumptions, both for adsorption and classical reaction, (3) The possibility of changing the CO_2 concentration, which is limited by solubility in liquid water reactors; ad (4) The liquid water reactor

presents even higher reaction limitations because its reaction mechanism is seldom complicated carbonates activation [25, 28, 29]. A typical setup of water vapor photo-reactor is presented in Figure 2-11 (1: CO_2 gas flowmeter, 2: bubbler, 3: reactor cell, 4: supported photo-active material, 5: quartz window, 6: filter/polarizer, 7: UV-light source, 8: sampling port, 9: relief, 10: Gas Chromatograph [GC] + detector).

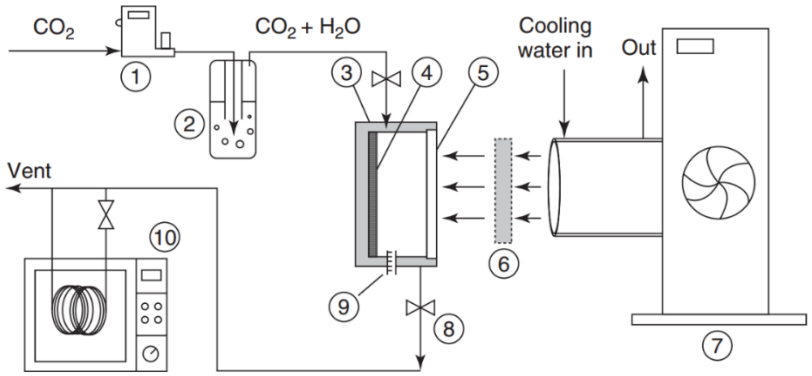

Figure 2-11 Typical batch photoreactor for CO_2 reduction with water vapors. Reproduced from [Zhang et al, 2012].

2.4.2 Batch mode

The batch mode has been used widely in literature to obtain saturation kinetics. Besides its experimental simplicity and versatility, it also presents many advantages for kinetic studies; only one experiment gives at least 4 selectivity (H_2, O_2, CH_4, and CO), and well-defined saturation trends, making data fitting models able to introduce more reaction parameters. Typical time-scales chosen vary between 4 and 36 hours, depending on the material, catalyst load, reactants concentrations and reactor conditions, among others. A classical reaction progression is presented in Figure 2-12; reaction curves are sometimes reduced to the maximum yield rate.

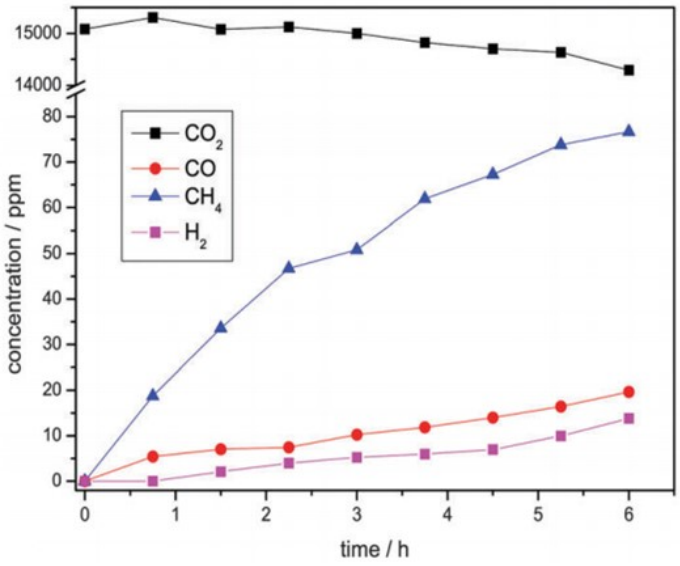

Figure 2-12 Saturation kinetics in a typical photoreactor for CO_2 reduction with water vapors. [Pougin et al, 2015].

It must be noticed that the outcome of the reaction is highly unpredictable [12]. Each reactor design needs trial-error optimization to obtain saturation curves in reasonable times for different materials. In an effort to standardize this situation for P25, Pougin et al (2015) presented a so-called standard conditions for CO_2 reduction in P25, which is going to be of particular interest for the rest of this work [3]. To illustrate how difficult can it be to either design a reactor geometry or find a suitable model for surface reaction, a comparison in Table 2-3 is presented for this type of reactor for different materials and conditions; in some cases the difference in performance by adding a co-catalyst can vary up to three orders of magnitude.

Table 2-3 Summary of photocatalytic activities for CO_2 reduction, measured experimentally for different materials in batch reactors with water vapors. Adapted from [Ma et al, 2015]

Photocatalyst	Structure	Main Product	Yield [μmol g^{-1} h^{-1}]	Year

0.1% Cu-TiO_2	Powder	CH_4	0.08	1994
MWCNT-TiO_2	NP on NanoTubes (NT)	HCOOH	18.7	2007
0.15%Pt-TiO_2	NP on NT	CH_4	0.66	2009
Au-TiO_2	Np on film	HCHO	1.36	2011
Pt-TiO_2	NP on NT	CH_4	25	2011
0.27% graph-TiO_2	film	CH_4	500	2011
$CuPt_2$-TiO_2	internally coated NT	CH_4	134	2012
0.2 % Au-TiO_2	mesoporous powder	CH_4	1.5	2012
0.2%Pt-TiO_2	mesoporous powder	CH_4	2.81	2012
Pt-TiO_2	NP on thin film	CO	190	2012
0.1 %Ag-TiO_2	mesoporous powder	CH_4	0.8	2012
$PtCu_2O$-TiO_2	core shell NP on powder	CO	8.3	2013
Cu-TiO_2	NP on wafer	CO	24	2014
$AuCu_2$-TiO_2	film	CH_4	2,200	2014
0.5 % Au-TiO_2	NP on powder	CO	1.5	2014
0.5%Pt-TiO_2	NP on powder	CO	1.1	2014
Pt-TiO_2	NP on wafer	CH_4	28	2014
Pt-TiO_2	NP on NP	CH_4	60.1	2014
0.5 %Ag-TiO_2	NP on powder	CO	1.7	2014
0.5 % Pd-TiO_2	NP on powder	CO	1.1	2014
0.5 % Rh-TiO_2	NP on powder	CO	0.62	2014
10 %In-TiO_2	NP	CO	230	2015

2.5 Supporting photo-active materials

2.5.1 Motivation

As most of photocatalysis applications requires the material to be nanoparticle sized, its implementation as a feasible technology must meet the criteria and limitations of industry, both for liquid or gas phase applications. Although nanoparticles suspension may present a higher exposed area, they are very difficult to separate from processes stream, and hard to illuminate evenly. Separation technologies for nanoparticles (5-100 [nm] size) or agglomerates (<1 micron), are not efficient enough in practice [30, 31].

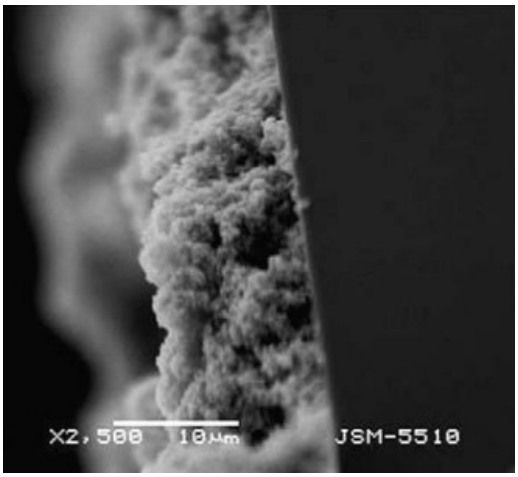

Figure 2-13 SEM imaging of TiO_2 thin dip-coated films. Reproduced from [Stefanov et al, 2011].

The use of mechanical stable supports fixing the photo-active material could help eliminating phase separation process. This has motivated the use of several different inert supports to facilitate practical applications of photocatalysis to different fields. Typical supports include glass, silica gel, quartz optical fibers, glass fiber, steel meshes, ceramic monoliths, and others [24, 32]. In this work, we will make an emphasis in the enhanced mechanical stability and optical properties of supported active films compared to bare powders. Typically, bare powders has undesired fluidization in typical batch photo-reactors, and are poorly illuminated since the catalyst load is not well controlled.

2.5.2 Immobilization Techniques

Since some key properties in photocatalysis are affected when an active material is supported, the design of supported films should be carefully engineered taking into account the interplay between optical properties, specific area and photocatalytic activity [30]. Although it is inevitable that light attenuation and aggregation limits the

use of immobilization techniques, later on this work we will demonstrate that with the proper design based on optical principles, supported films can unravel intrinsic activity of the different materials including P25. In this way, the reproducibility and the controllability of film thicknesses and porosity are the key features to take into account. Below a description of the different immobilization techniques available to deposit previously synthesized nanoparticles to inert substrates.

Evaporation: A given volume suspension is poured into a glass substrate and allowed to dry out, typically at 100 [°C] for few hours, or more if ambient temperature is chosen to avoid cracks. After drying, the supported material must be fired at temperatures of 400 [°C] or more to calcine any remaining solvent or stabilizers [33]. A major drawback of this method is the poor tunability of both the surface load and porosity. However, it results particularly simple and practical if high surface loads are preferred.

Dip-coating: A suspension is initially prepared with a stabilizer and the particles to be deposited. Subsequently, a dip-coater apparatus completely submerges and withdraws the substrate into the solution at linear speeds varying from 5[mm/s] to 2[mm/min]. The optimal composition of the slurry and withdrawal speeds must be optimized by trial and error most of the times based on the physical properties of the final films [32, 33, 34]. Advantages of this method includes the versatility to be used with different geometries and nano-crystalline catalyst geometry, the uniformity and transparency of the films, and the linear increase of the surface load with coating cycles.

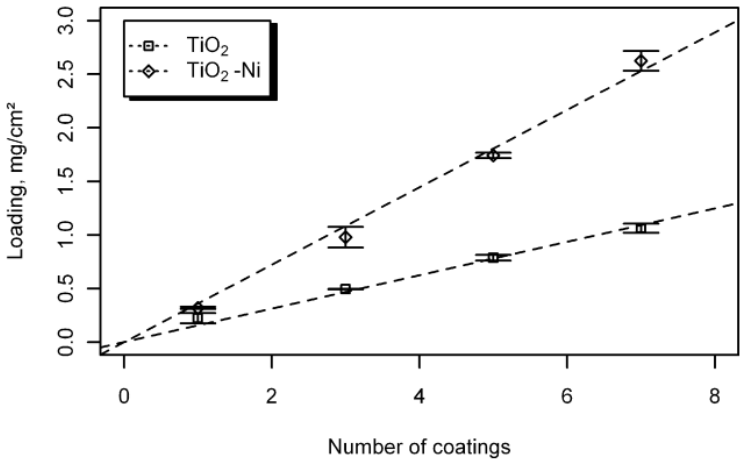

Figure 2-14 Increase of catalyst load with dip-coating cycles. Reproduced from [Stefanov et al, 2011].

Spin-coating and Langmuir-Blodgett (L-B) film: Although both methods will not be addressed in this work, they are useful for applications where the desired thicknesses of the film is in the hundreds of nm scale. Spin coating is based on centrifugal sputtering of a solution of similar characteristics to the ones used in dip coating. Rotation speeds are in the order 3,000 RPM. L-B films is based on two-phase interactions. It consists in isothermal compression cycles that are applied to a suspension of the active material over a sub-phase media. Subsequently, the upstroke of the substrate takes place through the film and produces highly ordered layers of active materials, achieving depositions as small as 100[nm] thickness [35, 36].

2.6 Intrinsic kinetics in CO_2 photocatalytic reduction

Intrinsic kinetics studies are not accidental works in the field of photocatalysis. Recently, these concepts have gained increasing attention since it is in part what makes photocatalytic experiments results so inconsistent compared to others. The influence of external factors, such as contamination, light intensity heterogeneity and mass transfer

limitations screens the inherent activity of different materials for CO_2 reduction [37]. Intrinsic kinetics in photocatalysis refers to measured reaction rates that are independent of the reactor size and configuration [37, 38]. While some external influences can be easily extrapolated to other cases, i.e., reactor volume, some others have an inherent influence in the calculated kinetic parameters, and its deconvolution requires a precise modeling of the physical properties and geometries of the setup that is used in a particular experiment. It must be noticed as well that scaling-up procedures cannot use kinetic parameters that were not obtained having an appropriate treatment of the influence of external parameters, such us photon flux, concentration gradients, velocity fields, etc. [37] .

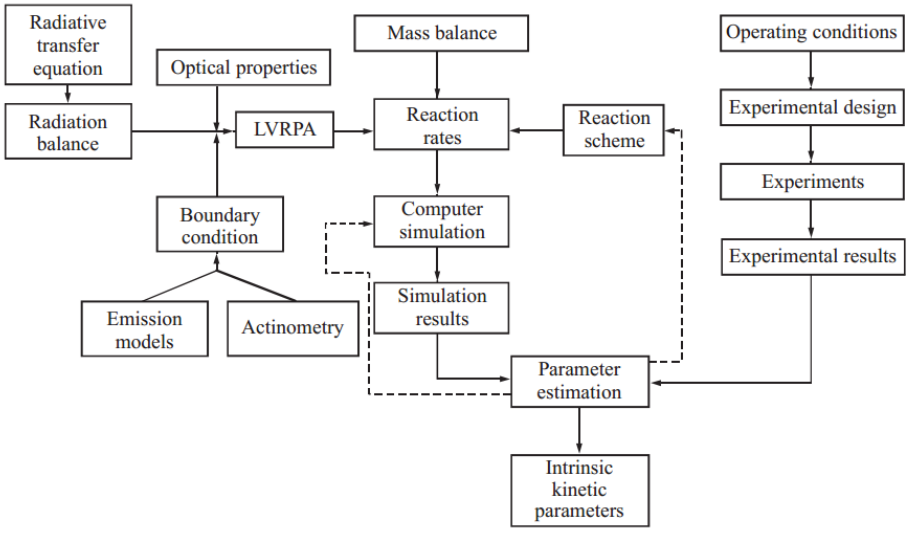

Figure 2-15 Intrinsic Kinetics methodology in liquid media photo-reactors. Reproduced from [Zalazar et al, 2005].

Besides the work of Zalazar et al (2005), and other earlier contributions that have addressed this issue in water decontamination technologies, many other authors have

followed a similar approach in an effort to characterize the different interdependent factors in photocatalysis [33, 38, 39]. For instance, this concept applies similarly to liquid water CO_2 photo-reactors. The methodology used by the original author to solve such interplay is presented in Figure 2-15. Assuming a reaction scheme and initial guesses for reaction parameters, differential mass and radiation balances are performed to calculate Local Volumetric Rates of Photon Absorption (LVRPA) and thus reaction rates. Using computational methods, the reaction parameters were finally fitted free of all the external phenomena.

On the other hand, external phenomena in gas-phase reactors are not quite the same; this will be discussed more in detail in Chapter 3 and Chapter 5. Even so, there has been an increasing effort to characterize mechanistic details of CO_2 photocatalytic reduction. Many authors have made an effort using more through coarse-grain representations, yet the lack of intrinsic kinetics concepts on those works undermines the validity of such fitted parameters [14, 24, 40]. Additionally, experimental good practices to avoid contamination are not always addressed. Contamination is fully addressed in the work of Pougin et al (2015) and stablishes a good set of practices to avoid biasing measurements with any foreign compound [3].

Therefore, a similar methodology will be developed in this work to take into account contamination free experiments, optical characterization and mass transfer calculations applied to water-vapor reactor for photocatalytic CO_2 reduction. As a case of study, this will be applied to P25, which is the baseline material for almost every photocatalysis application.

2.7 Surface reaction models

2.7.1 Motivation

A final piece for intrinsic activity characterization that deserves special attention is the validity of the surface reaction model used. Typically, most authors assumes Langmuir-Hinshelwood (L-H) kinetics expressions for CO_2 reduction processes, which main assumption is a pseudo-steady-state of both regular and photo-desorption steps [41]. An excellent discussion about the validity of these coarse-grain models is presented in the former work of Emeline et al (2005). Although the nature of regular L-H parameters have a different physical meaning, they can be used interchangeably with more rigorous definitions for photocatalytic rates, taking into account that L-H parameters are not actual gas-adsorption based; in some cases these simple models stablish good local reaction curve fitting, and the dependence of light as well [42, 43, 44].

Nevertheless, this reaction is far from simple and mechanistic information is necessary to not only predict the local behavior of such phenomena. It will be discussed in Chapter 6 how coarse-grain models like L-H break down under extreme cases, and how more detailed models can predict not only gas-phase products that are measurable, but also key intermediates. This is a tangential work to intrinsic kinetics, but equally important for further optimization studies, whose objectives do not only include characterizing intrinsic activity at local conditions, but also predicting trends out of the experiment boundaries. In this way, Microkinetics Analysis (MKA) have been applied to similar reactions and provides more insight of limiting-steps [45, 46], and provides a

powerful tool to predict better experimental conditions for further optimization studies [47].

2.7.2 Reaction mechanisms

Both experimental and theoretical works have tried to describe the reaction mechanisms for CO_2 reduction in semiconductors. For example, in situ spectroscopy measurements using diffuse reflectance infrared Fourier transform (DRIFTS) have been done last years in order to identify the intermediate reactions for different materials and reactants more accurately but, aside from giving a sense of what are the intermediates species formed, such as formic acid (HCOOH, $HCOO^-$), dissociated water (OH^-, H^+), CO_2 anions and carbonates (H_2CO_3, HCO_3^-, CO_3), these works remain unexploited due to the vague quantification of the amount of intermediates formed and the difficulty of integrating very different time scale processes at the same time, when representing this reactions analytically [18, 48].

On the other hand, theoretical calculations have made great progress on predicting the mechanisms by which those intermediates are formed [49, 50, 51, 52]. For instance, He et al (2010) have identified a minimum energy pathway (MEP) based on Density Functional Theory (DFT) calculations for different adsorption modes of CO_2 adsorbed in presence of previously dissociated water in TiO_2 Anatase (101) surface [52]. Their findings are shown in Figure 2-16 and describe the possible reaction pathway assuming the formation of formic acid as the limiting step and considering two competitive electron transfer reaction involving neutral and charged CO_2 adsorbed species. Even though they achieved remarkable predictions, i.e.: the potential needed

for the formation of undissolved CO_2^- , no other study has accounted this information to elaborate a unified model at least for TiO_2 based catalysts.

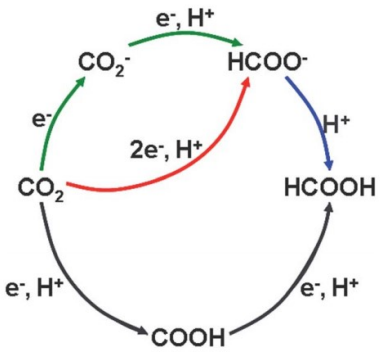

Figure 2-16 Elementary steps of photocatalysis. [He et al, 2010].

Moreover, He et al (2010) and later works did not consider the previous formation of active species like protons, neither the availability of electrons in surface traps available for reaction. Initially, the movement of free generated charges through the bulk of catalyst can be well described by solid-state physics principles, such as diffusion-drift equations and non-equilibrium fermi statistics [53, 54]. On the other hand, the nature of redox reaction rates explaining the formation of active species at the surface is better addressed by semi-classical theories for electron transfer, for instance Marcus Theory [55]. In this way, a more inclusive approach to model such interplay was proposed by Liu et al (2011), Monllor-Atoca et al (2007), and other authors [9, 56, 57]. Starting from elementary redox steps, more meaningful reaction rates were obtained for the formation of intermediates involved in organics degradation. In Figure 2-17, a representation of the "Indirect-direct model" is presented. In this model, the stationary-states of charge carriers is the key assumptions to obtain explicit reaction rates. Although CO_2 reduction is in principle different to organics degradation,

intermediate active species like hydroxyl and protons are common precursors, which makes these approaches particularly useful to describe the way the free or trapped holes attack an electron donor (*Direct Transfer* (DT) are hole attack mechanisms without trapping, *Indirect Transfer* (IT) is the attack of holes with previous trapping. *INS* means inelastic electron transfer to adsorbed species, and *ADB* are adiabatic electron transfers to dissolved species in liquid media).

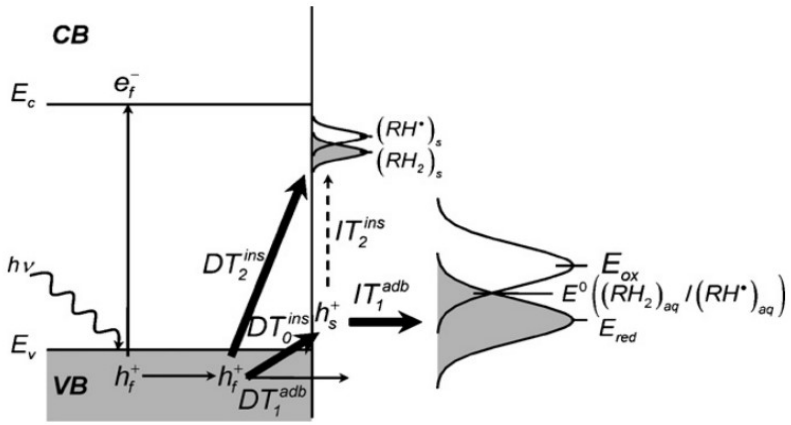

Figure 2-17 Elementary steps of photocatalysis. [Monllor-Atoca et al, 2007].

2.8 Conclusions

By the end of this literature review, we can conclude that besides the interesting application of photocatalysis to the field of solar fuels, CO_2 photocatalytic reduction still presents major limitations to become a feasible solution to either mitigate CO_2 emissions or transforming solar energy into higher value compounds [2]. The nature of the photocatalytic reaction involves semiconductor physics, redox reaction phenomena and classical reaction mechanisms at different time-scales, which makes this type of reactions a complex system; determining a priori which aspect of those steps is more limiting is still a hard undertaking. For instance, fast surface recombination has been

pointed out in literature as one of the main limitations for this reactions to have better Quantum Yield (QY) and Product Yields [4].

Regardless of the above facts, the rewards by implementing CO_2 photocatalysis to produce solar fuels are still thrusting a constant search for better materials to enhance particular aspects of the reaction, namely enhanced charge separation or electron-transfer rates [14]. In this way, P25, a widespread polycrystalline form of TiO_2, is usually a baseline reference to compare the photocatalytic activity for CO_2 reduction of any new material. However, neither in P25 or more complex material composites the influence of external factors in such slow reaction rates has been extracted. Moreover, it is clear that the influence of light is important since is the driving force to form free-charges. The influence of light intensity has been analyzed by simple reaction models showing at least a square root dependence to the local light intensity [42].

Consequently, the aim of the following chapters will be to re-define the intrinsic activity of P25 CO_2 photocatalysis in batch reactors with water vapors. Such scheme has several advantages controlling incident light intensity and analyzing reaction mechanisms. The load of the catalyst will be controlled by a dip-coating technique which allows to obtain thin porous films of catalyst and tune optical properties [58]. Engineering optical properties of the films we hope to get rid of light intensity influence using a simple reactor setup and models for light attenuation. Finally, part of the methodology to unravel intrinsic kinetics also involves quantifying rigorously the influence of mass transfer in the reactor [37]. This will be done using different dimensional analysis of transport equations with reaction curves obtained from

photocatalytic measurements, which makes the analysis general and applicable to other cases where the influence of diffusion is evidently more important.

Additionally, in light of this review, a discussion about reaction mechanisms is also an essential part of the work. Reaction mechanisms in P25 are still matter of debate, which has generated a wealth of theoretical and experimental literature about specific steps. However, in literature those aspects are obviated by approximating reaction rates to coarse-grain approximations [23, 41]. Such expressions are useful to locally fit the data of a specific experiment, and to roughly estimate the influence of light intensity only. Those models do not provide any insight about intermediates and limiting steps. By combining different mechanistic models for three different time-scales, we hope to find a relation between those first principles with macroscopic reaction rates. The computational apparatus chosen to represent that relation will be Microkinetics Analysis (MKA) [46]. A proof of concept will be performed using MKA to show how divergent trends can be qualitatively explained using reaction mechanisms information.

CHAPTER 3

LIGHT EXTINCTION AND OPTICS COUPLED REACTOR DESIGN

3.1 Light influence in photocatalytic rates

In this Chapter, the interplay of light and observed reaction rates will be decomposed. It was described in Chapter 2 that the influence of light in photocatalysis is key since it is the initial driving force that produces free-charges that migrate to the surface of the material [10]. A theoretical background will be presented describing simple ways to decompose the intrinsic dependence of reaction rates to local light intensities and light propagation phenomena. Taking these concepts into account, a simple way to characterize optical properties of an active film of material will be proposed together with its fabrication techniques. By the end of the chapter, two forms of loads will be proposed to be tested on its activity for CO_2 photocatalytic reduction, facilitating the later deconvolution of light influences.

3.1.1 Light dependent reaction rates

In Chapter 2, it was shown that photocatalysis is inherently light dependent since the initial step is the electron-hole pair generation. However, the dependence of reaction rates to light intensity, or photon flux, it is uncertain. From theoretical works discussing the coarse-grain behavior of redox reactions it was highlighted that coarse-grain approximation for photo-reduction phenomena in semiconductors are equivalent to an

apparent L-H expression, whose kinetic constant is proportional to a power of the light intensity. A basic expression is presented by Emmeline et al (2005) in Eqn. 3-1, and summarizes photo-oxidation of species in semiconductors in the absence of recombination (light absorption, excited state decay, and photoreaction) [42].

$$v_{OX} = \frac{k_{abs} k_r \Phi [S][M]_{ads}}{k_d + k_r [M]_{ads}} \qquad \textbf{3-1}$$

$$S + hv \rightarrow S^* \qquad k_{abs}$$

$$S^* \rightarrow S \qquad k_d$$

$$S^* + M \rightarrow Products \qquad k_r$$

Where

v_{ox} : Net oxidation rate.

K_{abs} : Absorption constant given by the wavelength of photon flux in surface.

K_r : Reaction between adsorbed reactants and excited active sites.

Φ : Photon-flux in surface.

K_d : Rate of excited states decay.

$[S]$: Active sites concentration in surface.

$[M]_{ads}$: Surface concentration of adsorbed reactants.

In despite of the equivalence between the Eqn. 3-1 and standard L-H models in literature [24, 40, 41, 59], this model contains several implicit assumptions that limits its validity. For simplicity, we will consider this expressions locally valid for the purposes of optical controls, but, it must be kept in mind that L-H kinetics is just a coarse-grain representation assuming a Quasi Steady State and a limiting step, which is not always the case. This misconception that an L-H model universally applies to any data regression to kinetic parameters is a more entangled problem that will be addressed in Chapter 6, and it is briefly outlined by Emmeline et al (2005). The modification of such expressions considering recombination is presented in Eqn.3-2 and Eqn.3-3.

$$rate = k_{L-H}\frac{K_L c}{(1 + K_L c)} \qquad \textbf{3-2}$$

$$k_{L-H} = k_{L-H,0} \times \left(\frac{\Phi}{\Phi_0}\right)^{\beta} \qquad \textbf{3-3}$$

Where

$k_{L\text{-}H}$: Apparent Langmuir reaction constant

K_L : Apparent Langmuir adsorption equilibrium constant

c : Single reactant concentration

$k_{L\text{-}H,0}$: Reaction constant at known photon flux condition (Φ_0)

β : Semi-empirical factor for the local photon flux dependency

Whether it be detailed surface reaction steps or a coarse-grain L-H model, it is evident that light intensity has an important role in CO_2 photo-reduction. In this way, for the subsequent optics modeling, we will use the definition of a semi-empirical β. For simplified limiting cases, β can be 0.5 for recombination dominated reactions (high illumination), and 1 for ultrafast redox reaction (low illumination) [43, 56].

3.1.2 Light Propagation in media

The semi-empirical relations described in Eqns. 3-1, 3-2 and 3-3 only describe the reaction rate in terms of the local photon flux perceived by the active surface of the photo-active material. However, in real reactors, light propagates under optical principles from the source to the walls of the supporting structure, which has drastic consequences in the light profile formed along the reactor.

The set of equations that describes this profile can be obtained solving the Radiative Transfer Equations (RTE), taking into account two main phenomena: light scattering and absorption. A more general case of light propagation is presented in the work of Pareek et al (2003). The core of the model is presented in Eqn. 3-4 , together with its numerical resolution for the Local Volumetric Rate of Energy Absorption (LVREA) of a liquid media photo-reactor study case [60].

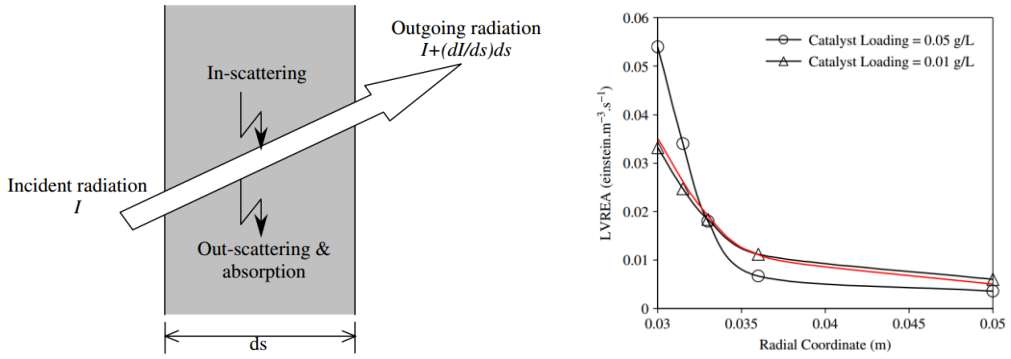

Figure 3-1 Radiation Field Balance Model. Reproduced from [Pareek et al, 2003]. Left: a scheme depicting the differential balance of light, where W_a is the light absorbed, W_e is the light transmitted, and W_{in} and W_{out} are in and out scattering respectively. Right: a numerical solution to the model of a study case liquid reactor with different concentration of nanoparticles suspended. The reactor solved is an annular geometry illuminated from the center. The results shows the radial decay of light intensity averaged in the Y-axis.

$$\frac{dI_v}{ds} = -W^a + W^e + W^{in} - W^{out} \qquad \textbf{3-4}$$

Furthermore, these models can be also solved for other type of reactor media and geometries, like the one presented in the work of Hossain et al (1998) [61]. In this last approach the author defines a generic media, and a monolithic photo-reactor geometry with homogeneous nanoparticles film coating its walls. In fact, their numerical results in Figure 3-3 are consistent with the experimental evidence presented in Figure 3-2. In this last experiment, an externally illuminated monolithic gas-phase photoreactor presented significant differences in CO and CH_4 yield depending on the monolith channel aspect ratio used. Although the author attributed this difference to mass transfer effects, considering the evidence just presented it is more plausible that this was due to the light profile obtained using different geometries.

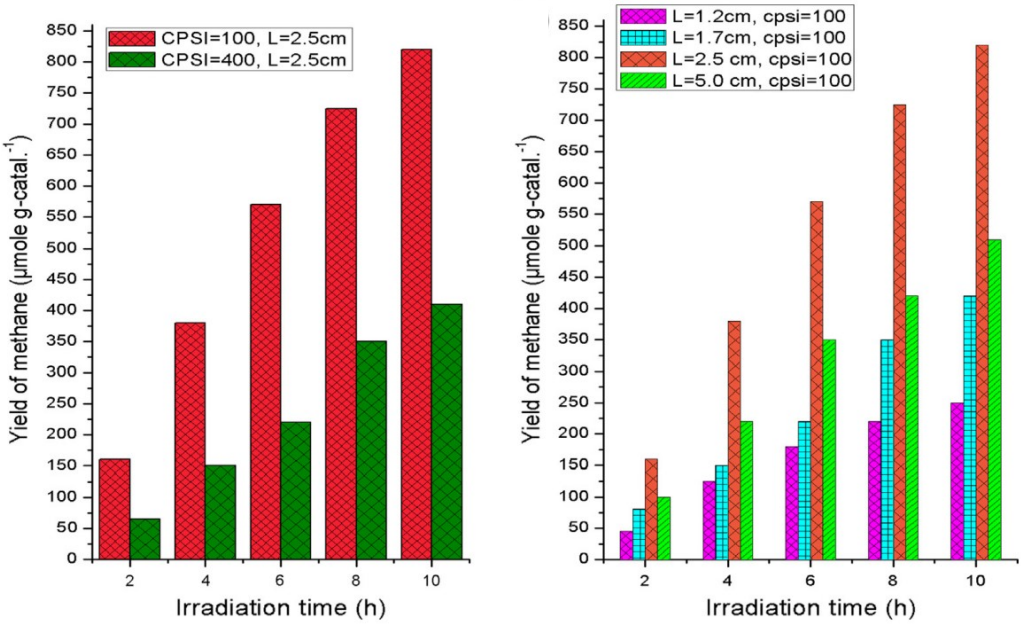

Figure 3-2 Influence of monolith channel length/width aspect ratio in photocatalytic activity. Reproduced from [Tahir and Amin, 2013]. Left: Influence of using different channels meshes (L=2.5 cm) in methane production. Right: Influence of using different channels length (CPSI=100) in methane production.

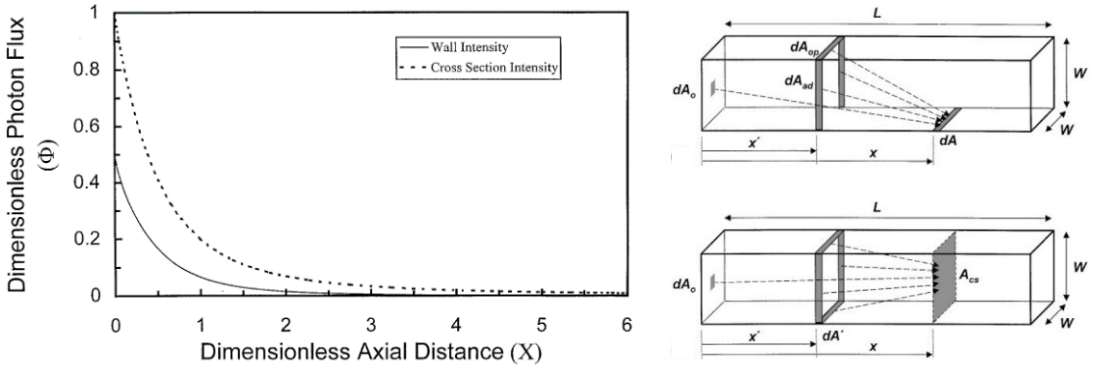

Figure 3-3 Radiation Field in a Monolithic photo-rector. Reproduced from [Hossain et al, 1999]. Left: non-dimensional photon flux decay along channel length axis (cross sectional and incident light in wall). Right: depiction of the RTE differential form in the monolith.

Nevertheless, this type of models that describe the light propagation in a 3-D media are in practice just qualitative, because accurate estimations for the LVREA can only be obtained using numerical methods. Such methods cannot be extrapolated because are geometry dependent, and requires a thorough description of both the geometries and material properties including active films optical and physical properties, which are often difficult to estimate ab-initio.

For these reasons, in order to simplify the intrinsic-kinetics in a batch-gas-phase photoreactor we will use the dip-coated films approach described in Chapter 2. Besides the mathematical modeling issues, in practical terms 3-D supporting structures enormously increase the catalyst loading but a main fraction of the material have poor light utilization [23, 24, 60-63]. In contrast, dip-coated films are in practice small loads with high optical utilization, and with a simple solution for the LVREA which simplifies the optical analysis to light propagation through a thin film only. The incident light intensity in a film can be obtained using the Linear Source Spherical Emission model, which only depends on the substrate characteristic length and the distance to the light-source. At typical laboratory scale geometries, the incident light can be considered constant along the surface of the film and measured with a typical radiometer in-situ [33].

3.1.3 Light Propagation through thin films

Besides how local light propagates to the surface of the active material, the question of how light propagates from the top to the bottom of the films is still unanswered. Although the principles are the same as the ones presented in Eqn. 3-4, the

solution to the balance simplifies to an exponential decay (Eqn. 3-5) dependent on two main phenomena: Rayleigh Scattering and Bruggeman molecular light absorption.

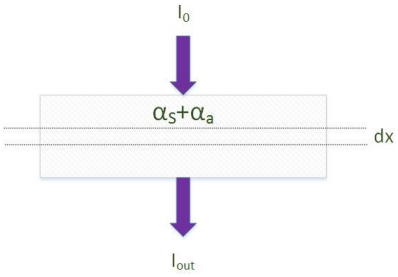

Figure 3-4 Light extinction in thin meso-scale crystal composites

$$\frac{I_{out}}{I_0} = \exp(-\alpha_E x) \qquad \textbf{3-5}$$

In Eqn. 3-5, the exponential decay has to contributions. One coefficient for the attenuation of light by absorption, α_A, and a scattering contribution α_S. The sum of them both gives the total extinction coefficient α_E. For instance, if Rayleigh Scattering is small in a film, the attenuation of light through the film can be approximated to pure effective absorption; Bruggeman Theory for instance predicts that molecular light absorption can be an effective the apparent Beer-Lambert's presented Eqn. 3-5 [62]. However, in meso-crystals the absence of scattering is rarely the case. This has serious implications in photocatalysis since not all the optical properties needed to calculate effective reaction rates can be reduced to the Transmittance of the film. In other word, not all the light extinction produces reaction in Eqn. 3-2.

Since the scattering coefficient of the film is seldom an important factor affecting the external influence of light in reaction rates, the contribution of both phenomena must be decoupled. In this way, the work of Usami and Ozaki (2005)

provides a good insight into semi-empirically describe Rayleigh Scattering in films. They describe Rayleigh Scattering as the deflection of light in nanoparticles composites due to the dipole fields created when the characteristic radius of the particle is much smaller than the wavelength of light [58]. They do not only provide the specific contribution of Rayleigh Scattering to attenuation in a single film, but also an useful trend for this relation if optimization of catalyst loads are pursued and the scattering properties of the films are uncertain beforehand. For instance, we will reduce their analysis to the simple extrapolation of scattering of the visible range when Diffuse Transmittance/Reflectance UV-Vis experiments are performed in the films using a spectrophotometer. In Figure 3-5, by extrapolating the trend of wavelengths larger than the bandgap of the material to the absorption range, the contribution of scattering and absorption can be obtained.

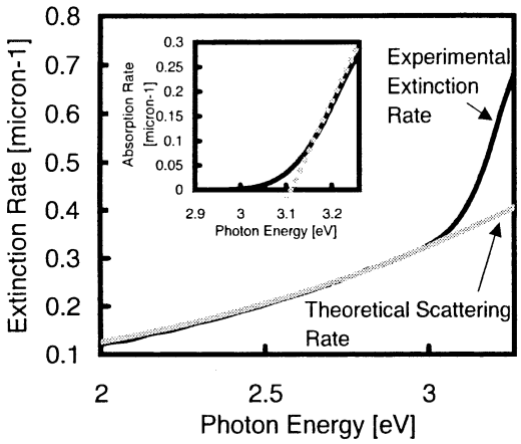

Figure 3-5 Extinction, scattering and absorption rates of a P25 moderate thickness film. Reproduced from [Usami and Ozaki, 2005]. Main graph shows the comparison between experimental extinction rate and the predicted scattering contribution. They both overlap in the visible range and the theoretical prediction of scattering shows the trend for wavelength higher than the bandgap. The secondary graph shows the calculated effective absorption rates.

3.2 Catalyst load preparation

Considering the simplified optical characterization when testing photocatalytic activity of thin films, the catalyst load will be prepared using dip-coating glass substrates. The thin P25 films were prepared using the work of Stefanov et al (2010) as a reference [34].

An initial solution was prepared using 4.26 [gr] of Degussa P25, and 4.26[gr] of Polyethylene Glycol 6000 (PEG 6000) into 80[ml] of reactive grade ethanol. The resultant solution was 7% w/w in P25 and 7% w/w in PEG 6000 as the original work. Then, regular 1[in] x 2.5[in] microscope glass-slides were meticulously washed with DI water, acetone and alcohol to eliminate any organic or dust, and then dried with compressed air. Previous to the dip-coating process, the slides were also fired at 400[°C], cooled down to room temperature on a desiccator, and finally weighted.

The dip-coating process was done considering one and two coating cycles. Each coating cycle consisted in attaching one extreme of the glass slide to the sample holder of an own-built dip-coater apparatus. The slide was then submerged and withdrawn at a speed of 1[mm/s]. The slides were then carefully extracted and put to dry at 15 [°C] for one hour. After that time, the samples could be either calcined or dip-coated again. Finally, after all the slides were coated the desired number of cycles, the rear side of the slides was carefully cleaned, and the slides were put into the oven at 400 [°C] for 1 hour to calcine PEG. Finally, the slides were cooled down to room temperature on a desiccator and weighted.

Two samples were prepared in duplicate to test the reproducibility of the method. The Samples S1 are the ones that were dip-coated in 1 cycle, while S2 were

dip-coated two times. Additionally, a set of 2 blanks using the same solution without P25 were prepared also to make sure that by the end of the process the increase in weight was only due to the deposition of P25. The results are presented in Table 3-1, and compared with the results of the original author for the same number of coating-cycles.

Table 3-1. Results for dip-coated glass slides. Parameters of Reference were obtained from the work of Stefanov et al (2005).

Sample	Coating Weight [mg]	Area [cm^2]	Surface load [mg/cm^2]		Film Thickness [µm]	Film Density [mg/cm^3]	
			Exp.	Ref.	Exp.	Exp.	Ref.
S1-A	1.1	11.1	0.10	0.15	1.4	671	700
S1-B	1.0	10.9	0.09		1.6	601	
S2-A	2.2	9.4	0.23	0.25	2.1	1084	700
S2-B	2.0	10.1	0.20		2.6	773	

3.3 Thin film characterization

The film look homogeneous, and present a moderate mechanic stability and water resistant. Additionally, the characterization using a surface profilemeter showed a homogeneous thickness in the order of 1[µm] per cycle, consistent with the surface load increase per cycle calculated by weighting the microscope slides before and after coating. This would indicate that the mesoporous structures were preserved and that the specific area of the films is somewhat preserved [34]. Although BET experiment must be done to determine to what extent the specific area of P25 is lost from its initial value of approximately 50 [m^2/g], this is unpractical for such small amount of material. Only in supporting structure with appreciable catalyst load a BET specific area experiment

can be done. For moderate thickness and calcination, the loss in specific area has been reported to be small [32]. In this way, besides confirmation of the smoothness of the films in the nano-scale, an estimation of specific area could be done using either SEM or AFM imaging [33, 34]. In regards to optical characterization, a similar experiment to the work of Usami and Ozaki (2005) was performed using a UV-vis spectrophotometer equipment (Cary 5000). Measuring the diffuse transmittance of the film at different wavelengths, the contribution of scattering can be extrapolated from the pure-scattering range. The extinction coefficient for both phenomena will depend on the wavelength of the light source.

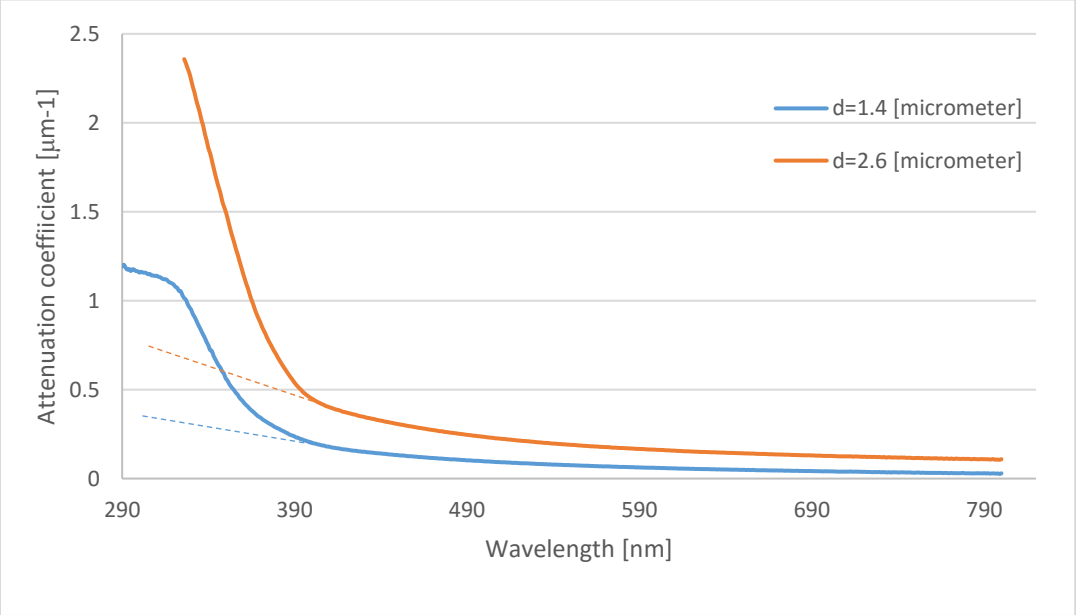

Figure 3-6 Extinction coefficient extracted from UV-Vis diffuse reflectance of Samples S1-A and S2-B. Dashed lines are the projections of the scattering contribution based on the work of Usami and Ozaki (2005).

3.4 Estimations for catalyst loading and reactor scale-up

3.4.1 Classical scaling

Taking into account both the dependency of reaction rates to light intensity and light attenuation concepts, it is clear that a tradeoff exists between the number of dip-coating cycles and the time-scales for typical batch experiment: the less material Monolayers (ML) deposited, the longer the time needed for the reaction curve to reach its characteristic form.

The most basic scale-up can be obtained as it follows. Assuming a perfectly stirred batch reactor and an apparent reaction rate at the bottom, the Eqn.3-6 describes the evolution in time are of the scheme presented in Figure 3-7

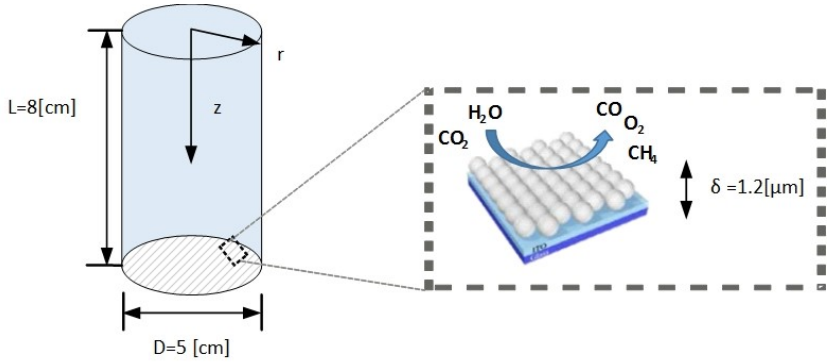

Figure 3-7 Reactor idealization scheme with own-built experimental setup dimensions

$$V_R \frac{\partial c_i}{\partial t} = \gamma_i \, (A_F \delta_F \rho_F) \, a \, k_{L-H} \, f_{L-H}(\boldsymbol{c}) \qquad \textbf{3-6}$$

Where

V_R : Reactor volume

c_i : Product (or reactant) concentration in time of species *i*

$\boldsymbol{c}$: Species concentration vector

$f_{\text{L-H}}$: Langmuir-Hinshelwood (L-H) expression as a vector-valued scalar function (non-linear)

$k_{\text{L-H}}$: Langmuir-Hinshelwood constant at incident light intensity

A_{F} : Glass substrate area at the bottom

δ_{F} : Active film thickness

ρ_{F} : Active film density

a : Specific area per gram of catalyst

γ_{i} : Reaction stoichiometry for species *i*

Particularly for this perfectly mixed case, the bulk concentrations are flat and also follow a stoichiometry using a parametrized reaction rate. Therefore, using the proper overall molar balance, the equation reduces to the following single non-linear ODE

$$V_R \frac{\partial c_{CO_2}}{\partial t} = (A_F \delta_F \rho_F)\, a\, k_{L-H}\, f_{L-H}\left(c_{CO_2}\right) \qquad \textbf{3-7}$$

Where the rest of the species are defined by stoichiometry as it follows

$$c_i = c_{i,0} + \frac{\gamma_i}{\gamma_{CO_2}}\left(c_{CO_2} - c_{CO_2,0}\right) \qquad \textbf{3-8}$$

Therefore, using a convenient characteristic time and concentration the math object obtained is now generic and presented in Eqn. 3-9 to 3-11.

$$\frac{\partial \tilde{c}_{CO_2}}{\partial \tau} = f_{L-H}\left(\tilde{c}_{CO_2}\right) \quad \textbf{3-9}$$

$$\tilde{c}_{CO_2} = \frac{c_{CO_2}}{c_{CO_2,0}} \quad \textbf{3-10}$$

$$\tau = \frac{V_R}{W_F\ a\ k_{L-H} c_{CO_2,0}} t \quad \textbf{3-11}$$

It is now clear that the time-scale of the reaction progression scales with the reciprocal of the catalyst loading W_F. Nevertheless, this classical scaling process did not consider the empirical relation between reaction constant $k_{L\text{-}H}$ and light intensity. This principle is in fact one of the reasons why baseline materials like P25 presented such low TOF in literature [23, 24, 40, 63, 64]. Most of this experimental literature uses bare powders or highly loaded substrates which in fact have an enormous amount of material not being used under optical principles.

3.4.2 Light attenuated scaling

The same non-dimensional analysis was performed to obtain a relation between observed rates and optical properties, but considering light attenuation laws and the proportionality $k_{L\text{-}H} \propto I^{\beta}$. Consider the scheme in Figure 3-5; the fraction of light attenuation along the film that produces reaction can be estimated at every x coordinate as described by Eqn. 3-12.

$$I_A = \frac{\alpha_A}{\alpha_A + \alpha_S} I_0 \exp(-[\alpha_A + \alpha_s]x) \quad \textbf{3-12}$$

Where

α_A : Light absorption coefficient

α_S : Scattering coefficient

α_E : Effective attenuation coefficient

I_0 : Incident light intensity at the top of the film

Then, the differential contribution to an apparent reaction rate using the relation in Eqn. 3-2 is defined in Eqn.3-13. Integrating the equation knowing the BC at x=0, the estimation for the apparent reaction is obtained in Eqn. 3-14.

$$dk_{app} = k'_{L-H,0} \times \mathrm{I}_A{}^{\beta} dx \qquad \textbf{3-13}$$

$$k_{app} = k_{L-H} \left(\frac{\alpha_A}{\alpha_E}\right)^{\beta} \frac{1}{\beta \alpha_E} \left(1 - \exp(-\beta \alpha_E \delta_F)\right) \qquad \textbf{3-14}$$

3.4.3 Discussion

Going back to the original equation, some useful relations can be obtained scaling-up the characteristic time terms. For example, using the same film for two experiments at identical conditions in a cylindrical reactor but changing the radius/height aspect, the time-scales will follow the next relation

$$t_{c,2}/t_{c,1} = \frac{L_{R,2}}{L_{R,1}} \qquad \textbf{3-15}$$

Which is the simplest scale-up equation predicted by the classical analysis as well. This predicts that the reaction time increases linearly with the height of the reactor.

Another important relation can be obtained by is using a very thick film in two experiments at different light intensities, assuming that exponential terms collapses to zero, which gives

$$t_{c,2}/t_{c,1} = \left(\frac{I_{2,0}}{I_{1,0}}\right)^{\beta} \qquad \textbf{3-16}$$

Additionally, if two films with different surface load S_1 and S_2 are prepared using the same procedures, and tested under identical conditions (assuming same optical properties), the following relation is obtained

$$t_{c,2}/t_{c,1} = \frac{V_{R,2}}{A_{R,2}} \times \frac{A_{R,1}}{V_{R,1}} \times \left(\frac{1 - \exp\left(-\beta\alpha_E \, S_2/\rho_F\right)}{1 - \exp\left(-\beta\alpha_E \, S_1/\rho_F\right)}\right) \qquad \textbf{3-17}$$

Eqn. 3-17 predicts that the reaction time does not increase linearly with the reciprocal of the catalyst load. In fact, just few optical depths α_E^{-1} are needed to achieve roughly the same results as a high load in the bottom of the reactor. It must be noticed that the specific areas of the films can decrease drastically by using deposition techniques. For thick coatings, it has been estimated in other works that the BET area of bare powders can decrease up to 5 times [32]. This loss of specific area is likely to increase when adding more and more layers of materials or when using high calcination temperatures. On the other hand, bare powders are seldom in form of aggregates that produces significant reduction of surface area, which is not quantified in most of the experimental literature; neither a suitable pre-treatment like sonication or milling is presented to ensure that the BET area presented is actually representative of the catalyst exposure under in-situ conditions. Therefore, the exponential decay due to optical

properties is probably far more detrimental than the loss of area when using supported materials. Additionally, in Chapter 2 was shown that some experimental literature in photocatalytic organic degradation literature has addressed this problem [33, 37, 38]. Although the reaction principles are very different compared to CO_2 reduction, some of the ideas that high catalyst loads present poor light utilization are still very similar. For example, in Figure 3-8, it can be seen that testing the photocatalytic activity of the material using high loads actually underestimates the intrinsic activity, which is the case in most of the literature about CO_2 reduction.

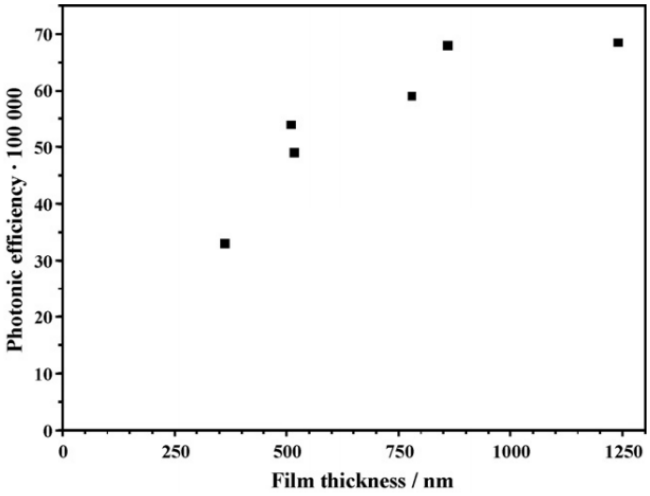

Figure 3-8 Plot of the photonic efficiencies of the methylene blue degradation for different films as function of film thickness. Reproduced from [Bennani et al, 2009].

3.4.4 Optical effectiveness

A novel way to quantify how far the apparent reaction rates are from intrinsic activities is what we defined an optical effectiveness factor (Φ_L). Similar to mass transfer effectiveness factors, this is defined as the ratio of the actual reaction

considering light attenuation to the ideal reaction considering all the active area exposed to the incident light.

$$\Phi_L = \left(\frac{\alpha_A}{\alpha_E}\right)^{\beta} \frac{1}{\beta \alpha_E \delta_F} (1 - \exp(-\beta \alpha_E \delta_F)) \quad \textbf{3-18}$$

Where a factor near 0 means total underestimation of intrinsic activity (optics limited), and 1 means intrinsic activity (reaction limited). This definition is also consistent for extreme cases when δ_F is very thin ($\Phi_L = \Phi_{max}$), only limited by the absorption/extinction ratio, and when it is very thick ($\Phi_L = 0$).

3.5 Election of loadings for photocatalytic activity measurements

3.5.1 Thick films

According to Eqn. 3-16, a simple experiment can be performed using a thick film under two identical conditions but illumination to test light dependency in CO_2 photocatalysis. The thickness of the film was chosen considering an arbitrary number that may give total attenuation of light. Using the same sonicated solution of 7% P25 and 7% PEG 6.000, a volume considering total evaporation was poured into a small petri dish with the glass substrate in the bottom. In order to have a reference, we calculated the height of the solution to achieve double the load used in the work of Pougin et al (2016) when the solvent evaporates, considering as well that their reactor was 4 times shorter. Then, the sample was left to ambient conditions to evaporate, and after 24 hours, it was calcined at 420 [ºC] for 2 hours. The final weight of the thick film was 95[mg].

3.5.2 Thin films

According to results in Figure 3-6, scattering increases enormously in films S2-A and S2-B. We chose the film S1-A due to its homogeneity, and better transparency. Although some significant amount of light is still scattered, the characterization of optical properties presented in Figure 3-6 still follows the scattering model presented by Usami and Ozaki (2005), and therefore can be decoupled simply by using Eqn. 3-12. After testing both the thick and thin films activity, an estimation of β and the optical effectiveness of the thin film will be calculated. If the effectiveness factor obtained is reasonable, then an estimation for the intrinsic activity of P25 can be stablished as a baseline for future studies.

3.6 Conclusions

In this chapter, using some of the coarse-grain models described in Chapter 2, we have defined first a quantitative relation between light intensity and local reaction rates in a photo-active material aggregate. This type of expressions is stablished as a first estimation to the interplay between light intensity and simply defined as $k_{L\text{-}H} \propto I^{\beta}$, where $k_{L\text{-}H}$ is an apparent Langmuir-Hinshelwood reaction constant, and β is a semi-empirical number [42].

Secondly, we have explored different models for light propagation, concluding that the best way to characterize the light intensity profile in the reactor is using the thin-film approach presented in Chapter 2. By using this form for the catalyst load, a set of complicated radiation balances simplifies to an apparent exponential decay through the film. It was shown that the contribution of scattering and absorption to this attenuation

of light is not trivial to model, but simple to approximate experimentally using the approach of Usami and Ozaki (2005) [58]. After producing dip-coated glasses, characterizing the films using a surface profilometer and a spectrophotometer, the parameters to extract the scattering part at different wavelength were obtained.

Finally, the influence of the simplified optics in the observable reaction rates was obtained by using a dimensional analysis. This not only has an influence in the intrinsic kinetics methodology but also in the correct design of the reactor needed for subsequent photocatalytic activity measurements. By including the attenuation of light in the definition of $k_{L\text{-}H}$, a set of useful scaling equations were obtained. Among them, the influence of light in two thick films (Eqn.3-15) and the novel concept of Optical Effectiveness Φ_L (Eqn. 3-18) were of key importance. Based on those equations, two appropriate forms for the catalyst were found of key importance to obtain the intrinsic activity of the material in the next section, which are thick and thin films (95[mg] and 0.64[mg] of P25 respectively, deposited in a 1[in]x1[in] glass substrate).

CHAPTER 4

P25 FILMS PHOTOCATALYTIC ACTIVITY FOR CO_2 REDUCTION

4.1 Experimental setup

The experimental setup was built following the same guidelines as the ones presented in Figure 2-11; general ideas of water-vapor reactors advantages for kinetic studies were already presented in Chapter 3. The specific features of our experimental setup are presented in Figure 4-1. The reactor was own-built using both Swagelok and NPT stainless steel connections, together with copper tubing and stainless steel fittings. Our adaptation also includes a glass bubbler, flowmeters and three different valve configurations modes: purge, initial load, and sampling.

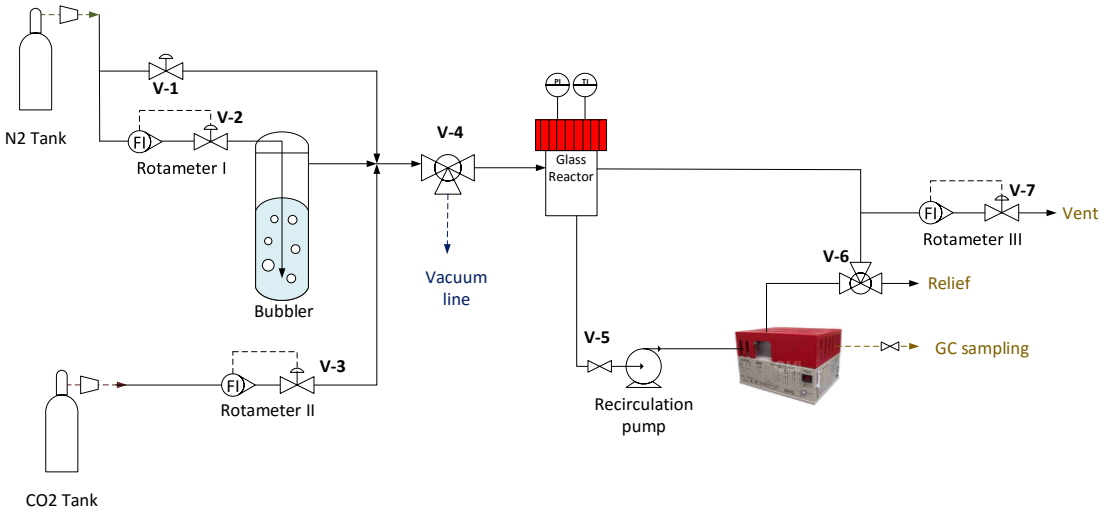

Figure 4-1 Own-built photo-reactor configuration. The different configurations are controlled by three-ways swage lock valves.

4.1.1 Glass reactor

Similar to most of the literature about CO_2 photocatalytic reduction, only metal and glass parts were used to seal the reaction chamber. Tight sealing was achieved using stainless steel adapters with internal NPT threads and O-rings compression seals. No plastic parts besides the rubber-quartz contact were used inside the reaction chamber. All peripheral piping surrounding the chamber was made of Swagelok connectors and copper tubing.

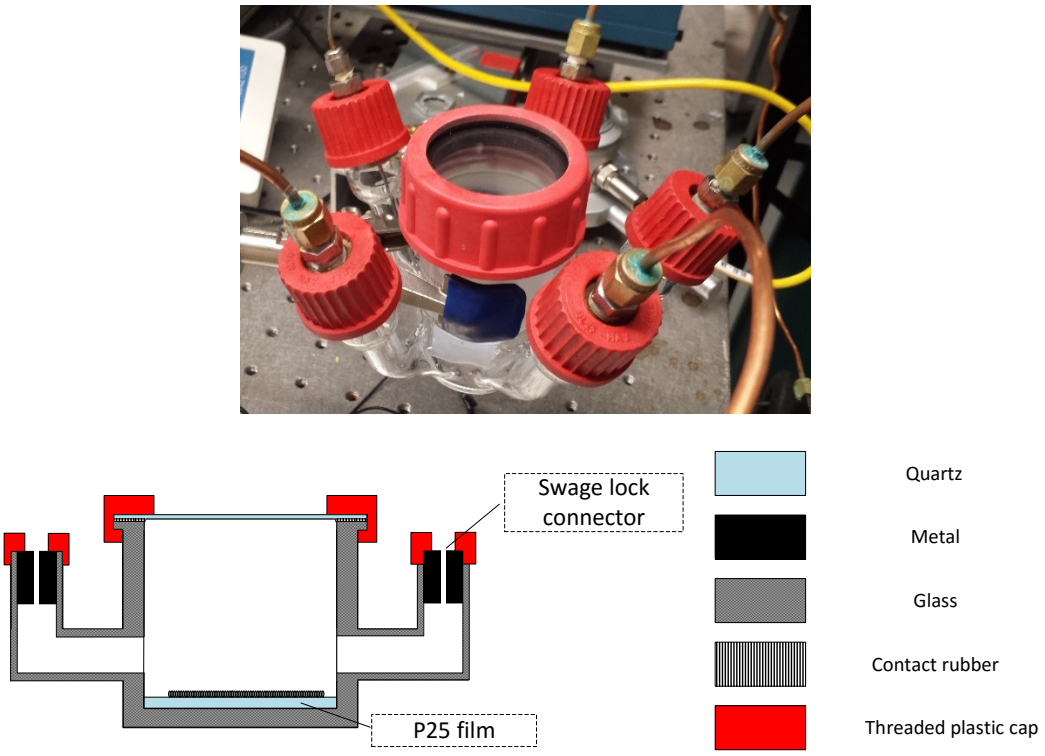

Figure 4-2 Own-built 5-ports photo-reactor glass cell. The total inner volume is approximately 120 [cm^3], and the height is 8[cm].

4.1.2 Illumination

The Illumination chosen was a 200 W UV LED chip. The incident light intensity was measured previous to all the experiments using a radiometer coupled to a hemispherical detector (Solar Co PMA2100). Additionally, the transmittance of the films was measured in-situ using this same device. Contrasting UV-Vis experiments in Figure 3-6 and in-situ transmittance of the film S1-A, the LED chip light source was estimated to have a sharp spectra between 365 and 370 [nm].

4.1.3 Gas Chromatography

The Gas Chromatography equipment used to analyze the concentration inside the reactor is a model SRI 8610C Gas Chromatograph. This equipment has an internal circuit that controls the sample injection in carrier gas (Argon) to the separation columns through a solenoid valve. The columns are packed with commercial materials that have different retention times for different species. As the expected species have dissimilar retention times, it is convenient to differentiate the separation process of the species that have a high affinity for typical commercial packing, like CO_2 and C_2 compounds. First, the sample is passed through a pre-column 1 (0.5m HayD), which has a very high affinity for CO_2 and C2 compounds. In a second moment, the flow is reversed through this column, letting pass only light compounds to a second column (1m MS5A). Without this procedure, CO_2 and C2 compounds would get stuck in column 1m MS5A. In column 1m MS5A, the species like H_2, CH_4, N_2 and O_2 are separated. In a second moment, another sample is carried by Argon to a third column (2m HayD), which separates CO_2 and C2 compounds.

The continuous flow of Argon that carries the species through the different columns goes finally to a TCD/FID detector. The Thermal Conductivity Detector (TCD) quantifies the thermal conductivity difference between carrier-gas-sample and pure carrier-gas. The flame ionization detector (FID) passes the carrier gas-sample flow through a Hydrogen Flame, which produces ions from combustive species that are detected in a current measuring circuit; the FID detector also has a methanizer incorporated to detect CO_2 and CO also. Both, TCD and FID lectures at different retention times can be associated with the relative concentration of species in the carrier gas.

In order to associate TCD/FID readings with the specific concentrations of the different species in the original sample, a set of calibrations were done using a calibration gas of a certified composition (Matheson Tri-Gas). At different dilutions, and after injecting samples directly to the GC internal circuit, the integration of the peaks at the retention times of the different species was registered. In most of the cases, the area under the peaks increases linearly with concentrations at the characteristic retention time of the species. Besides water and oxygen, all the lectures of peaks during CO_2 photocatalysis experiments were associated with calibration curves obtained using certified gas compositions.

4.2 Procedures

4.2.1 Catalyst pre-treatment

As part of the procedure replicated from Stefanov et al (2010), part of the dip-coating process is the removal of the PEG that was used to generate nanopores and

maintain mechanical stability. This process is referred in literature as standard calcination, and consists in heating the films up at 400 [°C] at 1 hour at atmospheric conditions to annihilate the stabilizer compound.

Additionally, as some remaining organics may prevail after this process, a pre-photocatalytic treatment was used to degrade any trace of carbon contamination. This was performed by introducing the film inside the reactor, and enclosing it at oxidizing conditions of 1.5 [bar] with 10% CO_2 and 0.6% $H_2O_{(g)}$. After keeping the reactor under experimental illumination conditions for 12 hours, 10 purges were made fully vacuuming and replenishing the reactor chamber with pure N_2 (all valves closed, manipulating V-1 and V-4 only). Furthermore, the pre-photocatalytic treatment is also necessary between experiments using the same catalyst; Pougin et al (2016) presented several evidence that some organics are strongly physorbed, or chemisorbed, after CO_2 photocatalysis experiments, which may produce additional formation of gaseous compounds in subsequent experiments if these heavy compounds are intermediates products.

4.2.2 Tight-sealing

An initial tight-seal test consisted in keeping a pressure of 2[bar] for 24 hours. No leak was, detected both under vacuum and positive pressure. Additionally, it was ensured that the small pressure drop during each experiment was due exclusively to the small volume taken by the GC in each sampling; keeping positive pressure during experiments is essential to ensure that the batch system is fully enclosed from the atmosphere.

4.2.3 Flushing mode

After pre-treating the catalyst and testing leaks, the reactor is connected to the GC by opening the valves V-1, V-4 (to reactor), V-5 and V-6 (to relief). An approximate flow of 1 [lpm] of N_2 for 10 minutes was used previous to all the experiments to flush any trace of previous products in the circuit. An initial GC sampling was performed previous to all the experiment to ensure that no trace of O_2, H_2, or carbon compounds remained in the system. In most cases, after the purge the traces were less than 1ppm.

4.2.4 Initial load and reaction

After flushing the GC circuits, the system is set up to blend CO_2 and N_2 using controlling valves V-1, V-3, and V-4 (to reactor), V-5 (open), V-6 (to recirculation) and V-7. The conditions of system pressure, ratio of flows, and output flow were previously identified to reach molar fractions of CO_2 ranging from 0.1% to 15% in the feeding stream. In this way, to achieve standard conditions proposed by Pougin et al (2016), a mixture of 3% CO_2 and 97% N_2 was prepared inside the reactor first. Then, the Valves V-1, V-3 and V-4 were fully closed, keeping the recirculation mode. After this initial load, the system was relieved to 1[bar]. Next, a slow bubbling condition was controlled using V-4 and V-2 to fill up the system with water saturated N_2, which water concentration at upstream pressure (17 [psig]) and temperature (25 [° C]) conditions is approximately 1.3%. When a 2[bar] pressure is obtained inside the reactor, the system is enclosed by closing Valves V-4 and V-2, and relieved back to 1.5[bar]. This gas mixture had composition equivalent to the desired standard conditions, which were checked afterwards with the GC measurement at the beginning of the experiment.

This procedure is flexible enough to achieve standard conditions highlighted by Pougin et al (2016), and other extreme cases of interest like high partial CO_2 pressures or water; being able to control the reactants ratio was remarked in Chapter 2 as one of the main advantages of water vapor reactors to perform kinetic studies compared to liquid water, because different data sets at different reactants conditions can be produced.

4.2.5 Diminishing sampling loses

Although concentrations inside the reactor does not change after sampling, the depressurization of the reactor due to sampling can certainly affect the partial pressures of both reactants and products. To avoid this, a small recirculation flow to the GC is constantly maintained, because isolated measurements typically need 10-20 [ml] of gas volume to displace previous samples. Using a small recirculation through the GC circuit, at 1.5[bar] and 25 [° C], the pressure loss after sampling is about 0.2[psi]. Therefore, the depressurization is only 1[psi] by the end of 5-6 samples, which is small enough to consider the experiment at constant total pressure of 1.5[bar].

4.3 Results

4.3.1 Results for thick films

After following the previous procedures, once the initial load and the reaction mode is set up, the UV light is turned on and GC automatic sampling is performed, obtaining the characteristic progression of reaction in time. These results for thicker films will be useful to quantify the dependency of reaction rates with light when the

transmittance of the film is practically zero. Additionally, before testing a film, blank tests using only nitrogen and light were performed to ensure that the progression of products is only due to CO_2 reduction.

Hydrogen Evolution Reaction (HER) tests were performed to make sure that under CO_2 free conditions no carbon compounds are formed. The thick film described in Chapter 3 was used, which has an area of 6.3 [cm^2] and a catalyst net weight of 95[mg]; this load was estimated considering a reasonable time-scale for the. The results both for HER and CO_2 reduction are presented in Figure 4-3, Figure 4-4 and Figure 4-5; it must be noticed that O_2 production is not presented since is just estimated for kinetics purposes using calibrations without a standard and stoichiometry calculations.

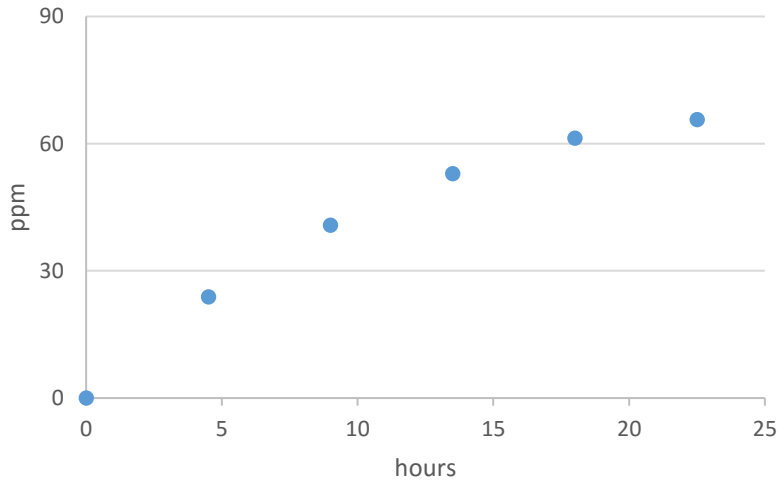

Figure 4-3 Hydrogen evolution on thick films. Experimental conditions: P=1.5 [bar], I=200 [W/m^2], T=30 [°C], 0%CO_2, 0.6 %H_2O

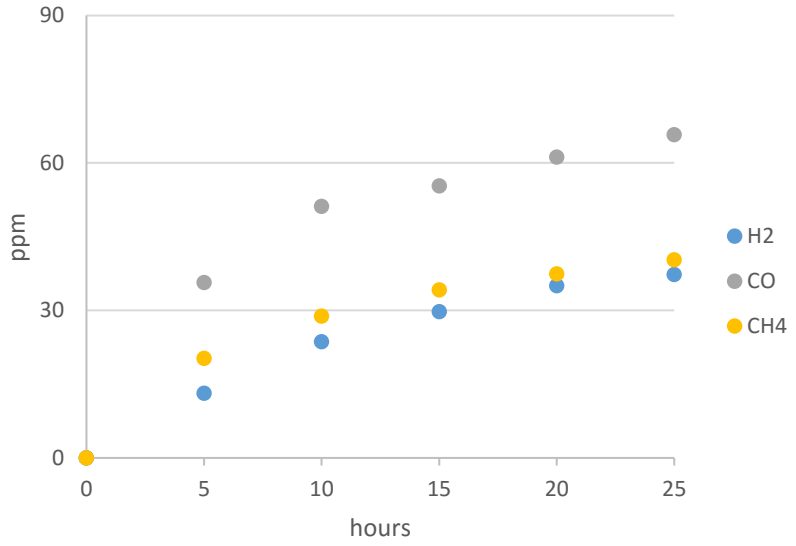

Figure 4-4 CO_2 reduction evolution on thick films. Experimental conditions: P=1.5[bar], I=200 [W/m^2], T=30 [°C], 0%CO_2, 0.6 %H_2O.

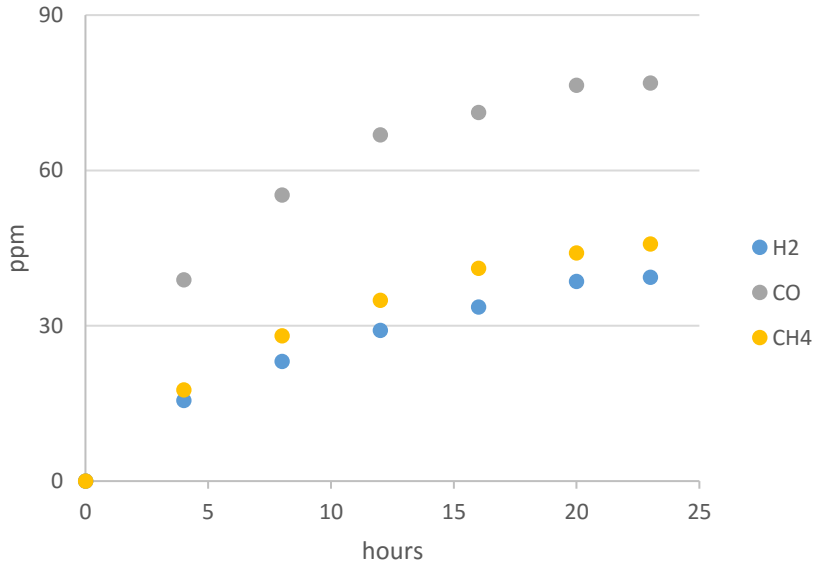

Figure 4-5 CO_2 reduction evolution on thick films. Experimental conditions: P=1.5[bar], I=300 [W/m^2], T=30 [°C], 0%CO_2, 0.6 %H_2O.

4.3.2 Results for thin films

For thin films, no reaction progression could be tracked due to the precision of the GC equipment. Only final conversions could be measured reliably after 24 hours of reaction at 300 [W/m^2]. Those results are summarized in Table 4-1. Although the trajectory of the reaction could not be tracked, it is evident that the selectivity was changed to methane.

Table 4-1. Final production for thin films after 24 hours of 300[W/m^2] illumination.

Product	Final ppm
H_2	18
CO	14
CH_4	23

4.4 Discussion

4.4.1 Light dependency

The exponent β of the Eqn. 3-16 can be estimated using the progression of the main products, which are presented in Figure 4-6. For practical reasons, reaction kinetics and influence of light were analyzed using the thick films results. Comparing the reaction at different light intensities, the curves present the same trend but with a different time-scale. This difference can be modeled with the following relation derived previously

$$\beta_{exp} = \ln(t_{c,2}/t_{c,1})/\ln\left(\frac{I_{2,0}}{I_{1,0}}\right) \quad \text{4-1}$$

The Figure 4-6 presents a consistent increase in all the products when the experiment was performed at identical conditions but increasing the light intensity from 200 [W/m^2] to 300 [W/m^2]. Additionally, the selectivity was roughly preserved in both experiences, suggesting that slightly increasing in illumination does not affect the functionality of the apparent Langmuir expression. Therefore, the β_{exp} value could be quantified by comparing both curves, smoothing the time-scale of the experiment at 200[W/m^2] to minimize the offset between the two curves, which gives a non-dimensional value β_{exp} of approximately 0.47. According to Emeline et al (2005), this is consistent with a photocatalytic reaction limited by recombination (β=0.5).

Compared to the results presented by Pougin et al (2005), our reaction progression presented a notorious selectivity change to H_2 and CO. Considering that our illumination was roughly one order of magnitude smaller, it might be concluded that at significantly larger illumination, not only the time-scale of the experiment is changed but also the selectivity. Additionally, for the thin film the methane selectivity was also higher, suggesting that in the thick film the portion of the material that is significantly less illuminated produced mainly CO and H_2; this disagreement will be more thoroughly discussed in Chapter 6.

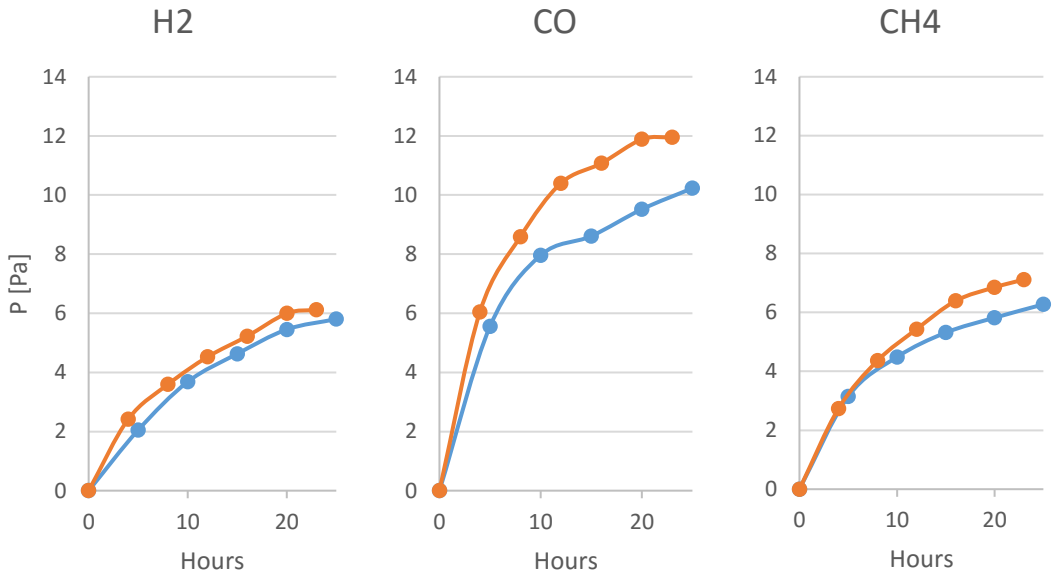

Figure 4-6 Influence of light intensity in CO_2 reduction on thick film at standard conditions. In red, the curve obtained at 300 [W/m^2]; in blue, the curves obtained at 200 [W/m^2].

4.4.2 Key indicators

A comparison of the overall performance is presented in Table 4-2 for our experiment and the reference work of Pougin et al (2016). Although the material was P25 in the four cases, it must be noticed that the nature of the material aggregation was different. However, it is clear that in the thin film case the yield was significantly increased, similar to what it was predicted by Eqn.3-18 for the film thickness. This reinforces the idea that the activity of any material can drastically decrease if the way it is tested does not consider optical features of the reactor. For instance, using the estimations for α_A and α_S at 365[nm], the optical effectiveness was calculated using Eqn. 3-18 as Φ_L =0.67 .This gives a more accurate estimation for the intrinsic activity of P25 for CO_2 photocatalytic reduction considering that in our work the reaction was not fully limited by light.

Table 4-2. Different activities measured for P25 under standard conditions.

Experiment	Catalyst load [mg/cm^2]	Reactor Volume [cm^3]	Incident light intensity [W/m^2]	C-products yield [µmoles g^{-1} h^{-1}]	Φ_L
Thick Film	4.75	100	200	0.28	≈0
Thick Film	4.75	100	300	0.33	≈0
Thin film	0.10	100	300	14.5	67%
Pougin et al	2.5 (powder)	25	2,000	0.48	N/A

4.4.3 Data fitting

The data obtained from thick films follows a typical saturation behavior that is straightforward to model with L-H models used in literature. For instance, the model proposed by Tan et al (2008) was used (Eqn. 4-2), where the HER data was not taken into account, and an initial stoichiometry for a one-step reaction is assumed [41].

$$16CO_{2(ads)} + 15\,H_2O_{(ads)} \xrightarrow{k_{red}} 5H_{2(ads)} + 11CO_{(ads)} + 19O_{2(ads)} + 5CH_{4(g)} \qquad \textbf{4-2}$$

There is still a debate whether hydrogen comes from pure water splitting or a by-product from the degradation of intermediate species coming from CO_2 reduction [65, 63]. Even though our data suggests that HER is independent from CO_2 reduction, we limited the analysis to a one-step reaction, and a backwards oxidation (Eqn.4-3) that limits the CO production. Both, k_{red} and k_{ox} have the same light dependency described in Eqn. 3-2.

$$O_{2(ads)} + 2CO_{(ads)} \xrightarrow{k_{ox}} 2CO_{2(ads)} \qquad \textbf{4-3}$$

The step-by-step procedure to fit the data to the proposed model is presented in the Appendix 8.1. The result of such procedure gives the following fitting:

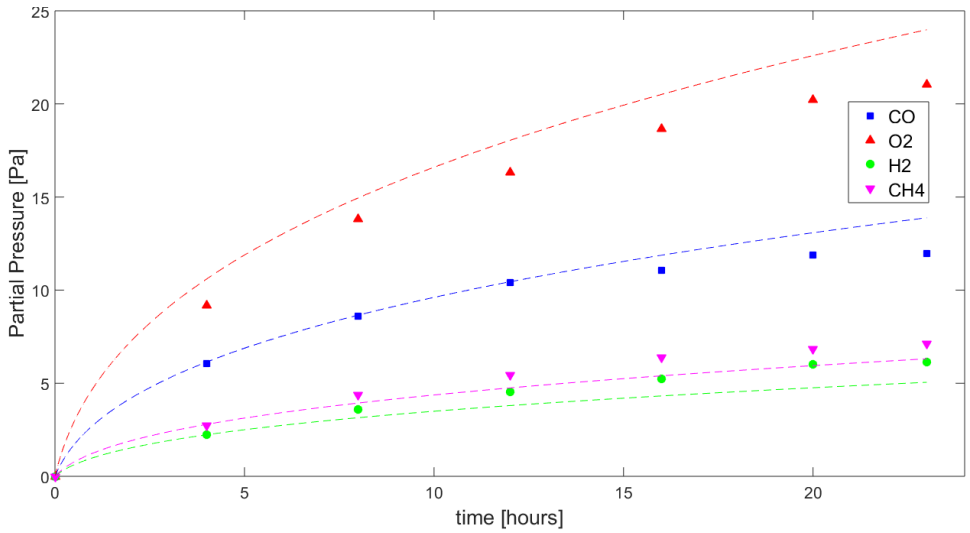

Figure 4-7 Experimental CO_2 reduction vs L-H model prediction. Experimental conditions: P=1.5[bar], I=200 [W/m^2], T=30 [°C], 0%CO_2, 0.6 %H_2O. The dashed lines (--) are the model predictions.

It must be noticed that the model cannot capture some particular behavior of the reaction. In other works, by increasing light up to 1,000[W/m^2] and 2,000[m^2], the reaction selectivity was changed to methane [3, 65]. Therefore, the data fitting just provided is a local representation only and its validity will be discussed more thoroughly in Chapter 6.

4.5 Conclusions

In this chapter, we have shown an experimental setup to reliably test the photocatalytic activity of P25 films under standard conditions (T=25[°C], P=1.5[bar],

1.5% CO_2, 0.6%H_2O). This own-built setup was ensured to avoid any type of contamination and other influences like external carbon sources, depressurization, sampling losses. Additionally, the light source was fully characterized and measured, together with the optical properties of the films at those irradiation conditions.

Among these results we highlight the intended obtained saturation kinetics under standard conditions, replicated from the work of Pougin et al (2015), as well as yields just slightly lower compared to the reference. These differences are easy to explain considering that the catalyst specific area and optical properties of P25 might have changed during the dip-coating process, and most importantly because the light intensity used by our experiment is ten times lower. An important increase of 20 times in the overall carbon products yield was obtained for the thin film, confirming that the influence of light can drastically decrease the intrinsic activity of the material. Using the results from chapter 3, the model showed a similar light dependence compared to recombination limited reactions, and the coarse-grain model for kinetics showed a correct fit of the data. Our estimations show that the optical effectiveness of the film was 67%, suggesting that the intrinsic photocatalytic activity of P25 might be even higher.

Finally, important differences in selectivity compared to the original work were obtained. Other similar experiments suggests that the methane selectivity increases gradually with light intensity, achieving up to 5:1 ratios of CH_4 to CO when illuminated at 2,000 [W/m^2]. This was also confirmed by the results from thin film experiment, which average of light intensity along the film is higher compared to the thick films, or bare powders, which explains partially the slight shift to methane selectivity. Such

difference cannot be explained by the initial coarse-grain model assumptions and will be further discussed in Chapter 6.

CHAPTER 5

MASS TRANSFER ANALYSIS

5.1 Mass transfer in gas phase CO_2 photocatalysis

Since the Honda and Fujushima experiment of, transforming solar energy into chemical compounds appeared as an alternative to directly store solar power in the form of chemical carriers, several experiments and studies have obtained significant improvements in the QY and Product Yield compared to P25. However, reactions rates to date remain slow, which has led to the generalized idea that for gas-solid photocatalytic reactors mass transport limitations are unlikely. Yi ma et al (2014) summarized a registry of different experiments done last decades in vapor phase reactors, which was presented in Table 2-3. As most of the experimental yields are in a range of 0.01-1,000 [μmoles g-catalyst^{-1} h^{-1}], and the diffusivity of the light molecules involved in the reaction (CO, CO_2, H_2O and CH_4) in dilution gases (i.e. Helium) are in the order of $1x10^{-6}$ to $1x10^{-7}$ [m^2/s], it appears to be reasonable to neglect mass transport limitations based on these experiments [12]. Nevertheless, the lack of formal analysis on the governing equations and the use of sophisticated geometries to improve light distribution and yield rates make this assumption less clear.

5.2 Mass transfer influence in observed kinetics

One of the main goals of TiO_2 photocatalysis is the design of large-scale reactor for applications in both CO_2 reduction and water decontamination. This design involves the scale-up of reaction rates from experiments like the one described in former sections, which main assumption is that the bulk concentration of reactants and products is roughly the same as the one in the surface of the catalyst. Otherwise, no matter how accurate the model for surface reaction is, if fitted to the concentrations sampled from the bulk, there will be an inherent bias when predicting reaction rates for large-scale applications.

In CO_2 reduction and water splitting, the influence of mass transfer has been studied more thoroughly in liquid-water reactors, were a diffusion coefficient of CO_2 through a liquid film can be up to $1x10^{-9}$ [m^2 s^{-1}] [66]. Due to the proximity of this diffusion time in a typical reactor geometry with reaction rates, stirring or flow are usually incorporated to make the apparent reduction rates reaction-limited. Velocity field-dependent mass transfer coefficient in liquid films permeated by CO_2 (in form of carbonate) are straightforward to model using correlations based on boundary layer estimations [67]. In this way, many authors have contributed to quantify to what extent mass transfer affects apparent CO_2 reduction rates in liquid water.

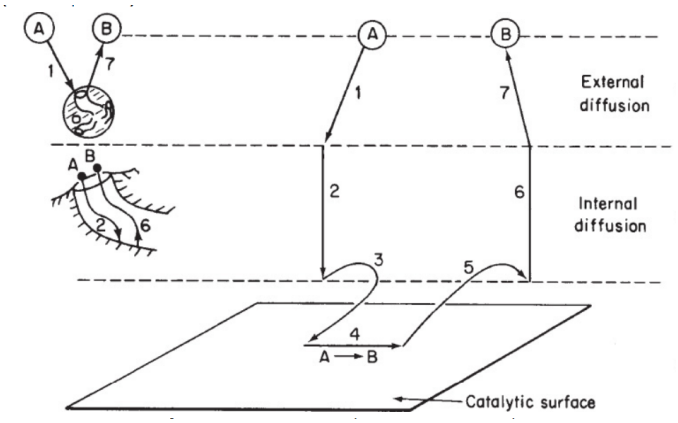

Figure 5-1 Steps in heterogeneous catalysis [Fogler, 2016]. (1) Mass transfer (diffusion) of the reactant(s) from the bulk fluid to the external surface of catalytic meso-structure, (2) Diffusion of the reactant through the pores of the mesostructure, (3) Adsorption of reactants, (4) Reaction on the active surface of the catalyst, (5) Desorption of the products from the active surface (6) Diffusion of the products from the interior of the mesoporous to the external surface (7) Mass transfer of the products from the external meso-structure surface to the bulk fluid.

Although less complicated and apparently less relevant, these concepts has not been studied in reactions involving CO_2 and water in vapor phase. Typical batch reactors using water vapors have a stagnant vapor phase which is assumed to be completely mixed; given the typical reactor dimension this assumption may be true. However, its more rigorous quantification is key to determine to what extent it is valid. This is recently becoming more necessary for experiments testing photocatalytic activity of materials that have fairly surpassed P25. In such photo-active materials, the reaction-limited assumption is less clear when high illumination and large geometries are used.

5.3 Internal Mass transfer

In Figure 5-1 it is presented a sketch of the different transport phenomena involved in heterogeneous catalysis [68]. We will address internal diffusion first to show

that the CO_2 conversion through the photo-active film is less limiting than external diffusion.

The particular phenomena that describes internal mass transfer in a porous film are Knudsen Diffusion and Molecular Diffusion through idealized nano-pores. Knudsen Diffusion takes over regular diffusion when the diffusivity of the gas is dominated by the collisions with the wall of a small channel [69]. This occurs when the Mean Free Path of the molecule exceeds the length of the channel, which is quantified by the ratio of the mean free path of the molecules in the gas mixture, λ, and the approximate channel width d_p. This ratio is the Knudsen Number (K_n) and indicates pure Knudsen diffusion when K_n>10. The Mean Free Path of an ideal gas with an atomic diameter assumed to be the characteristic CO2 D_{CO2} (2.32×10^{-10} [m]) can be calculated using Eqn. 5-1 and Eqn. 5-2.

$$\lambda = \frac{1}{\sqrt{2} \times n \times \pi \times {D_{CO2}}^2} \quad \textbf{5-1}$$

$$n = \frac{P}{RT} \quad \textbf{5-2}$$

Where

P : Reactants Pressure (140,000 [Pa])

R : 8.314 [kJ/kmol°K]

T : Experiment temperature (303 [°K])

The mean free path at these conditions is 113 [nm]. On the other hand, the pore radius R_p is estimated by assuming an ideal packing of nanoparticles on the film is 35[nm] (Appendix 8.2), giving a K_n of 1.67. Therefore, internal mass transfer is slightly dominated by Knudsen Diffusion, and an estimation of its magnitude can be calculated using Eqn. 5-3, where m_{CO2} is CO_2 molecular weight and k_B is the Boltzmann constant.

$$D_{K,CO2} = \frac{2R_p}{3} \times \left(\frac{8K_BT}{\pi m_{CO_2}}\right)^{1/2} \quad \textbf{5-3}$$

However, the question of how dominant is the internal mass transfer resistance compared to pure surface reaction in a typical P25 dip-coated glass remains unanswered. Using the dimensional analysis in Appendix 8.2 we can quantify its influence. For practical reasons, we only compared internal diffusion to external diffusion. The comparison between them is presented in Appendix 8.2 and demonstrates that internal mass transfer in this system is less limiting than external diffusion.

5.4 External Mass transfer

External diffusion is the process by which reactants are driven from the bulk of the gas phase to the surface of the catalyst, where the reaction occurs as an effective surface reaction rate. This process depends on the diffusion properties of the different species involved in the dilution gas, and depending on the characteristic time for this process, it might have a great impact on the observed reaction rates.

In the gas phase reactor presented in Chapter 3, the diffusion of reactants will be driven by the photocatalytic reaction rate occurring at the bottom of the reactor. Even when significantly slower compared to the diffusion time of the external diffusion in

regular catalysts, the gradient formed must be quantified based on non-dimensional numbers to extract its actual influence on observed reaction rates. Additionally, it must be noticed that the diffusion time of external mass transfer is approximately five orders of magnitude higher than the effective Diffusion time in pores (Appendix 8.2), which reflects immediately that external diffusion is much more limiting. This implies that the reaction constant k_{red} at the bottom of the reactor corresponds to the apparent L-H parameter described in Chapter 3, and that all the internal area is equally exposed to the concentration of reactants near the external surface of the film

5.5 Modeling Diffusion and Heterogeneous reaction in a Batch Photocatalytic reactor

5.5.1 Scaling and dimensions

The reactor geometry and basic scaling concepts were already presented in Chapter 3. Before to start any attempt to solve such problem considering mass transfer limitations, it is useful to use non-dimensional normalized variables by using convenient characteristic times, lengths and concentrations. The most basic scaling we started with is similar to the one in Chapter 3 and is presented in Eqn. 5-4 to Eqn. 5-7 (i=1:CO_2, 2:H_2O, 3:CO, 4:O_2, 5:H_2, 6:CH_4).

$$\left(\frac{L^2}{\beta_i D_1 t_c}\right)\frac{\partial \tilde{c}_i}{\partial \tau} = \frac{\partial^2 \tilde{c}_i}{\partial \tilde{z}^2} \qquad \textbf{5-4}$$

$$\left.\frac{\partial \tilde{c}_i}{\partial \tilde{z}}\right|_{(\tilde{z}=1)} = \left(\frac{\gamma_i a L}{\beta_i D_1 \lambda_i c_c}\right) J_{net}(\tilde{c}_1, \tilde{c}_2 \dots \tilde{c}_n) \qquad \textbf{5-5}$$

$$\left.\frac{\partial \tilde{c}_i}{\partial \tilde{z}}\right|_{(\tilde{z}=0)} = 0 \qquad \textbf{5-6}$$

$$\tilde{c}_i(\tilde{z}, \tau = 0) = 1 \qquad \textbf{5-7}$$

Where

L : Reactor Height (8[cm])

D_1 : CO_2 diffusion in N_2 ($2x10^{-5}$ [m^2 s^{-1}])

β_i : Relative diffusion of the species *i* to CO_2

J_{net} : Surface heterogeneous reaction (L-H expression)

γ_i : Stoichiometry of species *i*

t_c : Characteristic time

c_c : Characteristic concentration

λ_i : Ratio of the characteristic concentration of species *i* and c_c

Additionally, the time-scale of interest is the one that represents the fastest moment for the reaction, but representative of the experiments as well. We define this characteristic time as the maximum concentration of product (CO) obtained divided by the initial formation rates. This slightly contravene the initial condition, because in a diffusion time scale, a small gradient is previously formed. This first stage for the reaction because it only represents few seconds, and the error introduced by assuming the initial profile for the longer time-scale is very small. If the diffusion time represents

an important portion of the experiment time, and as long as the problem is not reaction limited, its rigorous demonstration will just require matching both solutions.

We also ignored the other two characteristic times candidates, which are the depletion of reactants and the saturation time. The depletion of reactants will stop at the saturation time first; and this second one represents the slowest moment for the reduction of CO_2 and thus reaction-limited. Using the production time-scale as the characteristic time, the non-dimensionalized equations give us our first math object to analyze in Eqn. 5-8 to Eqn. 5-12.

$$\left(\frac{J_{net,0}aL}{\beta_i D_1 c_c}\right)\frac{\partial \tilde{c}_i}{\partial \tau} = \frac{\partial^2 \tilde{c}_i}{\partial \tilde{z}^2} \quad \textbf{5-8}$$

$$\varepsilon\frac{\partial \tilde{c}_i}{\partial \tau} = \beta_i\frac{\partial^2 \tilde{c}_i}{\partial \tilde{z}^2} \quad \textbf{5-9}$$

$$\left.\frac{\partial \tilde{c}_i}{\partial \tilde{z}}\right|_{(\tilde{z}=1)} = \left(a\frac{\gamma_i L k_{red}}{\beta_i D_1 \lambda_i c_c}\right)\tilde{J}_{net}(\tilde{c}_1, \tilde{c}_2 \dots \tilde{c}_n) \quad \textbf{5-10}$$

$$\left.\frac{\partial \tilde{c}_i}{\partial \tilde{z}}\right|_{(\tilde{z}=0)} = 0 \quad \textbf{5-11}$$

$$\tilde{c}_i(\tilde{z}, \tau = 0) = 1 \quad \textbf{5-12}$$

Additionally, the surface reaction functionality is given by the Langmuir-Hinshelwood expression calculated in Chapter 4 and put into concentration terms in Eqn. 5-13.

$$\tilde{J}_{net} = \left(\frac{\tilde{c}_{1,s}{}^{\sigma_1} \tilde{c}_{2,s}{}^{\sigma_2}}{\left(1 + \alpha_1 \tilde{c}_{1,s} + \alpha_2 \tilde{c}_{2,s} + \ldots\right)^{\sigma_1 + \sigma_2}} - K_{ox} \gamma'_i \frac{\tilde{c}_{3,s}{}^{|\sigma'_3|} \tilde{c}_{4,s}{}^{|\sigma'_4|}}{\left(1 + \alpha_1 \tilde{c}_{1,s} + \alpha_2 \tilde{c}_{2,s} + \ldots\right)^{|\sigma'_3| + |\sigma'_4|}} \right) \quad \text{5-13}$$

Where:

K'_i : Langmuir adsorption constant of species *i* adapted to concentrations

K_{ox} : k_{red} and k_{ox} ratio

γ'_i : ratio of stoichiometry in reduction and oxidation of species *i*

σ_i : Exponent in L-H expression of species *i*

Regardless of its generality, the problem is still non-linear and dependent-variable-coupled. Its resolution using regular methods would involve finite elements or finite differences calculations with two independent variables [37, 47]. These type of calculations are computationally expensive and restricted to the each particular geometry, which makes its application to decoupling mass transfer from observed kinetics impracticable [37].

5.5.2 Regular Perturbation

When there is such a difference between 2 characteristic times or length scales, the solution can be approximated to an asymptotic series in terms of a small parameter [70, 71]. In the conservation equation, the small parameter ε will be given by the ratio of the diffusion time and reaction time (Eqn.5-14 and Eqn.5-15). Typically in more

conventional kinetics, such as first or second order rates, this terms correspond to the Damkohler number.

$$t_{dif} = \frac{L^2}{D_{CO_2}} \quad \textbf{5-14}$$

$$t_{rxn} = \frac{c_c V_R}{r_{red} A_R} \quad \textbf{5-15}$$

The main advantage of using this method is that the outcome of the analysis is an analytical expression, which is of enormous value for its validity under different parameters and geometries. This analytical expression take less than seconds in an optimization routine and can be calculated based on non-dimensional numbers only [72]. Additionally, in this application to intrinsic photocatalytic activity, it only requires an observed production rate to roughly estimate the characteristic reaction time for the problem. Based on our reactor geometries and measured kinetics, the characteristic reaction time is approximately 3 hours, while the diffusion time is approximately 3 minutes.

Although the comparison between the two characteristic times comes naturally and defines immediately what the limiting phenomena is, it does not provide quantification neither a threshold for the comparison under different conditions, i.e. when both diffusion and reaction time are comparable. In contrast, finding a perturbation solution is not trivial and requires thorough understanding and definition of the math object. In some cases, the problem will give place to a boundary layer (singular problem), which require asymptotic matching procedures [72, 73].

In our experiment for P25, it is quite evident that the influence of mass transfer is small. Nevertheless, some materials in literature can have up to 1000 time faster reaction rates. Our aim is to provide a general solution for this problem that can be consulted as a rapid estimation for the difference of concentration in bulk and in the surface of the catalyst. This difference will be crucial to fit the actual surface concentration to models, and its analytical representation will be valid as long as the small perturbation parameter does not exceed 1, which covers a wide range of experiments.

5.5.3 Decoupling the system and linearizing

The first step previous to try a perturbation expansion is to linearize the Langmuir-Hinshelwood expression. Using a Taylor expansion around the initial surface concentrations $c_{i,o}$ (i means reactants, j means products) the reaction term is reduced to Eqn. 5-16.

$$\tilde{J}\left(\tilde{c}_{r1}, \tilde{c}_{r2}, \dots \tilde{c}_i \dots \tilde{c}_n : \tilde{c}_{p1}, \tilde{c}_{2p}, \dots \tilde{c}_j \dots \tilde{c}_m\right) = \tilde{J}\left(\tilde{\boldsymbol{c}}_{\boldsymbol{i,0}} : \tilde{\boldsymbol{c}}_{\boldsymbol{j,0}}\right) + \sum_{n=1}^{\infty} \sum \left.\frac{d^n \tilde{J}}{d\tilde{c}_i{}^n}\right|_{(\tilde{\boldsymbol{c}}_{i,0})} \times \frac{\left(\tilde{c}_{i,s} - \tilde{c}_{i,0}\right)^n}{n!} \qquad \textbf{5-16}$$

We kept only the reduction part since in our problem the backwards reaction only has important effects at extremely long time scales ($k_{ox} \approx 1\text{x}10^{-26}$ [moles m^{-2} s^{-1}]). In this particular case, we only worked with the saturation contribution of the products. However, it must be noticed that given the form of the Langmuir problem, in other cases where the backwards oxidation is strong the typical asymptotic part of the reaction is

lost by using initial concentration of products equal to zero. By dropping the backwards term the reaction functionality is simplified to Eqn. 5-17.

$$\tilde{J}(\tilde{c}_1, \tilde{c}_2 \dots \tilde{c}_n) = \tilde{J}_0 + \left(-\frac{(\sigma_1+\sigma_2)K'_1}{\left(1+\sum K'_i c_{i,0}\right)} + \frac{\sigma_1}{c_{i,0}}\right)(c_1 - c_{1,0}) + \left(-\frac{(\sigma_1+\sigma_2)K'_2}{\left(1+\sum K'_i c_{i,0}\right)} + \frac{\sigma_2}{c_{2,0}}\right)(c_2 - c_{2,0}) - \sum \frac{(\sigma_1+\sigma_2)K'_j}{\left(1+\sum K'_i c_{i,0}\right)}(c_j - c_{j,0}) + O(c^2) \quad \textbf{5-17}$$

Although linear up to the second term, the conservation equations for each product are still coupled in this boundary condition. However, it will be demonstrated that using a new scaling and replacing the perturbation expansion, the *O(1)* solution will be fully decoupled, and the rest of the subsequent problems of Order δ ($O[\delta]$) can be extracted after obtaining previous solutions. The scaling for the boundary conditions now yields Eqn.5-18 to Eqn.5-20.

$$\left.\frac{\partial \tilde{c}_i}{\partial \tilde{z}}\right|_{(\tilde{z}=1)} = \varepsilon\left(\frac{\gamma_i}{\beta_i \lambda_i}\right) \times \tilde{f}(\tilde{c}_1, \tilde{c}_2 \dots \tilde{c}_n) \quad \textbf{5-18}$$

$$\tilde{c}_{i,s} = \tilde{c}_i|_{(\tilde{z}=1)} \quad \textbf{5-19}$$

$$\tilde{f}(\tilde{c}_1, \tilde{c}_2 \dots \tilde{c}_n) = 1 + \left(\frac{\sigma_1}{c_{1,0}} - \frac{(\sigma_1+\sigma_2)K'_1}{\left(1+\sum K'_i c_{i,0}\right)}\right)\lambda_1 c_c \tilde{c}_{1,s} + \left(\frac{\sigma_2}{c_{2,0}} - \frac{(\sigma_1+\sigma_2)K'_2}{\left(1+\sum K'_i c_{i,0}\right)}\right)\lambda_2 c_c \tilde{c}_{2,s} - \sum \frac{(\sigma_1+\sigma_2)K'_j}{\left(1+\sum K'_i c_{i,0}\right)}\lambda_j c_c \tilde{c}_{j,s} \quad \textbf{5-20}$$

5.5.4 Re-scaling

As previously mentioned, some problems require a special scaling for a consistent solutions to appear. In this case, if the following perturbation solution expansion is tried (upper indices are not exponents).

$$\tilde{c}_i = \tilde{c}_i^0 + \varepsilon\tilde{c}_i^1 + \varepsilon^2\tilde{c}_i^2 \quad \textbf{5-21}$$

The time derivative is lost and thus the *O*(1) problem cannot be solved explicitly for time. If a higher order derivative term is lost, it would lead to a singular problem due to the inability for the solution to meet two boundary conditions (B.C.) at the same time [70]. In Eqn.5-9, keeping the time derivative to obtain a solution for longer times is still a regular perturbation problem, but it needs a special scaling for the solution to have explicit time terms that can meet the initial condition. In order to keep the time derivative, it was re-defined in Eqn. 5-22 to Eqn. 5-25 the axis coordinate using a function *g(ε)* a power of the ε term.

$$Y = \frac{1-\tilde{z}}{g(\varepsilon)} \quad \textbf{5-22}$$

$$g(\varepsilon) = \varepsilon^{-1/2} \quad \textbf{5-23}$$

$$\left.\frac{\partial\tilde{c}_i}{\partial Y}\right|_{(Y=0)} = \sqrt{\varepsilon}\left(\frac{\gamma_i}{\beta_i\lambda_i}\right)\tilde{f}(\tilde{c}_1, \tilde{c}_2 \ldots \tilde{c}_n) \quad \textbf{5-24}$$

$$\left.\frac{\partial\tilde{c}_i}{\partial Y}\right|_{(Y=\varepsilon^{-1/2})} = 0 \quad \textbf{5-25}$$

In this case we still have the problem that no explicit time terms appear for the *O*(1) solution. Trying the re-scaling in Eqn.5-26 to Eqn.5-28 of the concentrations of products (*i*) and reactants (*j*), an implicit function of the solution to the small parameter is obtained.

$$c_i = \lambda_i c_c \left(1 - \gamma_i \frac{\hat{c}_i}{h(\varepsilon)(\sigma_1 + \sigma_2)\beta_i}\right) \quad \textbf{5-26}$$

$$c_j = \gamma_j \lambda_j c_c \left(\frac{\hat{c}_j}{h(\varepsilon)(\sigma_1 + \sigma_2)\beta_j}\right) \quad \textbf{5-27}$$

$$h(\varepsilon) = \varepsilon^{-1/2} \quad \textbf{5-28}$$

Finally, redefine the problem with the small ε term in a boundary condition and keeping all the time and space derivatives, the final set of non-dimensional expressions is obtained and presented in Eqn.5-29 to Eqn.5-32.

$$\frac{\partial \hat{c}_i}{\partial \tau} = \beta_i \frac{\partial^2 \hat{c}_i}{\partial Y^2} \quad \textbf{5-29}$$

$$\left.\frac{\partial \hat{c}_i}{\partial Y}\right|_{(Y=0)} = A_i \left[1 + \sqrt{\varepsilon}\frac{\gamma_1}{\beta_1}\left(\frac{\sigma_1}{(\sigma_1 + \sigma_2)} - \theta_{1,0}\right)\hat{c}_1 + \sqrt{\varepsilon}\frac{\gamma_2}{\beta_2}\left(\frac{\sigma_2}{(\sigma_1 + \sigma_2)} - \theta_{2,0}\right) - \sqrt{\varepsilon}\sum \frac{K'_j \lambda_j c_c}{\left(1 + \sum K'_i c_{i,0}\right)(\sigma_1 + \sigma_2)}\frac{\gamma_j}{\beta_j}\hat{c}_j\right] \quad \textbf{5-30}$$

$$\left.\frac{\partial \tilde{c}_i}{\partial Y}\right|_{\left(Y=\varepsilon^{-1/2}\right)} = 0 \quad \textbf{5-31}$$

$$A_i = \frac{(\sigma_1 + \sigma_2)}{\lambda_i} \quad \textbf{5-32}$$

Now finally make the following expansion in terms of $\delta=\varepsilon^{1/2}$

$$\hat{c}_i = \hat{c}_i^0 + \delta\hat{c}_i^1 + \delta^2\hat{c}_i^2 \qquad \textbf{5-33}$$

This expression leads to a classical PDE with finite domains for the $O(1)$ problem. By doing this, we have changed a non-linear problem to a linear decoupled set of solutions that will be solved sequentially by using Finite Fourier Transform (Eqn.5-34 to Eqn. 5-36). Using an appropriate basis function in the FFT method, the solution should not include any term blowing up.

$$\frac{\partial\hat{c}_i^0}{\partial\tau} = \beta_i\frac{\partial^2\hat{c}_i^0}{\partial Y^2} \qquad \textbf{5-34}$$

$$\left.\frac{\partial\hat{c}_i^0}{\partial Y}\right|_{(Y=0)} = A_i^1 \qquad \textbf{5-35}$$

$$\left.\frac{\partial\hat{c}_i^0}{\partial Y}\right|_{\left(Y=\varepsilon^{-1/2}\right)} = 0 \qquad \textbf{5-36}$$

5.5.5 Finite Fourier Transform

The step by step procedure to solve the previous problem is described in Appendix 8.3. Using the following basis functions

$$\hat{c}_i^0 = \hat{c}_i^0(\tau)\Phi_{i,n}^0(Y) \qquad \textbf{5-37}$$

$$\Phi_{i,n}^{0}(Y) = \sqrt{\frac{2}{\sqrt{\varepsilon}}}\cos\left(n\pi Y/\sqrt{\varepsilon}\right) \quad \textbf{5-38}$$

$$\Phi_{i,0}^{0}(Y) = \sqrt{\frac{1}{\sqrt{\varepsilon}}} \quad \textbf{5-39}$$

The overall solution obtained for reactants (c_i) and products (c_j)

$$c_i = \lambda_i c_c \left(1 - \sqrt{2}\frac{\gamma_i}{\lambda_i\beta_i}\tau - \gamma_i \frac{\sqrt{2}\varepsilon^{5/4}\sum_{n=1}^{\infty}\frac{\cos\left(\pi n(1-\tilde{z})\right)}{(n\pi)^2}\left(1-\exp\left(-\frac{\sqrt{2}(n\pi)^2}{\varepsilon^{5/4}}\tau\right)\right)}{\lambda_i\beta_i}\right) \quad \textbf{5-40}$$

$$c_j = \lambda_i c_c \sqrt{2}\frac{\gamma_j}{\lambda_j\beta_j}\left(\tau + \varepsilon^{5/4}\sum_{n=1}^{\infty}\frac{\cos\left(\pi n(1-\tilde{z})\right)}{(n\pi)^2}\left(1-\exp\left(-\frac{\sqrt{2}(n\pi)^2}{\varepsilon^{5/4}}\tau\right)\right)\right) \quad \textbf{5-41}$$

For the higher order terms the solution will follow exactly the same procedure, with the only difference that replacing the previous solution to the subsequent problem will lead to non-homogeneous solutions. By using linear superposition the problem will have a similar solution with a particular and homogeneous time dependent terms, with increasing complexity but solvable. If the sampling point is near the top of the reactor (z=0), the $O(1)$ expression to calculate the difference between the measured and the surface concentration (for products and reactants) is the following

$$\Delta c_j = c_c 2\sqrt{2}\frac{\gamma_j}{\beta_j}\left(\varepsilon^{5/4}\sum_{n=1}^{\infty}\frac{1}{(2n\pi)^2}\left(1-\exp\left(-\frac{(8n\pi)^2}{\varepsilon^{5/4}}\tau\right)\right)\right) \quad \textbf{5-42}$$

5.5.6 Discussion

The result in Eqn. 5-42 demonstrate that the profile is almost flat in time for small values of ε. As ε in our experiments is estimated as $\approx 10^{-2}$, the rapid collapse of the exponential term at the characteristic time of the reaction makes the correction small and stationary. This demonstrates that under the standard experimental conditions, the CO_2 reduction in P25 is not limited by external diffusion. More generally, this result applies to any other material and/or conditions that can be approximated to a Langmuir-Like expression.

If the small parameter ε approaches to 1, the correction will increase and more terms may be included in the expansion. In this way, a convenient form to include this correction in such cases will be including Eqn.5-42 in the surface concentration when fitting reaction parameters in the procedure presented in Appendix 8.1. Moreover, in any other experiment, the initial reaction rate can be estimated immediately without any fitting procedure by estimating the slope at the beginning of the reaction progress. By calculating the diffusion time with the reaction time defined in this section, the parameter ε can be roughly estimated. If similar to our case for P25, where ε is approximately 0.01, the reactor can just be considered reaction limited and therefore an ideal batch reactor.

5.6 Conclusions

In consideration of the results of this section, we can neglect the influence of mass transfer limitation in observed reaction rates in this work. The dimensional analysis performed in this section evidenced a big difference between the diffusion time of reactants in Nitrogen, and the reaction time. This difference was a first indication that

the reaction was not limited by diffusion, however, a perturbation analysis was used to solve such system using regular linear PDE methods (Fourier Finite Transform). This resolution yielded an analytical expression convenient for the purposes of intrinsic kinetics, since this type of correction based on non-dimensional numbers, for instance a Damkohler number for an L-H expression, are computationally cheap and easy to incorporate in the reaction parameters fitting routine in Appendix 8.1. Additionally, this expression can be used by other similar works where the observed reaction can be up to 1,000 times faster. In those cases, as long as the parameter ε remains smaller than 1, the solution is still valid and more terms should be considered in the correction, which makes this solutions an important contribution to the field.

Finally, an important remark is that some other parameters affecting the parameter ε can be plugged into its definition, predicting under what conditions the reaction-limited assumption is still valid ($\varepsilon<1$), including incident light intensity, catalyst surface loading, reactor height, and reactants partial pressures.

CHAPTER 6

SURFACE REACTION MODELS

6.1 Summary of intrinsic kinetics

In previous chapters the different external factors affecting the observed CO_2 photocatalytic reduction activity of P25 were characterized and controlled. On one hand, a practical experimental setup was built to avoid the dependency of light intensity to the axial coordinate of the reactor chamber. The reactor chamber was initially purged, and connected to a GC equipment in a closed loop at positive pressure prior to illumination. This ensured that the samples obtained from the batch only contained initial reactants, and products coming from the photocatalytic reaction occurring at the surface of the P25 thin film placed at the bottom of the reactor. These photocatalytically active films thicknesses were two convenient limiting cases to characterize the intrinsic activity of P25 under standard conditions.

On the other hand, generally accepted coarse grain models for photocatalysis were used to approximate the reaction curve locally to 7 apparent L-H kinetics and the light intensity influence. These coarse grain approximations were finally analyzed using an asymptotic perturbation expansion to disentangle the external diffusion influence.

6.2 Expanding reaction model predictability

Once the intrinsic activity of P25 has been outlined, the final part of this work is the construction of a more realistic model for surface reaction that in principle could

explain multiple independent data sets. This ability of the model to explain the reaction behavior at different conditions was also pointed out as a “golden rule” for any kinetic model by Emeline et al (2005); more independent experiments at different CO_2 and H_2O molar fractions, total pressure, and illumination would finally demonstrate the robustness of the fitted reaction model. However, as coarse grain models presents enormous limitations well described in Chapter 3, it is necessary to build a better representation that applies also in wider range of experimental conditions.

For instance, the results presented in Chapter 4 are a clear evidence that the original coarse-grain model used is not able to predict the methane selectivity increase with drastic increase of light intensity, neither the formation of key intermediates that barely desorb from the surface, such as HCOOH, CH_3OH, and COOH [3, 52]. In this way, as there is experimental evidence of light intensity influence in selectivity of products, we limited the analysis to the variation of light. Nevertheless, other validations may include change in reactants concentration and or system temperature.

This section aims to relate charge-carrier generation and diffusion; electron-transfer rates; and gas-solid adsorption to predict reaction rates of more physical sense that can describe a trend when a strong fluctuation of light intensity is introduced; the light intensity was associated to the incident light intensity. The full mathematical representation of the photocatalytic process was obtained and solved in 3 different time-scales. The resolution procedure involved the integration of non-linear dynamical systems, ODE solvers, and optimizers to finally obtain a set of reduced parameters which accuracy was tested qualitatively as a proof of concept.

6.3 Photocatalytic reaction modeling at different time-scales

6.3.1 Free charges generation and fate

As described in Chapter 2, the driving force for the generation of free carriers is the excitation (and fast thermalization) of charges. This process is extremely fast and key to describe the profile of free-charges in the material that will be able to diffuse and react with photoactive molecules [8]. Therefore, it is clear that a convenient way to link the influence of light with reaction rates is to start looking for a steady solution for the movement of charges, to then plug this solution into other slower processes expressions.

From a mathematical perspective, and similar to the work of Liu et al (2013), it was assumed that this process occurs in a time-scale of femto seconds together with the thermalization of electrons and holes to the bottom of the conduction and top of the valence band respectively. Once the electron-hole pairs have been created in the bulk of the nanocrystal, their movement will follow a minority charge-carrier diffusion process. This is a good approximation for P25 which is known to be an n-type semiconductor [74]. The following equation slightly differs from the original one since the continuity in radial coordinates is introduced.

$$\frac{1}{r^2}\frac{\partial}{\partial r}\left(r^2\frac{J_h}{e}\right) - k_r c_h + G = \frac{\partial c_h}{\partial t} \qquad \textbf{6-1}$$

Where

c_h : bulk concentration of holes in the valence band [m^{-2}]

r : radial coordinate ($\approx 10^{-8}$ [m])

J_h : current density of holes

e : absolute charge of electrons

k_r : first order recombination/life-time term [s^{-1}]

D_h : diffusion of free holes [$m^2\ s^{-1}$]

G : generation of holes [$m^{-3}\ s^{-1}$]

Using the same argument as Liu et al (2013), the drift part was neglected since the Debye length is much larger than the typical dimension of a nanoparticle [9]. Then, the original equation simplifies to Eqn. 6-2.

$$D_h \frac{1}{r^2}\frac{\partial}{\partial r}\left(r^2 \frac{\partial c_h}{\partial r}\right) - k_r c_h + G = \frac{\partial c_h}{\partial t} \quad \textbf{6-2}$$

Additionally, the generation term can be obtained by using Beer-Lambert's law neglecting the variation in the radial and solid angle (θ and φ in Eqn.6-3 to Eqn.6-5).

$$I = I_0 \exp(-\alpha z) \quad \textbf{6-3}$$

$$G \approx \alpha \Phi \quad \textbf{6-4}$$

$$\Phi = \frac{I_0}{E_{ph}} \quad \textbf{6-5}$$

Where

I_0 : Incident light intensity in [$J\ s^{-1}\ m^{-2}$]

α : Optical depth in [m^{-1}]

E_{ph} : Energy of a photon at the source wavelength. 5.22×10^{-19} [J] for a λ=380 [nm] light source.

D_h : Diffusion of holes. Estimated as 10^{-7} [m^{-2} s^{-1}] [10].

Φ : Photon Flux in [m^{-2} s^{-1}]

Putting everything into non-dimensional terms (Eqn.6-6 to Eqn.6-9) yields a non-dimensional set of equations (Eqn.6-10 to Eqn.6-12) for the motion of free charges.

$$\tilde{r} = r/r_p \quad \textbf{6-6}$$

$$\tau = t/t_c \quad \textbf{6-7}$$

$$\tilde{c}_h = c_h/c_{h,c} \quad \textbf{6-8}$$

$$c_{h,c} = \frac{\alpha\Phi}{D_h/{r_p}^2} \quad \textbf{6-9}$$

$$\frac{1}{\tilde{r}^2}\frac{\partial}{\partial\tilde{r}}\left(\tilde{r}^2\frac{\partial\tilde{c}_h}{\partial\tilde{r}}\right) - \varepsilon_1\tilde{c}_h + 1 = \varepsilon_2\frac{\partial\tilde{c}_h}{\partial\tau} \quad \textbf{6-10}$$

$$\varepsilon_1 = \frac{k_r}{D_h/{r_p}^2} \approx 1 \times 10^{-19} \quad \textbf{6-11}$$

$$\varepsilon_2 = \frac{1/t_c}{D_h/{r_p}^2} \quad \textbf{6-12}$$

It is also justified that under low illumination conditions the thermal equilibrium concentration of electrons is almost unaffected. The characteristic hole concentration (c_{hc}) is in the order of 10^{17} [m^{-3}], while electron concentration under thermal equilibrium is in a range between 10^{17} and 10^{21} [m^{-3}] [74]. For instance the epsilon term ε_1 was neglected, yet it can and incorporated afterwards to the solution using a regular perturbation analysis. Additionally, the ε_2 term will be very small if a solution of this equation is attempted in a long time scale compared to the diffusion time of holes (10^{-11} [s]). Since the solution is in the time-scale of electron–transfer processes (10^{-8} [s] to 10^{-4} [s]), the PDE can be considered stationary leading to the set of Eqn.6-13 to Eqn.6-15. The boundary conditions are based on conservation principles.

$$D_h \frac{\partial \tilde{c}_h}{\partial \tilde{r}}\Big|_{\tilde{r}=1} = \left(r_p / c_{h,c}\right) \times C_T R_c\left(\boldsymbol{\theta_i}, c_{h,s}\right) \quad \textbf{6-13}$$

$$\frac{\partial \tilde{c}_h}{\partial \tilde{r}}\Big|_{\tilde{r}=0} = 0 \quad \textbf{6-14}$$

$$\tilde{c}_{h,s} = \tilde{c}_h(\tilde{r} = 1) \quad \textbf{6-15}$$

Where

R_c: Parametrized consumption rate of holes in surface [s^{-1}]. Function of coverages of the different active and non-active species ($\boldsymbol{\theta}_i$), and the bulk concentration of holes near the surface ($c_{h,s}$)

C_T: Concentration of active sites in surface. Estimated as 5.22×10^{22} [m^{-2}] [75]

The solution becomes a simple set of algebraic equations dependent on the surface events like recombination and activation of molecules (Eqn.6-16 to Eqn. 6-18). The parameter *B* can be calculated using surface coverages fixed (static).

$$\tilde{c}_h = \frac{\tilde{r}}{6} + B \qquad \textbf{6-16}$$

$$\tilde{c}_{h,s} = \frac{1}{6} + B \qquad \textbf{6-17}$$

$$\left.\frac{\partial \tilde{c}_h}{\partial \tilde{r}}\right|_{\tilde{r}=1} = \frac{1}{6} \qquad \textbf{6-18}$$

6.3.2 Electron-transfer and adsorption/desorption time-scale

As pointed out in Chapter 2, an essential part of the overall CO_2 reduction process is the activation of species under redox phenomena principles. It was be assumed for instance that monoatomic H and O were the key precursor that produce further reaction according to the work of He et al (2010) [52]. Those activation events on surfaces have a characteristic time in the range of hundreds of nano-second. For this reason, these events are comparable to gas-solid adsorption-desorption processes [57].

Very often in literature, both processes are decoupled by considering redox steps instantaneous and fixing the coverage of the precursor species adsorbates (infinitely slow or in steady state) [7, 9, 56]. Although it is true that in vapor phase adsorption is a condition for subsequent activation, the coverage of species is also dynamic at this time-scale. According to experimental and theoretical literature in physorption of gases on

TiO_2 anatase (101), the adsorption can be represented as it follows [75, 76]. For the species adsorbing in Ti^{+4} coordinated surface sites (*)

$$H_2O_{(g)} + * \xrightarrow{k_{H_2O,ads}} H_2O_{(a)} \quad \textbf{6-19}$$

$$H_2O_{(a)} \xrightarrow{k_{H_2O,des}} H_2O_{(a)} + * \quad \textbf{6-20}$$

And same for all the rest of carbon species. For hydrogen species that adsorbs in $O^{-2}_{(br)}$ sites (■)

$$H_{2(g)} + \blacksquare \xrightarrow{k_{H_2,ads}} H_{2(a)} \quad \textbf{6-21}$$

After adsorption, the activation events will be the hole-attack to adsorbed water and subsequent oxidation of hydroxyl radicals. It must be noticed that other slow redox processes were not considered in this time-scale, and bulk holes were considered to be reactive enough to trigger activation without being trapped, which is not the case for electrons. Finally, it was assumed that monoatomic hydrogen and oxygen radical are the only species capable of trigger other slower reactions. Its formation and recombination was considered fast (according to some literature, from 10[μs] to 1[ms]), but its utilization will be part of the slow surface reaction model [9, 56, 57]. A simple mechanism for water splitting and activation of protons and monoatomic oxygen is presented below (h_s is a free surface hole and F a trapped surface electron) [77]

$$H_2O_{(g)} + h_s \xrightarrow{k_{H_2O,act}} OH^{\cdot}{}_{(a)} + H^{+}{}_{(\blacksquare)} \quad \textbf{6-22}$$

$$OH^{\cdot}{}_{(a)} + h_s \xrightarrow{k_{OH,act}} O_{(a)} + H^+{}_{(\blacksquare)} \quad \textbf{6-23}$$

$$O_{(a)} + F \xrightarrow{k_{O,act}} O^-{}_{(a)} \quad \textbf{6-24}$$

$$H^+{}_{(\blacksquare)} + F \xrightarrow{k_{H,act}} H_{(\blacksquare)} \quad \textbf{6-25}$$

The backward thermal reaction between adsorbed species was also considered in this time-scale since it is a down-the-hill reaction with small activation energies [78] (Eqn. 6-26). Its characteristic time was estimated in some oxide materials as 100 [ns].

$$O_{(a)} + 2\,H_{(\blacksquare)} \xrightarrow{k_{H_2O,b}} O_{(a)} + H_2O_{(a)} \quad \textbf{6-26}$$

Recombination and trapping was considered important only at the fastest recombination centers. Liu et al (2013) considered hydroxyl species as recombination centers as well, but for water in vapor phase thermal dissociation of water is somewhat debatable, and the dissociation is mediated by holes and occurs irreversibly (Eqn.6-27 to Eqn.6-30) [9]. Electron trapping in shallow traps (Ti^{+4}) occurs in 1[ps], so it was assumed to be instantaneous (k_{et} is infinitely fast) [5].

$$O^-{}_{(a)} + h_s \xrightarrow{k_{O,rec}} O_{(a)} \quad \textbf{6-27}$$

$$H_{(\blacksquare)} + h_s \xrightarrow{k_{H,rec}} H^+{}_{(\blacksquare)} \quad \textbf{6-28}$$

$$F^+ + e_s \xrightarrow{k_{eT}} F \quad \textbf{6-29}$$

$$F + h_s \xrightarrow{k_{rec,2}} F^+ \qquad \text{6-30}$$

6.3.3 Microkinetics Analysis

A typical Microkinetics Analysis (MKA) was implemented to obtain the dynamical behavior of the coverage of the active species. It considered mass action law and mean field approximation to solve this equation analytically [79]. In the case of adsorption/desorption events, generally accepted models like Polanyi-Wigner equations were used [75]; in Chapter 7 it will be discussed the physical meaning of the MK solution when these autonomous ODE systems are solved numerically.

Obviating the limitations of a MK analysis, the dynamic behavior of the surface species is defined by a surface balance detailed in Appendix 8.4. The simulation of the initial ODE system for the active species are truly first principle simulation since up to this point no experimental information from CO_2 photocatalysis is required.

6.3.4 Steady-state approximation

Having described the fast solution for charges, and the surface events redox rates, an additional assumption to the time-scale dissociation was that electron trapping will be considered instantaneous, which will lead to a stationary surface concentration of electrons. This condition is met when the injection of free electrons to the surface is equal to its consumption. As electron and holes are generated in pairs, the injection of electron will be equal to the consumption of holes at the surface under this conditions. Therefore, the balance of charges yields the following relation

$$v_{red} + v_{rec} - v_{ox} = 0 \qquad \textbf{6-31}$$

The balances involved are also included in Appendix 8.4. Combining the results of the first ODE with Eqn.6-31 and the previous balance, an explicit function of coverage in time is obtained.

6.3.5 Integration: initial times

Using a sites balance in equilibrium (Eqn.6-32), the following solution for the initial coverage θ_i of non-active species is obtained previous to the start of the experiment.

$$\theta_i = \frac{K_i P_i}{1 + \sum K_j P_j} \qquad \textbf{6-32}$$

Where K_i and P_i are now regular adsorption constant and partial pressure respectively. Then having the initial coverage the problem is a typical non-linear ODE system with an initial condition (Eqn.6-33 and Eqn.6-34), which can be integrated using a wide variety of stiff ODE solvers (*Matlab ODE23s*); θ_a and θ_p are coverage of active species and heavy products respectively.

$$\frac{\partial \boldsymbol{y}}{\partial t} = \boldsymbol{f}(\boldsymbol{y}) \qquad \textbf{6-33}$$

$$\boldsymbol{y} = \begin{bmatrix} P_i \\ \vdots \\ \theta_p \\ \vdots \\ \theta_a \\ \vdots \end{bmatrix} \qquad \textbf{6-34}$$

The initial value for surface electrons (c_{es}) and holes (c_{hs}) were calculated at the beginning of each integration step using the algorithm of the Appendix 8.2. Such complete set of equations includes also the formation of products in a slow time-scale (CO, CH_4, H_2, O_2 and other intermediates). However, at very early times when illumination starts those species were invariant and the system was reduced to the surface balances described in Appendix 8.2, leading to a classical microkinetics analysis with static partial pressures. The estimation of the inputs parameters of the MKA problem are presented in Table 6-1; the inputs for the MKA model are still based on first-principles calculations only.

Table 6-1. MKA redox activation parameters

Parameter	Estimation	Reference
$\boldsymbol{k_{H,act}}$	$1 \times 10^{-17}[m^2/s]$	[80]
$\boldsymbol{k_{O,act}}$	$5 \times 10^{-11}[m^2/s]$	[80]
$\boldsymbol{k_{eh,rec}}$	$2 \times 10^{-28}[m^5/s]$	[56]
$\boldsymbol{k_{H_2O,act}}$	$1 \times 10^{-14}[m^3/s]$	[56]
$\boldsymbol{k_{OH^-,act}}$	$1 \times 10^{-14}[m^3/s]$	[56]
$\boldsymbol{k_{O,rec}}$	$1 \times 10^{-14}[m^3/s]$	[56]
$\boldsymbol{k_{H,rec}}$	$1 \times 10^{-14}[m^3/s]$	[56]
$\boldsymbol{C_T^{\,2} k_{H_2O,b}}$	$1 \times 10^{7}[1/s]$	[79]

For the conditions described in Chapter 4, and using the procedure described in Appendix 8.4, the initial coverages of the active species leading to further reaction is presented in Figure 6-1.

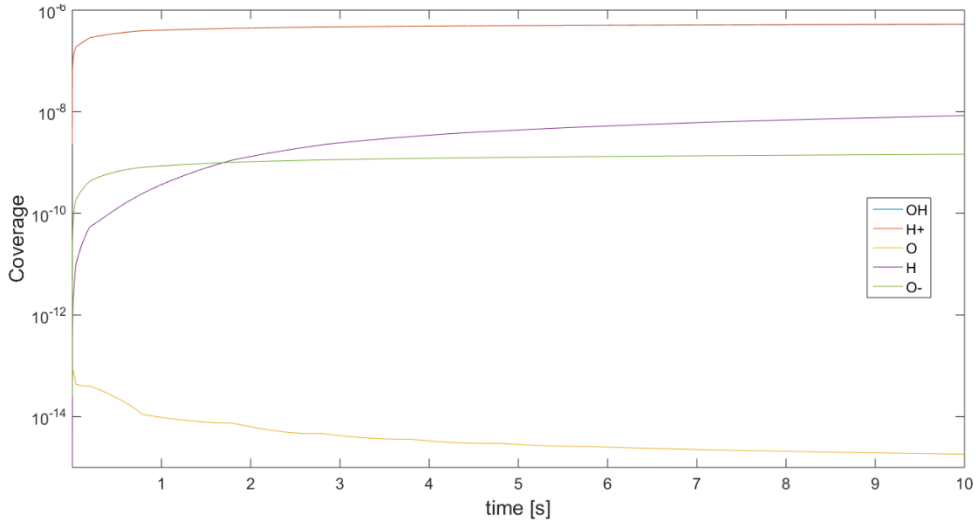

Figure 6-1 Coverage of active species during the first 10[s] of reaction. Experimental conditions: P=1.5 [bar], I=200 [W/m^2], T=30 [°C], 1.5%CO_2, 0.6 %H_2O

6.3.6 Integration: longer times

Once the active species are formed and reach a steady-state in the first seconds of the experiments, the reaction network predicted by DFT simulations from He et al (2010) was used to describe the slow interactions that produces both intermediates and gas products. Combining this information with simple models for backwards oxidation yields the following reaction network (redox-coupled nuclei combination)

$$CO_{2_{(a)}} + 2\,H_{(\blacksquare)} \overset{k_1}{\rightarrow} HCOOH_{(a)} + \blacksquare \qquad \textbf{6-35}$$

$$CO_{2_{(a)}} + 2\,H_{(\blacksquare)} \overset{k_2}{\rightarrow} CO_{(a)} + H_2O_{(\blacksquare)} + \blacksquare \qquad \textbf{6-36}$$

$$HCOOH_{(a)} + 4\,H_{(\blacksquare)} \overset{k_3}{\rightarrow} CH_3OH_{(a)} + H_2O_{(\blacksquare)} + 3\blacksquare \quad \textbf{6-37}$$

$$CH_3OH_{(a)} + 3\,O^-{}_{(a)} + 3h^+ + 2\blacksquare \overset{k_4}{\rightarrow} CO_{2_{(a)}} + 2H_2O_{(\blacksquare)} + 3\,* \quad \textbf{6-38}$$

$$CO_{(a)} + O_{(a)} \overset{k_5}{\rightarrow} CO_{2_{(a)}} + * \quad \textbf{6-39}$$

$$2\,H_{(\blacksquare)} \overset{k_6}{\rightarrow} H_{2_{(a)}} + \blacksquare \quad \textbf{6-40}$$

$$H_{2_{(\blacksquare)}} + \blacksquare \overset{k_7}{\rightarrow} 2\,H_{(\blacksquare)} \quad \textbf{6-41}$$

$$2\,O_{(a)} \overset{k_8}{\rightarrow} O_{2_{(a)}} + * \quad \textbf{6-42}$$

$$O_{2_{(a)}} + * \overset{k_9}{\rightarrow} 2\,O_{(a)} \quad \textbf{6-43}$$

$$CH_3OH_{(a)} + 2\,H_{(\blacksquare)} \overset{k_{10}}{\rightarrow} CH_{4_{(g)}} + H_2O_{(\blacksquare)} + \blacksquare \quad \textbf{6-44}$$

At longer times, the partial pressures of reactants and products will be changing at the same time as the remaining fluctuation of coverages. It is important to notice that is not convenient to use the same integration steps for both problems, because it would require an excessively high number of integration steps. Using the mechanistic information of the previous reaction network, the MKA model described in Appendix 8.4 yields a new type of solutions describing intermediates.

This particular part of the model is a form of regression, and only requires one data set to perform a proof of concept by predicting an independent data set afterwards.

In Figure 6-2 the progression of gaseous products is shown. The fitting data procedure is the same as the described in Chapter 3 and the Appendix 8.1.

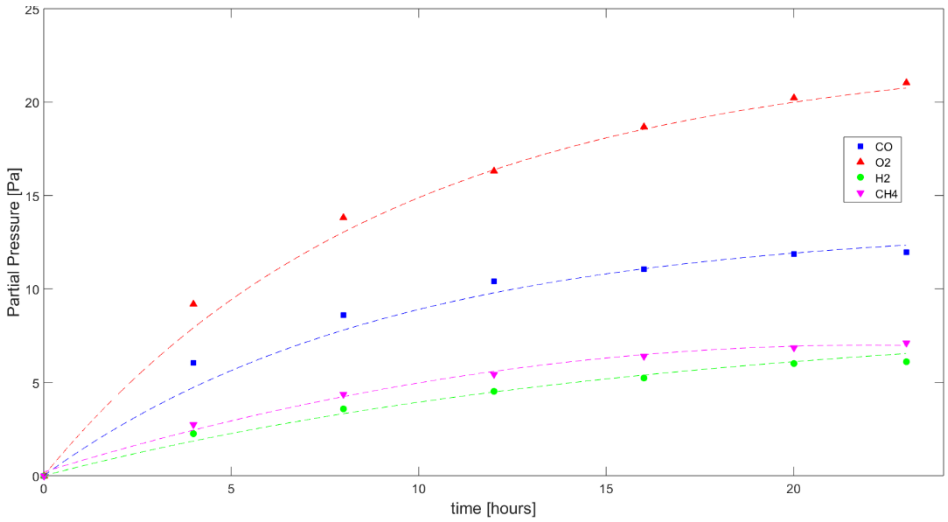

Figure 6-2 Experimental CO_2 reduction vs MKA fitted model. Experimental and simulation conditions: P=1.5[bar], I=200 [W/m^2], T=30 [°C], 1.5% CO_2, 0.6 %H_2O. The dashed lines (--) are the model predictions.

6.3.7 Discussion

Once the MK model parameters were fitted to the experimental measured production of gaseous species at the slow timescale, the change of the initial solution was simulated using same parameters shown in Table 6-1 at identical conditions but at 10 times illumination; this is 2,000[W/m^2]. Then, using the MKA fitted parameters described in Appendix 8.4 and same integration procedure as the slow time-scale, the production of gaseous species was simulated. The results are presented in Figure 6-3.

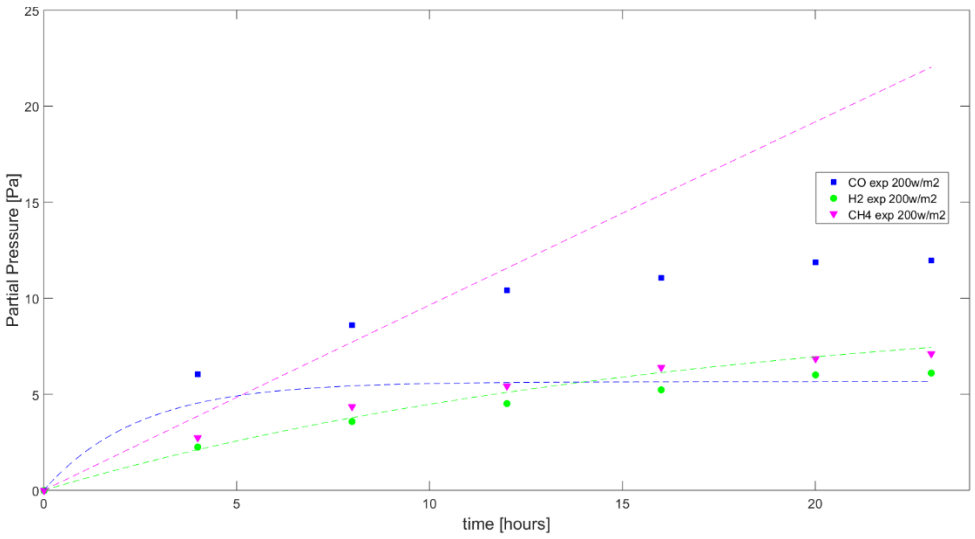

Figure 6-3 Experimental CO_2 reduction vs MKA model prediction. Experimental conditions: P=1.5[bar], I=200 [W/m^2], T=30 [°C], 1.5 %CO_2, 0.6 %H_2O. The dashed lines (--) are the model predictions for same conditions at I=2,000 [W/m^2].

Not surprisingly, the results shown in Figure 6-2 predicts a more accurate trend compared to the coarse grain models results presented in Figure 4-7. This better fit is suitable since two more parameters are introduced. In regards to the predictions of the model to an extreme case where illumination is 2,000 [W/m^2], in Figure 6-3 can be seen that a change of selectivity to methane is roughly predicted. Although it does not accurately predict the experimental results of Pougin et al (2016) presented in Figure 2-12, this model shows better capability to explain the light dependent selectivity's that coarse-grain models do not address. If more rigorously implemented, an MKA model like this could certainly predict quantitatively other intermediate cases as well; similar works have predicted an even production of CO and CH_4 at 1,000 [W/cm^2] [65, 81]. Therefore, a consistent tendency to enhanced production of methane is favored by increasing light intensity, and it is captured by mechanistic models.

In contrast to the qualitative results presented in Figure 6-3, quantitative results are harder to achieve since the concepts of intrinsic activity must be taken into account. In practice, light intensity varies along the film and the MKA models will only explain trends locally. A more rigorous regression should consider ultra-thin P25 films and detection apparatus with much higher sensitivity. In addition to this, there are other limitations for numerical results obtained from deterministic numerical resolutions. Said limitations are related to heterogeneities of the material and the discrete nature of the reaction. An introduction to stochastic models will be presented in Chapter 7 as potential candidates to better represent photocatalytic reactions.

6.4 Conclusions

In this chapter we have made a proof of concept that it is possible to link macroscopic reaction rates with charge-carrier equations, redox phenomena, gas-solid adsorption, and regular combination reaction mechanisms. Furthermore, the first motivation to pursue more complex models was a change methane selectivity under higher illumination. Since it is pointless to use deeper mechanistic models on polycrystalline materials under heterogeneous light intensity, like P25 thick films, we used a simple Microkinetics Analysis (MKA) to qualitatively predict said increase in methane selectivity at higher average light intensity.

The methodology proposed a dissociation of the time-scales to obtain a simple and inexpensive computational resolution. Light absorption and the movement of free electrons and holes were identified as the fastest processes (femtoseconds), whose stationary solution was followed by dynamic adsorption and fast redox activation steps

that progress in time (micro to miliseconds) and led to the formation of active species like O and H. Such species reach an almost stationary coverage and trigger a reaction network of different nuclei combinations in a longer time-scale (hours). All the inputs for the MKA model were obtained from first-principle estimations, and the slow reaction network was defined using reaction mechanisms proposed by He et al (2010). These last reaction parameters were fitted using the methodology described in Appendix 8.1. Once the model was fitted to the experimental data obtained for thick films under 200[W/m^2], a prediction of the progression of the reaction at 2,000[W/m^2] was made.

The MKA results showed a better fit to the experimental points, which had no special merit since 2 more parameters were introduced (desorbed CH_3OH and HCOOH cannot be measured by the GC equipment). However, the prediction of the observed trend in methane selectivity was well described, suggesting that more realistic reaction mechanisms are important to capture the influence of light out of experimental limits.

CHAPTER 7

CONCLUSIONS AND FUTURE STEPS

In this work, both a methodology and an experimental setup were developed for the study of intrinsic kinetics of P25 for CO_2 reduction. The experiment was designed simplifying optics aspects and favoring a saturation kinetics to obtain general trends for reaction rates.

Additionally, in Chapter 3 and 4 the catalyst loads were wisely selected in order to obtain useful parameters for light dependent reaction constants. A proof of concept using a thin film was also performed, introducing the concept of optical effectiveness. Under standard conditions and low illumination, an optical effectiveness of 67% for a thin film was obtained. The measured CO_2 reduction activity of the material was roughly 1,000 times higher compared to similar works were the catalyst load was not thoroughly engineered, suggesting that optical limitations are in practice the dominant phenomena in CO_2 photocatalysis.

In Chapter 5, a mathematical work based on dimensional analysis and perturbation expansion solutions was performed to show that mass transfer limitations are unlikely in this experiment. An important feature obtained is that the result can be extrapolated to other cases easily where the influence of diffusion might be more important.

Finally in Chapter 6, a proof of concept using a multi-scale analysis was performed to show the robustness of mechanistic reaction models compared to coarse-

grain approximations. Although the results obtained are just qualitative, the MKA solution to the problem was conceptualized and showed an interesting trend of enhanced methane selectivity under higher illumination. This results confirmed experimental literature showing this particular behavior of the reaction.

Taking into account the results of this work and the limited amount of time to present this it as a Master of Science final examination, the following recommendations should be considered in future research work that were not addressed in this examination:

I. Since the influence of light was demonstrated to be extremely important in quantifying the CO_2 reduction activity of a photo-active material, a suitable continuation of this work is testing this and other materials using finer deposition techniques, like LB films. This ultra-thin films would show the actual intrinsic activities, near an optical effectiveness of 1. On the other hand, such small amount of material would require new technologies for the reactor cell and the detection equipment. For instance, micro reactors coupled to mass spectrometer seems to be a good candidate [82].

II. Optical properties of the active films can be better tailored using different amounts of stabilizers and particle concentration. In this work a previous work was used as a reference, while other more efficient deposition techniques and or conditions may exist to enhance light absorption over scattering.

III. In regards to surface reaction models, a proof of concept was shown using Microkinetics, demonstrating that mechanistic aspects are essential to achieve robust mathematical description of photocatalytic reactions under different

conditions. However, in reality there are both space and time heterogeneities that make this analysis futile when it comes to quantitative prediction of performance of complex catalysts like P25 [83]. In this way, stochastic representations of heterogeneous catalysis are nowadays powerful tools to link atomic-scale features predicted by first principles DFT and MD modeling, with meso-scale models. Said simulations can not only provide rigorous regressions taking into account semiconductors defects, dissimilar time-scales and oscillating/discrete reaction behavior, but are also key to find better photocatalysts since they can be used as predictive tools of photocatalytic performance [7]. To show this point, a Kinetic Monte Carlo routine was implemented to describe CO_2 adsorption in anatase (101). The results obtained in Appendix 8.5 shows that occurrence of bent modes that are believed to be the main precursors in CO_2 reduction, are in practice rare discrete events, which is stark contradiction with the MKA model that only assumed an evenly distributed coverage of CO_2. Another limitation of deterministic models for photocatalysis, is the assumption that reactants are evenly adsorbed in the active sites, which is not likely in nanoparticles since so called surface effects exists; KMC models deal with the spatial distribution of adsorbates [84].

IV. Regardless of the surface reaction used to represent experimental results, other complementary experiments can reveal key aspects of the reaction mechanisms. Spectroscopy and Scan Tunneling Microscopy (STM) have been used to unravel specific redox and thermal reaction steps in this field [48, 85]. The use

mono-faceted-crystal photocatalysts would enormously simplify the study of reaction mechanisms as well [86].

APPENDIX

8.1 Fitting data model and algorithm

The type of models to be used are coarse-grain models assuming pseudo Langmuir-Hinshelwood (L-H) forms for surface reaction. The coverage of the different species *i* can be defined as

$$\theta_i = \frac{K_i P_i}{(1 + \sum_i^N K_i P_i)} \quad \textbf{8-1}$$

In this approach the formation of intermediates non-desorbing products or active species is neglected. Then, the overall reaction gives a sense of what the mechanism will be assuming the pseudo Langmuir-Hinshelwood expression. The overall reaction is defined as the initial stoichiometry obtained experimentally as it follows

$$16CO_{2(ads)} + 15\,H_2O_{(ads)} \xrightarrow{k_{red}} 5H_{2(ads)} + 11CO_{(ads)} + 19O_{2(ads)} + 5CH_{4(g)} \quad \textbf{8-2}$$

Then, assuming a mass action law with a forward reaction constant k_{red}, the reduction rate can be defined as

$$r_{red} \approx \theta_{CO_2} \times \theta_{H_2O} \times k_{red} \quad \textbf{8-3}$$

And the rate for each species is given by the initial stoichiometry γ_i defined as

$$r_{red,i} = \gamma_i r_{red} \quad \textbf{8-4}$$

Finally, the backward reaction that accelerates the observed asymptotic CO concentration compared to the other species is

$$O_{2(ads)} + 2CO_{(ads)} \xrightarrow{k_{ox}} 2CO_{2(ads)} \quad \textbf{8-5}$$

Whose reaction rate is defined similarly to the reduction rate as it follows

$$r_{ox} \approx \theta_{O_2} \times {\theta_{CO_2}}^2 \times k_{ox} \quad \textbf{8-6}$$

The model has 5 adsorption constants and 2 reaction constants to be fitted (methane is not considered as an adsorbing species). The way to find those 7 parameters will be starting with a guess that makes all the coverages $O(1)$, this is $K_i P_i \approx 1$. Then, the first guess for reaction rates will be considering that at the beginning of the reaction the reduction rates matches the observed reduction rate, and that by the end of the experiments, the reduction rate and the oxidation rate are approximately zero. Having the initial guesses, the following ODE system was solved using Matlab ODE23s

$$\frac{\partial \boldsymbol{P}}{\partial t} = \boldsymbol{f}(\boldsymbol{P}) \quad \textbf{8-7}$$

Where $\boldsymbol{f}$ it is an explicit vector value vector function dependent on the stoichiometry of the reduction and oxidation rates. Integrating the previous equation yields trying theoretical predictions. It must be noticed that many local minima can be obtained with regular optimization processes for the 7 parameters that minimizes the square error of the prediction at each experimental point. In order to find a global

minima a stochastic search was made using an evenly weighted error function described in Eqn. 8-8.

$$\chi_{i,k} = \sum\sum \left[\frac{\left(y_{pred,j}(t_i) | \boldsymbol{p}_k - y_{exp,j}(t_i) \right)}{y_{j,max}} \right]^2 \quad \textbf{8-8}$$

Where

t_i : Discrete time point *i*

$y_{exp,j}$: Discrete observed value for the variable *j* at time *i*

$y_{pred,j}$: Continuous predicted function of time evaluated at time t_i

$y_{j,max}$: Characteristic max value of the variable *j*

p_k : Set of parameters at trial *k*

In order to explore the different possibilities for the set of parameters, a new random modification for the vector will be generated as it follows

$$\boldsymbol{p}_{k+1} = \boldsymbol{p}_k \cdot \boldsymbol{f}_k \quad \textbf{8-9}$$

$$f_{k,l} = 10^{(-1+2*\xi_{k,l})} \quad \textbf{8-10}$$

Where

$p_{k,l}$: random number at trial k for the parameter l

With this method the wide variety of orders of magnitude can be tested. In order to accept or not a new trial, a likelihood function is defined as

$$P_{k+1} = \exp\left(-\left(\chi_{i,k+1} - \chi_{i,k}\right)\right) \qquad \textbf{8-11}$$

If the new set of parameter minimizes the error, the move is accepted, if not, the movement is rejected or accepted depending on a second random number. If the random number generated is bigger that P_{k+1}, the movement is rejected, otherwise is rejected. This methodology ensures that different order of magnitudes are tried and is self-exploratory. After approximately 1000-5000 steps, a regular optimization using *fmin* Matlab tool is performed to better find the exact value of the minima found. The results of the fitting procedure are presented in Table 8-1.

Table 8-1. Fitted parameters of L-H model

Fitted	Initial guess	Parameter
4.5E-09	4.4E-10	k_{red}
8.9E-27	5.8E-08	k_{ox}
2.4E+01	4.4E-04	K_{CO2}
2.3E+00	1.1E-03	K_{H2O}
1.5E-03	8.4E-02	K_{CO}
7.7E+03	4.9E-02	K_{O2}
6.7E-03	1.7E-01	K_{H2}

The fitting procedure of the MKA model presented in Chapter 6 was solved similarly, but using nine parameters instead of seven. Only the initial guess of CH_3OH and HCOOH coverages, and the stiffness of the ODE system needed special treatment. The results are presented in Table 8-2.

Table 8-2. Fitted parameters of MKA model

Fitted	Initial guess	Parameter	Units
1.1E-37	4.8E-37	k_1	1/s
3.2E-37	5.2E-39	k_2	1/s
1.3E+31	2.6E+30	k_3	1/s
1.7E+65	1.1E+75	k_4	-
1.6E-30	1.9E-36	k_5	1/s
1.8E-21	2.0E-39	k_6	1/s
1.4E-80	2.2E-49	k_7	1/s
1.8E-95	1.7E-25	k_8	1/s
5.5E-42	5.4E-46	k_9	1/s
1.4E+31	7.6E+31	k10	1/s

8.2 Knudsen Diffusion

Neglecting the meso-pores induced by the use of PEG during the dip-coating process, in an ideal case the particles will arrange as the sketch in **Error! Reference source not found.**. The characterization of the average properties of the pores are going to follow this idealization.

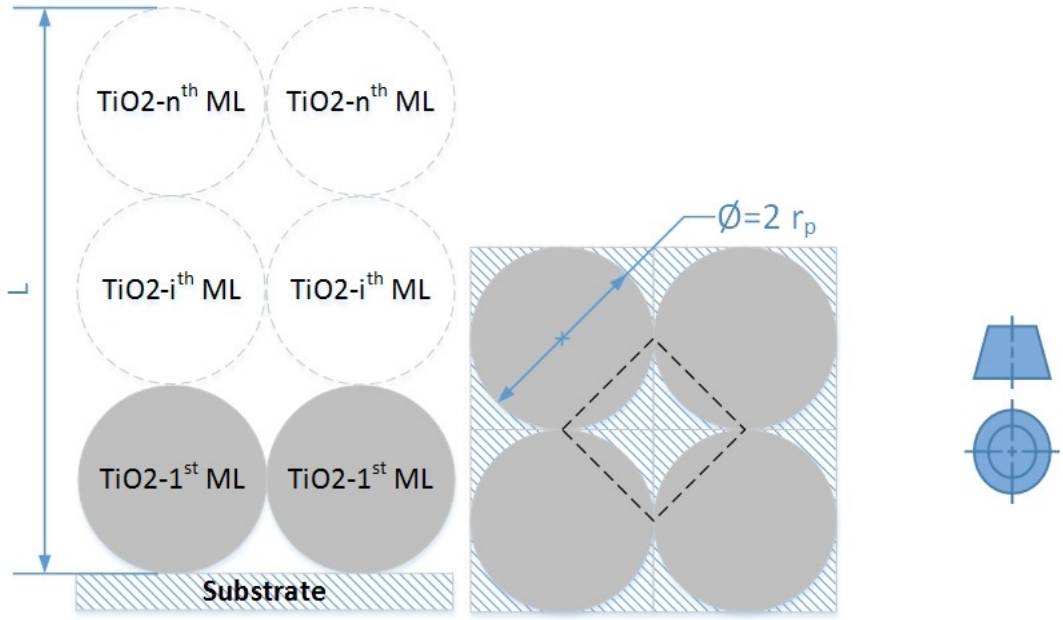

Figure 8-1 Ideal superposition of P25 nanoparticles in a film

This arrangement is a superposition of ideal ML. However, the overall porosity of this idealization does not match the porosity obtained after the dip-coating process. The real inter particle distance of the film (δ) using the same cubic centered unit cell can be calculated using the apparent density of the film in Eqn. 8-12.

$$\delta = r_p \times \left(\left(\frac{\rho_{app}}{\rho_{TiO_2}} \frac{3}{4\pi} \right)^{-\frac{1}{3}} - 2 \right) \quad \textbf{8-12}$$

Where

ρ_{TiO2} : TiO_2 density (4.2 [g/cm^3])

ρ_{app} : Film density (0.7 [g/cm^3])

r_P : Nanoparticle radius (10 [nm])

Then, the particle distance can be estimated as 19[nm]. Using this information the arrangement porosity can be calculated using Eqn. 8-13. Additionally, the volume of the void in the arrangement and the effective cylindrical pore radius can be calculated using Eqn. 8-14 and Eqn. 8-15 respectively.

$$\varepsilon_{film} = 1 - \frac{4\pi}{3} \left(\frac{r_p}{2r_p + \delta} \right)^3 \quad \textbf{8-13}$$

$$V_{void} = \frac{4}{3} \pi {r_p}^3 \left(\frac{\varepsilon_{film}}{1 - \varepsilon_{film}} \right) \quad \textbf{8-14}$$

$$R_{app} = \frac{2\, V_{void}}{4\pi {r_p}^2} \quad \textbf{8-15}$$

The radius R_{app} is approximately 35 [nm], which gives a Knudsen number of 1.67. In this case, neither Knudsen (D_K) nor Molecular Diffusion (D_{CO2}) can be

neglected. Then, the effective diffusivity D_e in channels can be calculated using the sum of two mass transfer resistance in series that is presented in Eqn. 8-16.

$$\frac{1}{D_e} = \frac{1}{D_K} + \frac{1}{D_{CO_2}} \quad \textbf{8-16}$$

The value of the effective diffusivity D_e is estimated as 1.75×10^{-7}. The next step is to determine the ideal channel length neglecting film heterogeneities. In order to do so the experimental surface loading S_{cat} estimation is used in Eqn. 8-17 to calculate the number of ML.

$$ML = \frac{S_{cat}}{\frac{4\pi {r_p}^3}{3} \times \rho_{TiO_2} / \left(r_p + \delta\right)^2} \quad \textbf{8-17}$$

Finally, the length L_C and approximated active area a per length of an ideal channel can be estimated by using Eqn. 8-18 and Eqn. 8-19.

$$L_c = 2 \times r_p \times ML \quad \textbf{8-18}$$

$$a = 4\pi {r_p}^2 \quad \textbf{8-19}$$

Once the average characterization for the pores has been done, it can be inferred from the existence of meso-pores that this estimation is not entirely valid, because not all the pores are actually accessible. The film in reality can be represented as a fractal geometry, and the way to solve that problem involves the approximation of a percolating network and a material balance in each node of the network [87]. For instance, only these ideal pore properties will be considered, and the new problem of mass transfer

with pseudo-homogeneous is presented in Figure 8-2, and its conservation equation in stationary state is presented in Eqn.8-20.

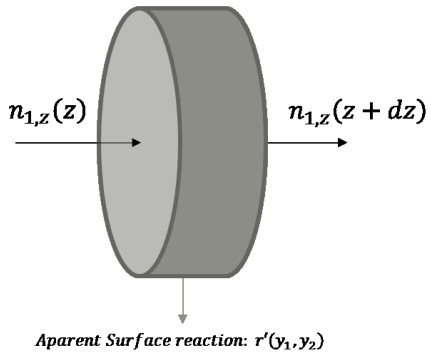

Figure 8-2 Idealized pore differential balance with an apparent wall zeroth order reaction.

$$D_{K,CO_2}\frac{d^2c}{dz^2} + \gamma_i 2\pi r_c \times J'_{net,0} = 0 \qquad \textbf{8-20}$$

Where

c : Reactant (CO_2) concentration ($1.22x10^{-4}$ [moles/m^3].)

r_c : Ideal channel radius (8 [nm].)

$J'_{net,0}$: Initial surface reaction rate per catalyst surface area ([moles/m^2 s^{-1}])

The reaction pore is assumed to be in the same time-scale as the reaction time defined in Chapter 6. Therefore, the channel is assumed to be stationary. The reaction is also assumed to the initial reaction rate. Then, a Damkohler like number can be obtained for the reaction-diffusion problem

$$\frac{d^2\bar{c}}{d\bar{z}^2} + Da_K = 0 \qquad \textbf{8-21}$$

$$Da_K = \frac{{L_p}^2}{D_{K,CO2}} \times \gamma_i \frac{2\pi r_c \times J_{net,0}}{c_{CO_2,0}} \qquad \textbf{8-22}$$

Where

$\bar{c}$: Non-dimensional CO_2 concentration

$\bar{z}$: Non-dimensional axial dimension

L_p : Ideal pore length (1.4 [μm])

$$\bar{c} = 1 - \frac{\bar{z}^2}{2} Da_K + \frac{Da_K}{2} \bar{z} \qquad \textbf{8-23}$$

Finally, it can be seen that the concentration profile inside the Channel is defined by a similar Damkohler number than external diffusion ε in Chapter 5 A simple comparison to avoid a full resolution of the problem is to obtain the ratio between those non-dimensional numbers:

$$\varepsilon / Da_K = \left(\frac{a' L A_R}{D_{CO2}} \right) \Bigg/ \frac{3{L_p}^2}{\left(\frac{8K_B T}{\pi m} \right)^{1/2} \pi} \qquad \textbf{8-24}$$

In this comparison, both processes are compared without using the reaction term itself, neither a radius for the ideal pore. If the length of the channel can be approximated to the film thickness, the ratio of external diffusion to internal diffusion can be

approximated to the following expression that demonstrates that under normal circumstances external diffusion is always more limiting.

$$\varepsilon/_{Da_K} = \left(\frac{a'LA_R}{D_{CO2}}\right) \Bigg/ \frac{3{\delta_f}^2}{\left(\frac{8K_BT}{\pi m}\right)^{1/2}\pi} \ll 1 \qquad \textbf{8-25}$$

8.3 Finite Fourier Transform

Let's use the following form for the solution and the basis function

$$\hat{c}_i^0 = \hat{c}_{i,n}^0(\tau)\Phi_{i,n}^0(Y) \tag{8-26}$$

$$\Phi_{i,n}^0(Y) = \sqrt{\frac{2}{\sqrt{\varepsilon}}}\cos\left(n\pi Y/\sqrt{\varepsilon}\right) \tag{8-27}$$

$$\Phi_{i,0}^1(Y) = \sqrt{\frac{1}{\sqrt{\varepsilon}}} \tag{8-28}$$

The eigenvalue problem for the basis function gives:

$$\frac{\partial^2\Phi_{i,n}^0(Y)}{\partial Y^2} = {\lambda_{i,n}}^2\Phi_{i,n}^0(Y) \tag{8-29}$$

$$\lambda_{i,n} = \frac{n\pi \times 2^{1/4}}{\varepsilon^{3/4}} \tag{8-30}$$

Now Applying an FFT transformation to the PDE

$$\int_0^{\sqrt{\varepsilon}} \frac{\partial\hat{c}_i^0}{\partial\tau}\Phi_{i,n}^0 dY = \frac{\hat{c}_{i,n}^0}{\partial\tau} \tag{8-31}$$

$$\int_0^{\sqrt{\varepsilon}} \frac{\partial^2\hat{c}_i^0}{\partial Y^2}\Phi_{i,n}^0 dY = \Phi_{i,n}^0\frac{\partial\hat{c}_i^0}{\partial Y}\bigg|_{Y=0}^{Y=\sqrt{\varepsilon}} - \int_0^{\sqrt{\varepsilon}} \frac{\partial\Phi_{i,n}^0}{\partial Y}\frac{\partial\hat{c}_i^0}{\partial Y}dY \tag{8-32}$$

$$\int_0^{\sqrt{\varepsilon}} \frac{\partial^2 \hat{c}_i^0}{\partial Y^2} \Phi_{i,n}^0 dY$$

$$= \Phi_{i,n}^0\left(\sqrt{\varepsilon}\right) \frac{\partial \hat{c}_i^0}{\partial Y}\left(\sqrt{\varepsilon}\right) - \Phi_{i,n}^0(0) \frac{\partial \hat{c}_i^0}{\partial Y}(0) - \frac{\partial \Phi_{i,n}^0}{\partial Y} \hat{c}_i^0 \Big|_{Y=0}^{Y=\sqrt{\varepsilon}} \quad \textbf{8-33}$$

$$+ \int_0^{\sqrt{\varepsilon}} \frac{\partial^2 \Phi_{i,n}^0}{\partial Y^2} \hat{c}_i^0 dY$$

Using previous equation and replacing into the PDE yields

$$\frac{\partial \hat{c}_{i,n}^0}{\partial \tau} = \sqrt{\frac{2}{\sqrt{\varepsilon}}} A_i^1 - {\lambda_{i,n}}^2 \hat{c}_{i,n}^0 \quad \textbf{8-34}$$

Using the initial condition we obtain

$$\hat{c}_{i,0}^0 = \sqrt{\frac{2}{\sqrt{\varepsilon}}} A_i^1 \tau \quad \textbf{8-35}$$

$$\hat{c}_{i,n}^0 = \frac{A_i^1 \varepsilon}{(n\pi)^2}\left(1 - \exp\left(-{\lambda_{i,n}}^2 \tau\right)\right) \quad \textbf{8-36}$$

So the modified solution for both product and reactants:

$$\hat{c}_i^0 = \sqrt{2}\varepsilon^{3/4} A_i^1 \sum_{n=1}^{\infty} \frac{\cos\left(\pi n(1-\tilde{z})\right)}{(n\pi)^2}\left(1 - \exp\left(-\frac{\sqrt{2}(n\pi)^2}{\varepsilon^{5/4}}\tau\right)\right) + \sqrt{\frac{2}{\varepsilon}} A_i^1 \tau \quad \textbf{8-37}$$

Finally, the overall *O*(1) solution for reactants

$$c_i$$

$$= \lambda_i c_c \left(1 - \sqrt{2}\frac{\gamma_i}{\lambda_i \beta_i}\tau \right. \tag{8-38}$$

$$\left. - \gamma_i \frac{\sqrt{2}\varepsilon^{5/4} \sum_{n=1}^{\infty} \frac{\cos\left(\pi n(1-\tilde{z})\right)}{(n\pi)^2} \left(1 - \exp\left(-\frac{\sqrt{2}(n\pi)^2}{\varepsilon^{5/4}}\tau\right)\right)}{\lambda_i \beta_i} \right)$$

$$c_j = \lambda_i c_c \sqrt{2}\frac{\gamma_j}{\lambda_j \beta_j} \left(\tau + \varepsilon^{5/4} \sum_{n=1}^{\infty} \frac{\cos\left(\pi n(1-\tilde{z})\right)}{(n\pi)^2} \left(1 - \exp\left(-\frac{\sqrt{2}(n\pi)^2}{\varepsilon^{5/4}}\tau\right)\right)\right) \tag{8-39}$$

8.4 MKA model

Water balance

$$\frac{d\theta_{H_2O}}{dt} = 1880 \times \theta_{V1} \times P_{H_2O} - \theta_{H_2O} k_{H_2O,des} - C_{h,s}\theta_{H_2O} k_{H_2O,act}\theta_{V2} + {C_T}^2 \theta_O {\theta_H}^2 k_{H_2O,b} \quad \textbf{8-40}$$

Hydroxyl radical balance

$$\frac{d\theta_{OH^{\cdot}}}{dt} = C_{h,s}\theta_{H_2O} k_{H_2O,act}\theta_{V2} - C_{h,s}\theta_{OH^{\cdot}} k_{OH^{\cdot},act}\theta_{V2} \quad \textbf{8-41}$$

Proton balance

$$\frac{d\theta_{H^+}}{dt} = C_{h,s}\theta_{H_2O} k_{H_2O,act}\theta_{V2} + C_{h,s}\theta_{OH^{\cdot}} k_{OH^{\cdot},act}\theta_{V2} + C_{h,s}\theta_H k_{H,rec} + C_{e,s}\theta_{H^+} k_{H,act} \quad \textbf{8-42}$$

Hydrogen balance

$$\frac{d\theta_H}{dt} = C_{e,s}\theta_{H^+} k_{H,act} - 2{C_T}^2 \theta_O {\theta_H}^2 k_{H_2O,b} - C_{h,s}\theta_H k_{H,rec} \quad \textbf{8-43}$$

Oxygen radical

$$\frac{d\theta_{O^-}}{dt} = C_{e,s}\theta_O k_{O,act} - C_{h,s}\theta_{O^-} k_{O,rec} \quad \textbf{8-44}$$

Oxygen

$$\frac{d\theta_O}{dt} = C_{h,s}\theta_{OH^{\cdot}}k_{OH^{\cdot},act}\theta_{V2} + C_{h,s}\theta_{O^-}k_{O,rec} - C_{e,s}\theta_O k_{O,act} - {C_T}^2\theta_O{\theta_H}^2 k_{H_2O,b} \quad \textbf{8-45}$$

Other (Ti^{+4}) adsorbing species (CO_2, CO, O_2)

$$\frac{d\theta_i}{dt} = k_{ads,i} \times \theta_{V1} \times P_i - \theta_i k_{i,des} \quad \textbf{8-46}$$

Other O_b adsorbing species (H_2)

$$\frac{d\theta_{H_2}}{dt} = k_{ads,H_2} \times \theta_{V2} \times P_{H_2} - \theta_{H_2} k_{H_2,des} \quad \textbf{8-47}$$

Sites balance

$$\theta_{V1} = 1 - \theta_{CO_2} - \theta_{H_2O} - \theta_{CO} - \theta_{O_2} - \theta_O - \theta_{O^-} - \sum \theta_p \quad \textbf{8-48}$$

$$\theta_{V2} = 1 - \theta_{H_2} - \theta_H - \theta_{H^+} \quad \textbf{8-49}$$

Steady state approximation

$$v_{red} = C_{e,s}\theta_O k_{O,act} + C_{e,s}\theta_{H^+}k_{H,act} + C_{e,s}C_{h,s}k_{eh,rec} \quad \textbf{8-50}$$

$$v_{ox} = C_{h,s}\theta_{H_2O}k_{H_2O,act}\theta_{V2} + C_{h,s}\theta_{OH^{\cdot}}k_{OH^{\cdot},act}\theta_{V2} + C_{h,s}\theta_{O^-}k_{O,rec} + C_{h,s}\theta_H k_{H,rec} \quad \textbf{8-51}$$

Which gives a steady sub-surface electron (excess) concentration (F sites)

$$C_{e,s} = \frac{C_{h,s}\left(\theta_{H_2O} k_{H_2O,act} \theta_{V2} + \theta_{OH^{\cdot}} k_{OH^{\cdot},act} \theta_{V2} + \theta_{O^-} k_{O,rec} + \theta_H k_{H,rec}\right)}{\theta_O k_{O,act} + \theta_{H^+} k_{H,act} + C_{h,s} k_{eh,rec}} \quad \textbf{8-52}$$

Plugging this result into the previous expressions

$$C_T \times \left(\frac{1}{6} + B\right) \times \frac{r_p}{D_h} \times \left(\theta_{H_2O} k_{H_2O,act} \theta_{V2} + \theta_{OH^{\cdot}} k_{OH^{\cdot},act} \theta_{V2} + \theta_{O^-} k_{O,rec} + \theta_H k_{H,rec} + C_{e,s} k_{eh,rec}\right) = 1/6 \quad \textbf{8-53}$$

At different coverage vectors, the exact stationary solution to this equation should be found numerically. However, Taylor expanding the surface concentration of electrons as a function of C_{hs} only, it is obtained an explicit function based on a previous solution. As the ODE is solved numerically, an initial value for C_{es} was calculated fixing the new coverage at each integration step. Few iterations plugging the first estimation into the implicit original function of C_{hs} gives a rapid convergence to the exact new solution.

Using the reaction mechanism proposed by He et al (2010), the reaction rates are defined in a similar fashion assuming a mean field approximation and a mass action law.

$$r_1 = k_1 C_T \theta_{CO_2} {\theta_H}^2 \quad \textbf{8-54}$$

$$r_2 = k_2 C_T \theta_{CO_2} {\theta_H}^2 \quad \textbf{8-55}$$

$$r_3 = k_3 C_T \theta_{HCOOH} {\theta_H}^4 \quad \textbf{8-56}$$

$$r_4 = k_4 C_T {c_{hs}}^3 \theta_{CH_3OH} \theta_{O^-}{}^3 {\theta_{V2}}^2 \quad \textbf{8-57}$$

$$r_5 = k_5 C_T \theta_{CO} \theta_O \quad \textbf{8-58}$$

$$r_6 = k_6 C_T {\theta_H}^2 \quad \textbf{8-59}$$

$$r_7 = k_7 C_T \theta_{H_2} \theta_{V2} \quad \textbf{8-60}$$

$$r_8 = k_8 C_T {\theta_O}^2 \quad \textbf{8-61}$$

$$r_9 = k_9 C_T \theta_{O_2} \theta_{V1} \quad \textbf{8-62}$$

$$r_{10} = k_{10} C_T {\theta_H}^2 \theta_{CH_3OH} \quad \textbf{8-63}$$

The surface balances are equivalent to the following system lumped in a slower timescale, where adsorption can now be considered infinitely fast

$$\begin{bmatrix} \dot{P}_{CO_2} \\ \dot{P}_{H_2O} \\ \dot{P}_{CO} \\ \dot{P}_{O_2} \\ \dot{P}_{H_2} \\ \dot{P}_{CH_4} \end{bmatrix} = C_{scale} \begin{bmatrix} r_5 + r_4 - r_1 - r_2 \\ r_2 + r_3 + 2r_4 + r_{10} \\ r_2 - r_5 \\ r_8 - r_9 \\ r_6 - r_7 \\ r_{10} \end{bmatrix} \quad \textbf{8-64}$$

$$\begin{bmatrix} \dot{\theta}_{HCOOH} \\ \dot{\theta}_{CH_3OH} \end{bmatrix} = \frac{1}{C_T} \begin{bmatrix} r_1 - r_3 \\ r_3 - r_4 - r_{10} \end{bmatrix} \quad \textbf{8-65}$$

$$\begin{bmatrix} \dot{\theta}_{A1} \\ \vdots \\ \dot{\theta}_{An} \end{bmatrix} = \begin{bmatrix} f_1 \\ \vdots \\ f_n \end{bmatrix} \quad \textbf{8-66}$$

$$C_{scale} = \left(\frac{RT}{V_R}\right)\frac{A_{cat}}{N_A} \qquad \textbf{8-67}$$

Now the resolution is a nonlinear ODE system where the formation of active species changes simultaneously with the coverages and partial pressure of the products. In this system, the factor C_{scale} is a constant that converts the production of moles in surface to partial pressures in gas phase. The integration started after the transient time for the active species to form an initial stationary state, described in Chapter 6 as the fast time scale.

8.5 Kinetic Montecarlo Calculations for CO_2 adsorption

Based on the work of Sorescu et al (2011), below a representation of TiO_2 Anatase (101) [88]

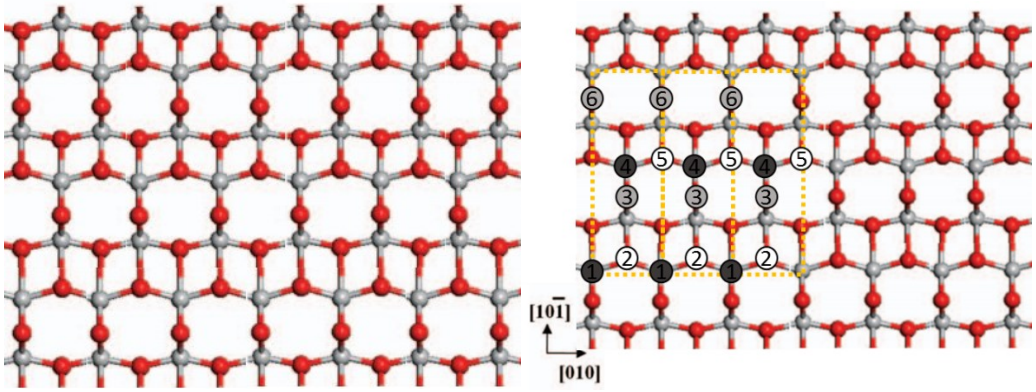

Figure 8-3 Anatase (101) lattice and sub-lattice representation. [Sorescu et al,2011]

On the right, a sub lattice definition recommended by AP Jansen (2012) [84]. All the details about the representation of adsorption and desorption processes as probabilities in time can be found on similar works in literature [89]. Below, a description of different CO_2 adsorption modes predicted by DFT simulations in the work of Sorescu et al (2011), and its representation in a computational discrete lattice.

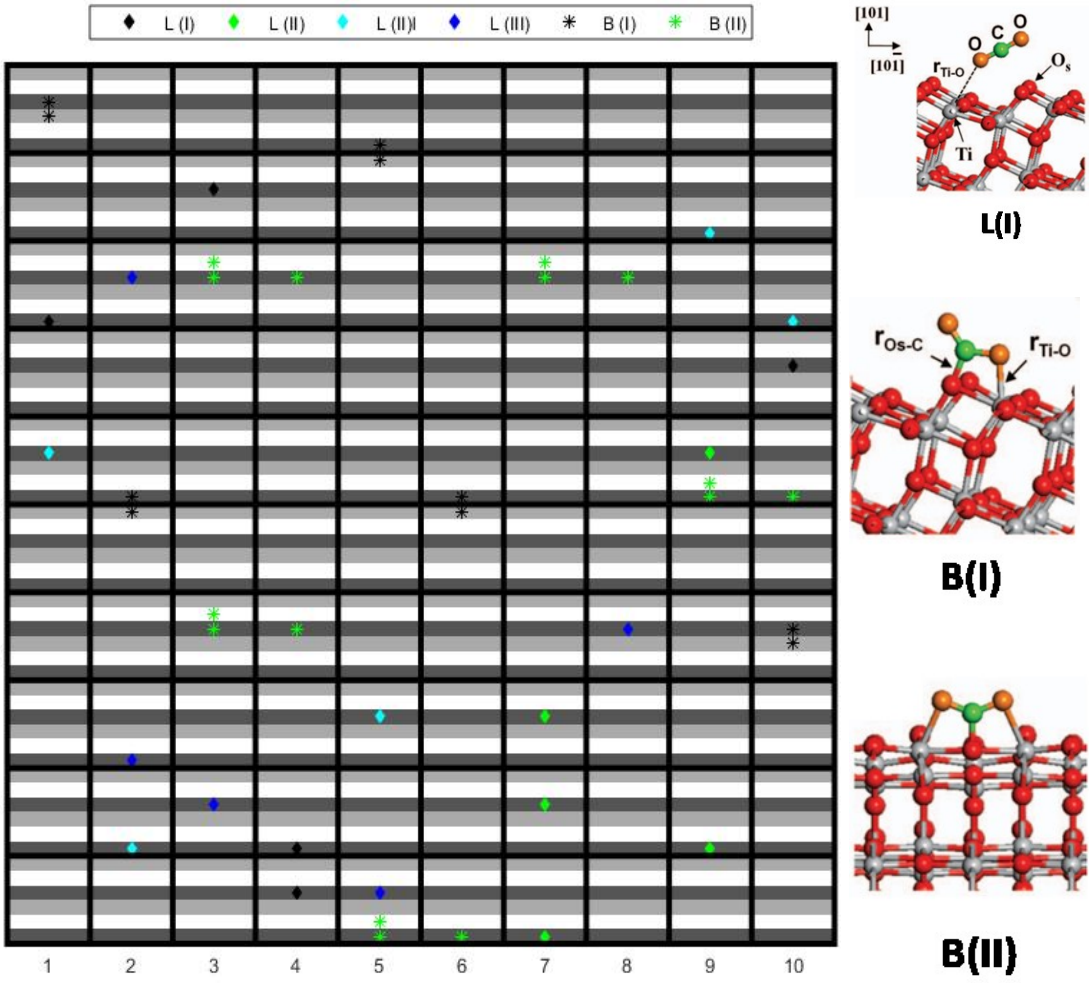

Figure 8-4 Lattice computational representation and predicted adsorption mode [Sorescu et al, 2011]

The different modes for adsorption in the active sites sub lattice can be represented as

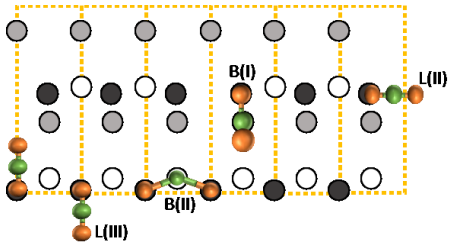

Figure 8-5 Sub-lattice configurations for different adsorption modes

It must be noticed that each molecule has its own lattice requirement to correctly adsorb. The lattice requirements and the valid movements definitions where identified with an own MATLAB code. For example, a valid random configuration generation was tested in the 10x10 lattice presented above. All the movements will be represented as Transition States, with predicted activation energies according to the DFT simulations from the work of Sorescu et al (2011). The events considered are presented in Table 8-3.

Table 8-3. Possible events in CO_2 adsorption

Events…25 total
CO2 L(I), L(II), L(II)l, L(III) B(I) and B(II) Adsorption
CO2 L(I), L(II), L(II)l, L(III) B(I) and B(II) Desorption
L(I) diffusion
L(II) ←→ L(II),l conversion
L(II) ←→ B(II) to right conversion
L(II)l ←→ B(II) to left conversion
L(III) ←→L(I) ←→L(II), L(II)l conversion
L(III) ←→ B(I) conversion

For instance only the influence of the activation energies and the change in free energy were used to estimate transition probabilities, because it does not require the calculation of pre-exponential factors and explains most of the trends that will be seen in a more thorough model; neither entropic effects in the free energy of the ensemble, or sticking coefficients were included. Subsequently, an initial lattice with no species adsorbed was defined, and the process was assumed to be a Markov chain. In other

words, the process is stochastic and only depends on its actual state [90]. This process is also assumed to be stationary, with fixed probabilities in time. The Master Equation that describes the probabilities of the system to be in different states over time is

$$\frac{dP_\alpha}{dt} = \sum_\beta W_{\boldsymbol{\alpha\beta}} P_{\boldsymbol{\beta}} - W_{\boldsymbol{\beta\alpha}} P_{\boldsymbol{\alpha}} \quad \textbf{8-68}$$

Where

P_α, P_β : Probability of system being in α or β configurations

$W_{\alpha\beta}$, $W_{\beta\alpha}$: Transition matrix probabilities

In a KMC representation, the transition probability matrix is defined by the transitions states rates, or probabilities in time. Then, this process can be conveniently represented as a sequence of discrete events in time given by the probability of the different possible event to occur, and the generation of a random-number to define what movement to choose. This is also known as Gillespie Algorithm.

$$\sum_{p=0}^{i-1} k_p \leq \rho_1 k_{tot} \leq \sum_{p=0}^{i} k_p \quad \textbf{8-69}$$

$$t_{i+1} \rightarrow t_i - \frac{ln(\rho_2)}{k_{tot}} \quad \textbf{8-70}$$

Where

t_i : Total discrete time increase at step i

ρ_i : Random number I

ρ_i : Random number II

k_p : Probability in time of event p

k_{tot} : Sum of probability in time of all events possible

Running this algorithm in a Matlab Code, the simplified CO_2 adsorption process in dark was then represented by:

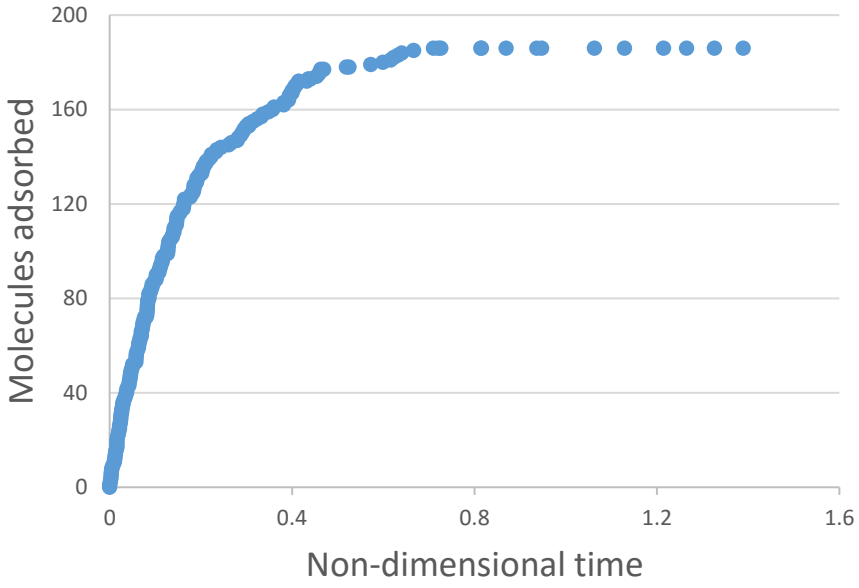

Figure 8-6 CO_2 uptake in dark at room temperature.

The occurrence of different modes in time are presented in **Figure 8-7**.It can be inferred immediately that some forms of CO_2 are very unlikely; some of them occurs in very long time-scales only. An interesting application of this result to CO_2 photocatalysis can be a quantitative prediction of what modes will be observed more

often, because DFT simulations alone can quantify activation energies for further reaction mechanisms [52, 91]. For example, it is was predicted by Sorescu et al (2011) and other authors that the form *BI* is much more stable in the presence of a free electron in the lattice than *L*I, *L*II and *LII*I; and just requires 1 e^-, which means that is much susceptive to activation than the rest of the linear species. Nevertheless, the result from KMC predicts that *BI* formation in time is highly unfavorable compared to linear species. Then, in a reaction scheme, both bent and linear modes can be competitive (BI and LI) even when DFT predicts a more likely activation for bent molecules.

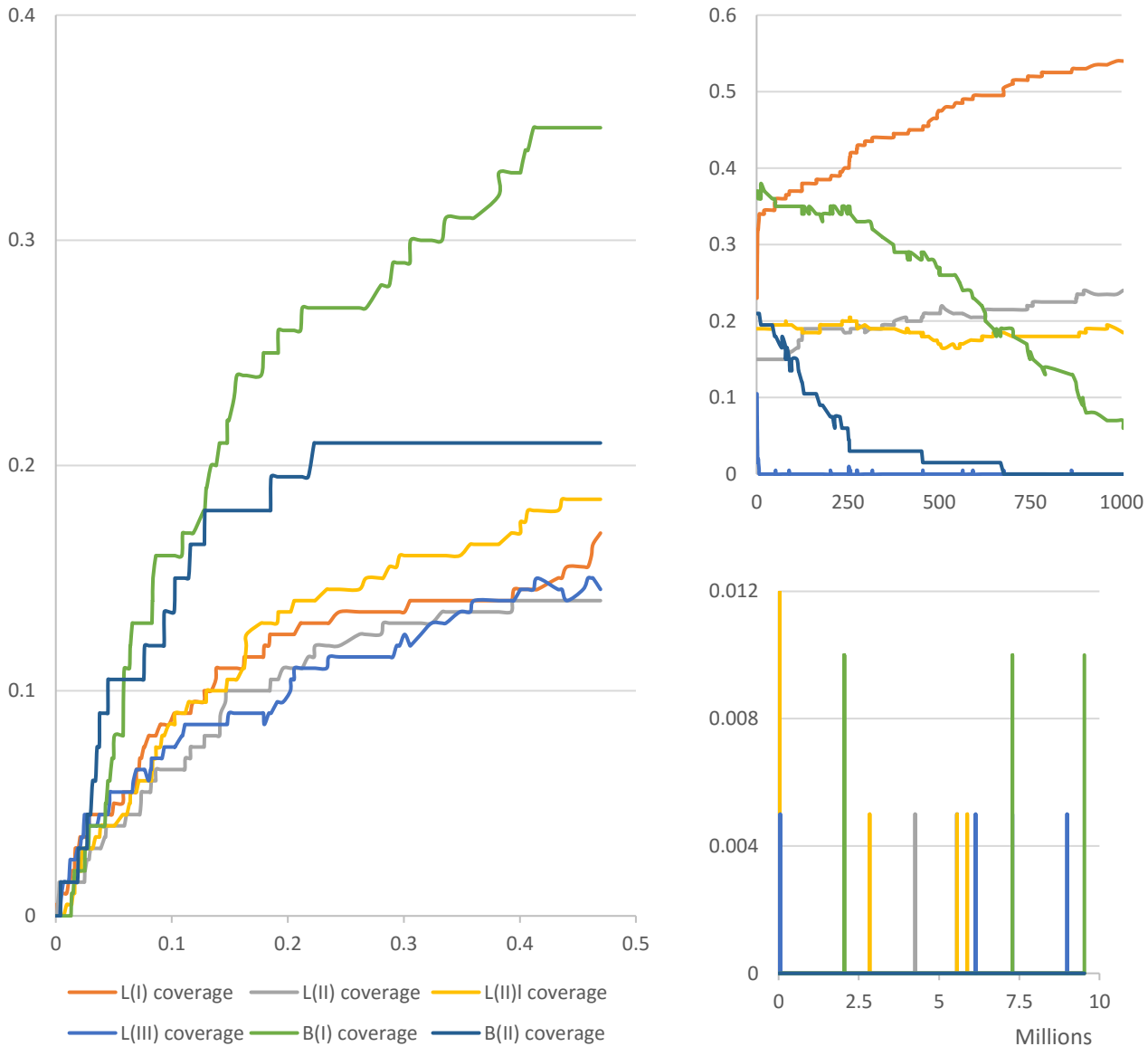

Figure 8-7 Coverage of different CO_2 adsorption modes at different non-dimensional time-scales

References

[1] A. Primo, Ş. Neaţu and H. García, "Chapter 14: Photocatalytic CO2 reduction," in *Advanced Materials fo Clean Energy*, CRC Press, 2015, pp. 421-445.

[2] C. Jooss and H. Tributsch, "Chapter 47: Solar Fuels," in *Fundamentals of Materials for Energy and Environmental Sustainability*, Cambridge University Press, 2012, pp. 656-674.

[3] A. Pougin, M. Dillab and J. Strunk, "Identification and exclusion of intermediates of photocatalytic CO2 reduction on TiO2 under conditions of highest purity," *Phys.Chem.Chem.Phys,* vol. 18, pp. 10809-10817, 2016.

[4] S. Neatu, J. A. Macia-Agullo and H. Garcia, "Solar Light Photocatalytic CO2 reduction: General Considerations and Selected Bench-Mark Photocatalysts.," *International Journal of Molecular Sciences,* vol. 15, pp. 5246-5262, 2014.

[5] M. R. Hoffmann, S. T. Martin, W. Choi and D. W. Bahneman, "Environmental Applications of Semiconductor Photocatalysis," *Chem. Rev.,* vol. 95, pp. 69-96, 1995.

[6] B. Kumar, M. Llorente, J. Froehlich, T. Dang, A. sathruum and C. P. Kubiak, "Photochemical and Photoelectrochemical Reduction of CO2," *Annu. Rev. Phys. Chem. ,* vol. 63, p. 541–69, 2012.

[7] B. Liu, "Monte-Carlo modelling of nano-material photocatalysis: bridging photocatalytic activity and microscopic charge kinetics," *Phys. Chem.,* vol. 18, pp. 1520-1527, 2016.

[8] J. B. Baxter, C. Richter and C. A. Schmuttenmaer, "Ultrafast Carrier Dynamics in Nanostructures for Solar Fuels," *Annu. Rev. Phys. Chem,* vol. 2014, p. 65, 423–47.

[9] B. Liu, K. Nakata, X. Zhao, T. Ochiai, T. Murakami and A. Fujishima, "Theoretical Kinetic Analysis of Heterogeneous Photocatalysis: The Effects of Surface Trapping and Bulk Recombination through Defects," *The Journal of Physical Chemistry,* vol. 115, p. 16037–16042, 2011.

[10] J. L. White, M. F. Baruch, J. E. I. Pander, Y. Hu, I. C. Fortmeyer and J. E. Park, "Light-Driven Heterogeneous Reduction of Carbon Dioxide: Photocatalysts and Photoelectrodes," *Chem. Rev.,* vol. 115, p. 12888−12935, 2015.

[11] A. Fujushima and K. Honda, "Nature 238," *Nature,* p. 37, 1972.

[12] Y. Ma, X. Wang, Y. Jia, X. Chen, H. Han and C. Li, "Titanium Dioxide-Based Nanomaterials for Photocatalytic Fuel Generations," *Chemical Reviews,* vol. 114, p. 9987−10043, 2014.

[13] U.S. Environmental Protection Agency, "Inventory of U.S. Greenhouse Gas Emissions and Sinks 2013," EPA, Washington D.C., 2015.

[14] M. Tahir and N. S. Amin, "Advances in visible light responsive titanium oxide-based photocatalysts for CO2 conversion to hydrocarbon fuels," *Energy Donversion and Management,* pp. 5-6, 2015.

[15] M. E. Boot-Handford, J. C. Abanades, E. J. Anthony, M. J. Blunt, S. Brandani, N. M. Dowell, J. R. Fernandez, M.-C. Ferrari, R. Gross, J. P. Hallet, R. S. Haszeldine, P. Heptonstall, A. Lyngfelt, Z. Makuch, E. Mangano and R. T. J. Porter, "Carbon capture and storage update," *Energy Environ. Sci.,* vol. 7, p. 130–189, 2014.

[16] B. Rybtchinski and M. R. Wasielewsk, "Artificial Photosynthesis for Solar Energy Conversion," in *Fundamentals of Materials for Energy and Environmental Sustainability*, Cambridge University Press, 2012, pp. 350-364.

[17] M. R. Singha, E. L. Clarka and A. T. Bella, "Thermodynamic and achievable efficiencies for solar-driven electrochemical reduction of carbon for Transportation Fuels," *PNAS,* pp. 1-10, 2015.

[18] L. Liu and Y. Li, "Understanding the Reaction Mechanism of Photocatalytic Reduction of CO2 with H2O on TiO2-Based Photocatalysts: A Review," *Aerosol and Air Quality Research,* vol. 14, pp. 453-469, 2014.

[19] A. Q. Fenwick, J. M. Gregoire and O. R. Luca, "Electrocatalytic Reduction of Nitrogen and Carbon Dioxide to Chemical Fuels: Challenges and Opportunities for a Solar Fuel Device," *Journal of Photochemistry and Photobiology B: Biology,* vol. 152, p. 47–57, 2015.

[20] Y. Hori, "Chapter 3: Electrochemical CO2 Reduction on metal electrodes," in *Modern Aspects of Electrochemistry*, New York, Springer, 2008, pp. 89-189.

[21] D. Beydoun, R. Amal, G. Low and S. McEvoy, "Role of nanoparticles in photocatalysis," *Journal of Nanoparticle Research,* vol. 1, p. 439–458, 1999.

[22] G. Odling and N. Robertson, "Why is Anatase a Better Photocatalyst than Rutile? The Why is Anatase a Better Photocatalyst than Rutile? The," *ChemSusChem,* vol. 8, p. 1838 – 1840, 2015.

[23] I. Alxneit and M. Corboz, "Influence of photoabsorbed O2 on the photoreduction of CO2 with water at the surface of TiO2," *J. Phys. IV France,* vol. 9, pp. 295-299, 1999.

[24] M. Tahir and N. S. Amin, "Photocatalytic CO2 reduction and kinetic study over In/TiO2 nanoparticles supported microchannel monolith photoreactor," *Applied Catalysis A: General,* pp. 1-14, 2013.

[25] Q. Zhang, Y. Li, E. A. Ackerman, M. Gajdardziska-Josifovska and H. Li, "Visible light responsive iodine-doped TiO2 for photocatalytic reduction of CO2 to fuels," *Applied Catalysis A: General,* vol. 400, p. 195–202, 2011.

[26] D. O. Scanlon, C. W. Dunnill, J. Buckeridge, S. A. Shevlin, A. J. Logsdail, S. M. Woodley, C. R. A. Catlow, M. J. Powell, R. G. Palgrave, I. P. Parkin, G. W. Watson, T. W. Keal, P. Sherwood and A. Walsh, "Band alignment of rutile and anatase TiO2," *Nature materials,* vol. 12, pp. 798-801, 2013.

[27] F. Donia, C. Mendive and D. Bahnemann, "TiO2 for water treatment: Parameters affecting the kinetics and mechanisms of photocatalysis," *Applied Catalysis B: Environmental,* vol. 99, p. 398–406, 2010.

[28] Y. Li, "Chapter 9: Fuel Production from Photocatalytic reduction of CO2 and water," in *Green Carbon Dioxide, Advances in carbon dioxide utilization.*, Messina, Italy, Wiley, 2014, pp. 245-265.

[29] N. M. Dimitrijevic, B. K. Vijayan, O. G. Poluektov, T. Rajh and K. A. Gray, "Role of Water and Carbonates in Photocatalytic Transformation of CO2 to CH4 on Titania," *Journal of the American Chemical Society,* vol. 11, pp. 3964-3971, 2011.

[30] D. Robert, V. Keller and N. Keller, "Immobilization of a Semiconductor Photocatalyst on Solid Supports: Methods, Materials, and Applications," in *Photocatalysis and Water Purification: From Fundamentals to Recent Applications*, Wiley-VCH, 2013, pp. 145-178.

[31] C. Guillard, B. Beaugiraud, C. Dutriez, J.-M. Herrmann, H. Jaffrezic, N. Jaffrezic-Renault and M. Lacroix, "Physicochemical properties and photocatalytic activities of TiO2-films prepared by sol-gel methods," *Applied Catalysis B: Environmental ,* vol. 39, pp. 331-342, 2002.

[32] Y. Chen and D. D. Dionysiou, "A comparative study on physicochemical properties and photocatalytic behavior of macroporous TiO2-P25 composite films and macroporous TiO2 films coated on stainless steel substrate," *Applied Catalysis A,* vol. 317, p. 129–137, 2009.

[33] J. Bennani, R. Dillert, T. M. Gesing and D. Bahnemann, "Physical properties, stability, and photocatalytic activity of transparent TiO2/SiO2 films," *Separation and Purification Technology,* vol. 67, p. 173–179, 2009.

[34] B. I. Stefanov, N. V. Kaneva, G. Li Puma and C. D. Dushkin, "Novel integrated reactor for evaluation of activity of supported photocatalytic thin films: Case of methylene blue degradation on TiO2 and nickel modified TiO2 under UV and

visible light," *Colloids and Surfaces A: Physicochemical and Engineering Aspects,* vol. 382, p. 219–225, 2011.

[35] I. Shakir, Z. Ali and D. J. Kang, "Layer by layer assembly of gold nanoparticles and graphene via Langmuir Blodgett method for efficient light-harvesting in photocatalytic applications," *Journal of Alloys and Compounds,* vol. 617, p. 707–712, 2014.

[36] K. Choudhary, V. Manjuladevi, R. K. Gupta, P. Bhattacharyya and S. K. A. Hazra, "Ultrathin Films of TiO2 Nanoparticles at Interfaces," *Langmuir,* vol. 31, pp. 1385-1392, 2015.

[37] C. S. Zalazar, R. L. Romero, C. A. Martín and A. E. Cassano, "Photocatalytic intrinsic reaction kinetics I: Mineralization of dichloroacetic acid," *Chemical Engineering Science,* vol. 60, p. 5240–5254, 2005.

[38] L. Davydov, S. E. Pratsinis and P. G. Smirniotis, "The Intrinsic Catalytic Activity in Photoreactors," *Environ. Sci. Technol.,* vol. 34, pp. 3435-3442, 2000.

[39] C. Guillard, B. Beaugiraud, C. Dutriez and J.-M. Herrmann, "Physicochemical properties and photocatalytic activities of TiO2-films prepared by sol-gel methods," *Applied Catalysis B,* vol. 39, no. Environmental, pp. 331-342, 2002.

[40] M. Tahir and N. S. Amin, "Photocatalytic CO2 reduction with H2O vapors using montmorillonite/TiO2 supported microchannel monolith photoreactor," *Chemical Engineering Journal,* pp. 4-10, 2013.

[41] S. Sing Tan, L. Zou and E. Hu, "Kinetic modelling for photosynthesis of hydrogen and methane through catalytic reduction of carbon dioxide with water vapour," *Catalysis Today,* vol. 131, p. 125–129, 2008.

[42] A. V. Emeline, V. K. Ryabchuk and N. Serpone, "Dogmas and Misconceptions in Heterogeneous Photocatalysis. Some Enlightened Reflections," *J. of Phys. Chem.,* vol. 109, pp. 18515-18521, 2005.

[43] A. Mills, J. Wang and D. F. Ollis, "Kinetics of Liquid Phase Semiconductor Photoassisted Reactions: Supporting Observations for a Pseudo-Steady-State Model," *J. Phys. Chem. B,* Vols. 14386-14390, p. 110, 2006.

[44] D. F. Ollis, "Kinetics of Liquid Phase Photocatalyzed Reactions: An Illuminating Approach," *J. Phys. Chem. B,* vol. 109, pp. 2439-2444, 2005.

[45] F. Karst, M. Maestri, H. Freund and K. Sundmacher, "Reduction of microkinetic reaction models for reactor optimization exemplified for hydrogen production from methane," *Chemical Engineering Journal,* vol. 281, p. 981–994, 2015.

[46] O. Hinr/Chsen, E. Rosowski, M. Muhler and G. Ertl, "The Microkinetics of Ammonia Synthesis Catalized by Cesium-Promoted Supported Ruthenium," *Chemical Engineering Science,* vol. 51, pp. 1683-1690, 1996.

[47] K. Yuan, L. Yang, X. Du and Y. Yang, "Numerical analysis of photocatalytic CO2 reduction in optical fiber monolith reactor with optimized structures," *Energy Conversion and Management,* vol. 87, p. 258–266, 2014.

[48] J. C. S. WU and C.-W. HUANG, "In situ DRIFTS study of photocatalytic CO2 reduction under UV irradiation," *Front. Chem. Eng. China,* vol. 4, p. 120–126, 2010.

[49] A. Markovits, A. Fahmi and C. Minot, "A Theroretical Study of CO2 Adsoption of TiO2," *Journal of Molecular Structure,* pp. 216 - 235, 1996.

[50] Y. L. Yongfei Ji, "Theoretical Study on the Mechanism of Photoreduction of CO2 to CH4 on the Anatase TiO2(101) Surface," *ACS Catalysis,* vol. 6, pp. 2018-2025, 2016.

[51] V. P. Indrakanti, J. D. Kubicki and H. H. Schobert, "Photoinduced activation of CO2 on TiO2 surfaces: Quantum chemical modeling of CO2 adosrption on oxygen vacancies," *Fuel Processing Technology,* vol. 92, pp. 805-811, 2011.

[52] H. He, P. Zapol and L. A. Curtiss, "Computational screening of dopants for photocatalytic two-electron reduction of CO2 on anatase (101) surfaces," *Energy & Environmental Science,* vol. 5, p. 6196–6205, 2012.

[53] P. Zawadzki, ,. A. B. Laursen, K. W. Jacobsen, S. Dahlb and J. Rossmeisl, "Oxidative trends of TiO2—hole trapping at anatase and rutile surfaces," *Energy Environ. Sci.,* vol. 15, pp. 9866-9869, 2012.

[54] J. Nelson, "Continuous-time random-walk model of electron transport in nanocrystalline TiO2 electrodes," *PHYSICAL REVIEW B,* vol. 59, pp. 374-380, 1998.

[55] R. Marcus, "Electron transfer reactions in chemistry. Theory and Experiments," *Pure and Applied Chemistry,* vol. 69, pp. 13-29, 1997.

[56] D. Monllor-Satoca, R. Gomez, M. Gonzalez-Hidalgo and P. Salvador, "The ‘‘Direct–Indirect’’ model: An alternative kinetic approach in heterogeneous photocatalysis based on the degree of interaction of dissolved pollutant species with the semiconductor surface," *Catalysis Today,* vol. 129, pp. 247-255, 2007.

[57] T. L. Villarreal Gomez, R. Gonzalez, M. and P. Salvador, "A Kinetic Model for Distinguishing between Direct and Indirect Interfacial Hole Transfer in the Heterogeneous Photooxidation of Dissolved Organics on TiO2 Nanoparticle Suspensions," *J. Phys. Chem.,* vol. 108, pp. 20278-20290, 2004.

[58] A. Usami and H. Ozak, "Optical Modeling of Nanocrystalline TiO2 Films," *J. Phys. Chem. B,* vol. 109, pp. 2591-2596, 2005.

[59] S. Sing Tan, L. Zou and E. Hu, "Photocatalytic reduction of carbon dioxide into gaseous hydrocarbon using TiO2 pellets," *Catalysis Today,* vol. 115, p. 269–273, 2006.

[60] V. Pareek, M. P. Brungs and A. A. Adesina, "A New Simplified Model for Light Scattering in Photocatalytic Reactors," *American Chemical Society - Ind. Eng. Chem.,* vol. 42, pp. 26-36, 2003.

[61] M. M. Hossain and G. B. Raupp, "Radiation field modeling in a photocatalytic monolith reactor," *Chemical Engineering Science,* vol. 53, p. 3771—3780, 1998.

[62] J. Kendrick and A. D. Burnett, "PDielec: The Calculation of Infrared and Terahertz Absorption for Powdered Crystals," *Journal of Computational Chemistry,* vol. 37, p. 1491–1504, 2016.

[63] N. Singhal, A. Ali, A. Vorontsov and C. Pendem, "Efficient approach for simultaneous CO and H2 production via photoreduction of CO2 with water over copper nanoparticles loaded TiO2," *Applied Catalysis A: General,* vol. 523, pp. 107-117, 2016.

[64] F. Saladin, L. Forss and I. Kamber, "Photosynthesis of CH4at a Ti02 Surface from Gaseous H20 and C02," *J. CHEM. SOC., CHEM. COMMUN.,* pp. 533-534, 1995.

[65] Z. Xiong, Z. Lei, B. Gong, X. Chen, Y. Zhao, J. Zhang, C. Zheng and J. C. Wu, "A novel reaction mode using H2 produced from solid-liquid reaction to promote CO2 reduction through solid-gas reaction," *Catalysis Communications,* vol. 89, pp. 4-8, 2017.

[66] S. P. Cadogan, G. C. Maitland and J. P. M. Trusler, "Diffusion Coefficients of CO2 and N2 in Water at Temperatures between 298.15 K and 423.15 K at Pressures up to 45 MPa," *J. Chem. Eng. Data,* vol. 59, p. 519−525, 2014.

[67] A. G. D. E. Syed Saad Ahsan, "Redox mediated photocatalytic water-splitting in optofluidic microreactors," *Lab on a Chip,* vol. 13, p. 409–414, 2013.

[68] H. S. Fogler, "Chapter 10: Catalysis and Catalytic Reactors," in *Elements of Chemical Reaction Engineering, Fifth Edition*, Prentice Hall, January 7, 2016, pp. 645-756.

[69] T. C. Merkel, Z. He, I. Pinnau, B. D. Freeman, P. Meakin and A. J. Hill, "Effect of Nanoparticles on Gas Sorption and Transport in Poly(1-trimethylsilyl-1-propyne)," *Macromolecules,* vol. 36, pp. 6844-6855, 2003.

[70] J. Singh, D. Kumar, S. Gupta and Sushila, "Application of Homotopy Perturbation Transform Method to Linear and Non-Linear Space-Time Fractional Reaction-Diffusion Equations," *The Journal of Mathematics and Computer Science,* vol. 5, pp. 40-52, 2012.

[71] C. Thangapandi and L. Rajendran, "Analytical expression of concentrations of adsorbed CO molecules, O atoms and oxide oxygen," *Natural Science,* vol. 5, pp. 326-332, 2013.

[72] J. W. Dingee and A. B. Anton, "A new perturbation solution to the Michaelis-Menten problem," *AICHE JOURNAL,* vol. 54, no. 5, pp. 1344-1357, 2008.

[73] M. Kumar and Parul, "Methods for solving singular perturbation problems arising in science and engineering," *Mathematical and ComputerModelling,* vol. 54, p. 556, 2011.

[74] D. Bozyigit, W. M. M. Lin, N. Yazdani, O. Yarema and V. Wood, "A quantitative model for charge carrier transport, A quantitative model for charge carrier transport, solar cells," *nature communications,* vol. 7180, pp. 1-10, 2014.

[75] Z. Dohna lek, J. Kim, O. Bondarchuk, J. M. W. White and B. D. Kay, "Physisorption of N2, O2, and CO on Fully Oxidized TiO2(110)," *J. Phys. Chem. B,* vol. 110, pp. 6229-6235, 2006.

[76] M. M. Islam, M. Calatayud and G. Pacchioni, "Hydrogen Adsorption and Diffusion on the Anatase TiO2(101) Surface: A First-Principles Investigation," *J. Phys. Chem. C,* vol. 115, p. 6809–6814, 2011.

[77] A. .. Valdes, Z.-W. Qu and G.-J. Kroes, "Oxidation and Photo-Oxidation of Water on TiO2 Surface," *J. Phys. Chem. C ,* vol. 112, p. 9872–9879, 2008.

[78] Q.-L. Tang, Q.-J. Hong and Z.-P. Liu, "CO2 fixation into methanol at Cu/ZrO2 interface from first principles kinetic Monte Carlo," *Journal of Catalysis,* vol. 604, p. 1869–1876, 2009.

[79] A. S. Cheettu and A. Heyden, "Combined DFT and Microkinetic Modeling Study of Hydrogen Oxidation at the Ni/YSZ Anode of Solid Oxide Fuel Cells," *J. Phys. Chem. Lett.,* vol. 3, p. 2767−2772, 2012.

[80] A. Yamakata, T.-a. Ishibash and H. Onishi, "Kinetics of the photocatalytic water-splitting reaction on TiO2 and Pt/TiO2 studied by time-resolved infrared absorption spectroscopy," *Journal of Molecular Catalysis,* vol. 199, no. A: Chemical, pp. 85-94, 2003.

[81] E. Korovin, D. Selishchev and D. Kozlov, "Photocatalytic CO2 Reduction on the TiO2 P25 Under the High Power UV-LED Irradiation," *Top Catal,* vol. 2016, p. 1292–1296, 59.

[82] P. C. Vesborg, J. L. Olsen, T. R. Henriksen, L. Chorkendorff and O. Hansen, "Gas-phase photocatalysis in micro-reactors," *Chemical Engineering Journal,* vol. 160, p. 738–741, 2010.

[83] I. L. C. Buurmans and B. M. Weckhuysen, "Heterogeneities of individual catalyst particles in space and time as monitored by spectroscopy," *Nature Chemistry,* vol. 4, pp. 873-886, 2012.

[84] A. Jansen, An Introduction of Kinetic Monte Carlo Simulations of Surface Reactions, Eindhoven, Netherlands: Lecture Notes in Physics, Springer., 2012.

[85] S. Tan, H. Feng, Y. Ji, Y. Wang, J. Zhao, A. Zhao, B. Wang, Y. Luo, J. Yang and J. G. Hou, "Observation of Photocatalytic Dissociation of Water on Terminal Ti Sites of TiO2 (110)-1 × 1 Surface," *J. Am. Chem. Soc. ,* vol. 134, p. 9978−9985, 2012.

[86] L. Chu, Z. Qin, J. Yang and X. Li, "Anatase TiO2 Nanoparticles with Exposed {001} Facets for Efficient Dye-Sensitized Solar Cells," *Nature,* vol. 5, pp. 12143 (1-10), 2015.

[87] J. S. Andrade, D. A. Street, Y. Shibusa, S. Havlin and H. E. Stanley, "Diffusion and reaction in percolating pore networks," *The American Physical Society,* vol. 55, pp. 772-777, 1997.

[88] D. C. Sorescu, W. A. Al-Saidi and K. D. Jordan, "CO2 adsorption on TiO2(101) anatase: A dispersion-corrected density functional theory study," *THE JOURNAL OF CHEMICAL PHYSICS,* vol. 135, pp. 124701 (1-17), 2011.

[89] L. Kunz, F. M. Kuhn and O. Deutschmann, "Kinetic Monte Carlo simulation of surface reactions on supported nanoparticles: A novel approac and computer code.," *The Journal of Chemical Physics,* vol. 044108, pp. 1-10, 2015.

[90] M. H. DeGroot, "Conditional Probability," in *Probability and Statistics*, Pitsburgh, Addison Wesley (Carnegie-Mellon University), 1885, pp. 72-82.

[91] H. He, P. Zapol and L. A. Curtiss, "A Theoretical Study of CO2 Anions on Anatase (101) Surface," *J. Phys. Chem,* vol. 114, p. 21474–21481, 2010.

[92] R. J. Braham and A. T. Harris, "Review of Major Design and Scale-up Considerations for Solar Photocatalytic," *American Chemical Society,* pp. 6-16, 2009.